The Influence of Electron Beam Welding Parameters on Heat Affected Zone and Weld Metal Cracking of Ni-Based Superalloys

By

Craig Churchman

Thesis submitted to the Engineering Faculty of the University of Manitoba for the degree of

Master of Science

in

Mechanical and Manufacturing Engineering

Supervisor: Dr. N.L Richards

Date

Department of Mechanical and Manufacturing Engineering

Winnipeg, MB

Copyright © 2008 by Craig Churchman

THE UNIVERSITY OF MANITOBA

FACULTY OF GRADUATE STUDIES

*****

COPYRIGHT PERMISSION

The Influence of Electron Beam Welding Parameters on Heat Affected Zone and Weld Metal Cracking of Ni-Based Superalloys

BY

Craig Churchman

A Thesis/Practicum submitted to the Faculty of Graduate Studies of The University of Manitoba in partial fulfillment of the requirement of the degree

Of

Master of Science

Craig Churchman © 2008

Permission has been granted to the University of Manitoba Libraries to lend a copy of this thesis/practicum, to Library and Archives Canada (LAC) to lend a copy of this thesis/practicum, and to LAC's agent (UMI/ProQuest) to microfilm, sell copies and to publish an abstract of this thesis/practicum.

This reproduction or copy of this thesis has been made available by authority of the copyright owner solely for the purpose of private study and research, and may only be reproduced and copied as permitted by copyright laws or with express written authorization from the copyright owner.

Acknowledgements

I would like to thank my supervisor, Dr N.L. Richards, for giving me the opportunity to work on this project and for his assistance, encouragement and support.

I acknowledge John Davies at Bristol Aerospace, Winnipeg MB for performing the electron beam welding on all material samples.

I would like to thank John Van Dorp, Don Mardis, and Dan McCooeye for their technical assistance. I would also like to thank Dr. O.A. Ojo and Dr. R Sidhu for their help. Furthermore I would like to thank Laura Stahl and Don Calverley for their help in the generation of this document.

The Influence of Electron Beam Welding Parameters on Heat Affected Zone and Weld Metal Cracking of Ni-Based Superalloys

by

Craig Churchman

Abstract

Nickel-based Superalloys IN 738, Rene 80, and a proprietary single crystal material were studied in this project. These three alloys are commonly used in the hot section of gas turbine engines due to their excellent properties at elevated temperatures. In this study the influence of electron beam welding parameters on the cracking susceptibility of the alloys was investigated. The welding of the samples was performed at Bristol Aerospace located in Winnipeg, Manitoba. Focus coil current and welding speed were varied on samples of varying thicknesses of each alloy to simulate different types of blade repair. The total weld metal and heat affected zone (HAZ) crack lengths along with the weld and HAZ areas were measured using an optical microscope equipped with an image analysis system. The crack length per unit area, termed cracking index, was calculated and used to evaluate the cracking tendency of the alloy with respect to varying welding parameters. Orientation image microscopy was also used to determine if changes in crystal orientation were responsible for the cracking present in the single crystal and directionally solidified alloys. The experimental results showed that (1) The hardness of all three alloys can be reduced significantly by performing a special heat

treatment called UMT. (2) IN 738 had a base microstructure of primary and secondary γ' with intermetallics present. The microstructure of the post heat treated alloy consisted of coarsened primary and secondary γ' plus the presence of $M_{23}C_6$ carbides. (3) The as-received microstructure of Rene 80 consisted of secondary γ' along with a variety of carbides, borides and intermetallics. After heat treating the secondary γ' was coarsened and M_6C carbides were present. (4) The single crystal microstructure had very few phases present with only secondary γ' and MC carbides visible. This is expected as fewer minor alloying elements are present as there is no need for grain boundary strengthening. Heat treating coarsened the γ' phase. (5) Analysis of the cracking index of each alloy indicates that the welding parameters play a key role in determining the cracking susceptibility of the weld. The effects of focus coil current and welding speed on the cracking susceptibility are discussed. (6) The post weld microstructure of the directionally solidified and single crystal alloys have been analysed and the results tend to agree with the reports of other investigators.

Table of Contents

Table of Figures

List of Tables

1.0 Introduction

1.1. Background

A gas turbine is a rotary machine consisting of three main components, the compressor, combustion chamber and turbine. It is commonly recognized for its use in aircraft propulsion which requires the addition of a nozzle on the back of the turbine to accelerate airflow. With ever increasing fuel costs as well as more stringent pollution control standards, it is desirable to increase the efficiency of any engine. The overall efficiency of a gas turbine engine can be improved by raising the operating temperature of the engine; however this places great demands on the materials chosen for the hot section components of the engine. Nickel-based Superalloys have been used successfully in the hot sections of turbine engines since the 1940's. The extended use of these materials in the hostile environment of a gas turbine leads to cracking and material loss which is caused by thermal and mechanical stresses, corrosion, erosion and oxidation. Replacing these parts is very costly so repair procedures have been necessitated. However, these procedures often require cracks to be welded and worn parts to be built up using a weld overlay.

Non-precipitation Ni-based Superalloys are usually reasonably weldable using weld procedures developed over the years and the use of skilled manual or semi-automated processes. Precipitation hardened alloys however present a challenge to welding engineers due to the gamma prime precipitation hardening phase which is present in percentages ranging from a few percent up to 80% in modern SX alloys. Thus

Ni-based Superalloys can be very difficult to weld due to their susceptibility to heat affected zone and weld metal cracking. Many studies have been performed as to why these materials crack, with the susceptibility to cracking being directly related to the microstructural constituents of the alloy. Materials with grain boundaries generally crack in the heat affected zone due to the liquation of particles such as carbides that are present along grain boundaries. It has been hypothesised that single crystal materials crack due to the presence of stray grains after welding. These stray grains are caused from the change between columnar to equiaxed grains during solidification which is caused by constitutional supercooling.

There have been many studies performed as to why these materials crack during welding, as well as there has been research into the effects of processing parameters on cracking susceptibility such as the work by Liu (Liu Y. N., 1996) and Li (Li, 2006). However, no report was found on the correlation of processing parameters to cracking behaviour of the newest modern alloys such as the ones studied in this work. In the present study three Ni-based Superalloys were welded using an electron beam welder and the cracking behaviour was studied. The three alloys studied were Inconel 738, Rene 80 and a proprietary single crystal alloy. The welded samples of each alloy were examined and correlations were made between the processing parameters and a cracking index. Furthermore, selected samples were examined using orientation image microscopy to determine why the samples exhibited cracking.

1.2. The Purposes of the Present Study

In the present study, the cast IN 738, Rene 80 and proprietary single crystal material were welded using an electron beam welder. An experiment was designed in order to determine the effect of welding parameters on the cracking susceptibility of each alloy. Focus coil current and welding speed were varied on specimens of varying thickness of each alloy. The objectives were:

(1) To study the effects of electron beam welding parameters on the cracking susceptibility of each alloy in a variety of repair configurations by correlating the cracking index to welding parameters.

(2) To use the data to determine the optimum combination of electron beam welding parameters to produce (if possible) a crack free weld.

(3) To understand the cracking process involved in crack initiation and propagation by means of orientation image microscopy

1.3. The Contributions of This Thesis

In this study 11 welding trials were performed on each of the three alloys. From these trials, 10 sections of each weld were examined and the crack lengths in both the heat affected zone (HAZ) and weld were measured by means of an optical microscope. The experimental results showed that (1) cracking was present in both the HAZ and weld of both IN 738 and Rene 80. This cracking would be associated with grain boundary liquation. (2) All cracking present in the proprietary single crystal was in the weld material. This is attributed to the formation of stray grains during the welding procedure.

(3) The welding velocity and focus coil current both had a significant effect on the cracking susceptibility of each alloy. (4) Cracking was minimized by using fast welding velocities and large beam defocus. (5) The cracking present in the proprietary single crystal appears to be due to the formation of stray grains within the weld zone.

2.0 Literature Review

2.1. Electron Beam Welding Characteristics

2.1.1. Definition

Welding is an essential process for the construction of many manufactured components. There are over 50 different types of welding operations as listed by the American Welding Society which can be categorized into two major groups: (1) fusion welding and (2) solid state welding. Electron beam welding (EBW) is categorized as a fusion welding process where heat is used to melt the base metal (Groover, 2002). In EBW no filler metal is generally added to the molten pool so the weld is referred to as autogenous. The heat required to melt the base metal is provided by a highly focused, high intensity stream of electrons that impinge against the workpiece. The high intensity electrons have a very high velocity, which is a function of accelerating voltage, of approximately 0.3 – 0.7 times the speed of light. This kinetic energy is converted into heat when the electrons strike the workpiece and thus the material is melted and the weld joint is produced (Kelly Ferjutz, 1993). There is not an extraordinary level of power in an EBW, but the power density is exceptional. The electron beam gun generally operates at high accelerating voltage (10kV – 150kV) with low beam current (milliamps). The high power density is obtained by focusing these highly accelerated electrons on a very small area of the workpiece.

2.1.2. Equipment

The process originated in the 1950's in the atomic power industry. The equipment used includes an electron beam gun, a power supply, a control system, and a workpiece motion system which may or may not be enclosed in a vacuum chamber. A schematic of an electron beam welder can be seen in Figure 2-1.

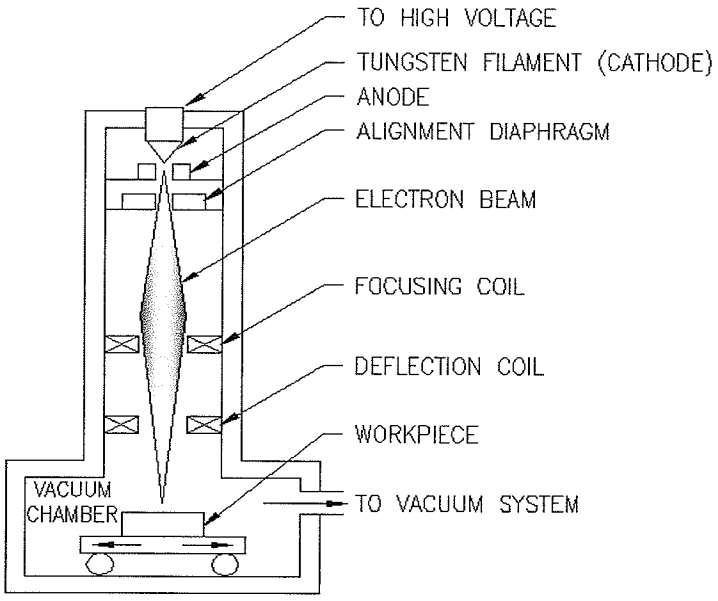

Figure 2-1 Electron Beam Welder Schematic

EBW has traditionally been performed only under high vacuum to minimize the disruption of the electron beam by air molecules. However, today there are three categories that are used in industrial applications. They are: (1) high vacuum (EBW-HV), where welding takes place in the same high vacuum as beam generation with pressures ranging from 0.13 – 0.30mPa. (2) medium vacuum (EBW-MV), where welding takes place in a separate chamber with only partial vacuum pressures of 0.13 – 3300Pa, and (3) non-vacuum (EBW-NV) where welding takes place at or near atmospheric pressure. High

vacuum welding produces the highest qualities and depth-width ratios, but can be a great inconvenience in production. It takes approximately 15 minutes to evacuate the chamber used in this study, however it may take hours to evacuate a large chamber to low pressure, and it may not be possible to weld large structure if they will not fit in the chamber. Medium vacuum and non-vacuum modes reduce the time required to load, unload and evacuate the chamber, but they require at least one vacuum divider to separate the beam generator from the chamber. This divider is a small orifice that impedes air flow but still allows the electron beam to pass. It is required as the beam generator must be at high vacuum (Groover, 2002). In high and medium vacuum there is no shielding gas required as there is no air present to contaminate the weld.

An electron beam gun is used to generate the electron beam that is used to heat the workpiece. Electrical current supplied by a power supply is passed through a tungsten filament and electrons are produced by thermionic emission. In this type of emission the electrons flow from the surface because their thermal vibration energy overcomes the electrostatic forces that restrain them. These free electrons are then accelerated from the gun by a high voltage potential between the cathode and anode. The electron beam then led down the column by Lorentz forces and is refined by focusing and deflecting electromagnetic coils. The electrons strike the workpiece which is generally mounted to a traversing welding table. The table can generally move in x and y directions. The accelerating voltage, focus coils and welding table along with other variables can be computer numerically controlled (CNC) by the operator.

2.1.3. Electron Beam Welding Parameters

An electron beam welder has many variables that can be manipulated to provide the desired weld characteristics. All welding variables are controlled by an operator using a computer. The thermal energy input to the workpiece can be optimized and controlled by at least six main variables which are (Engquist, 1968):

(1) The beam current and hence the number of electrons that impinge on the work surface which is determined by the current input to the electron gun

(2) The electron velocity which is controlled by the accelerating potential applied across the cathode and anode

(3) The size of the beam when it reaches the workpiece which is controlled by the beam focus coils

(4) The welding speed which is the velocity that the electron beam transverses across the metal to be welded and is controlled by moving the welding table

(5) The focal length or working distance is the length that the electrons "coast" between the gun and the workpiece

(6) The oscillation of the beam in the x and y directions which is controlled by beam oscillation coils.

Focus coil current and working distance interact to define the spot that the beam impinges on the workpiece. Spot size and beam power then interact to define power density. The beam can also be oscillated in the x and y directions and the oscillation frequency (puddle frequency) can also be varied. This can be useful as the beam can be

used to preheat the workpiece during welding. Many of these parameters are not found on a typical welding machine so the EBW process requires a trained operator.

2.1.4. Advantages and Disadvantages

Any metal that can be welded by the arc welding process along with some refractory and other exotic difficult to weld metals can be joined by the EBW process. Workpiece thickness can range from thin foils to thick plate. The EB process is well known for very high quality welds and high depth to width ratios. Because of the deep penetrating weld profiles generated with lower heat input, the heat affected zone (HAZ) of an EB weld is typically much smaller than one produced by an arc welding process. Additionally because of the low heat input and almost parallel sides of the weld profile there is much lower thermal distortion of the workpiece and much higher cooling rates. The high depth to width ratios generally eliminates the need for multiple passes. Since the workpiece chamber is evacuated there are no shielding gases or filler metals required. The high vacuum also leads to a cleaner, stronger and homogenous weld as atmospheric contamination is eliminated. Given that the welder is electronically controlled there is a high level of repeatability and precision that is not present with operator controlled processes.

As with many processes there are many disadvantages to the electron beam welder even though it produces high quality welds. There is a very high capital cost when purchasing an electron beam welder. If an operator is not aware of the effect of each parameter the reliability of the process can be reduced. Additionally the machine has a large footprint when compared to a gas tungsten arc (GTAW) or metal inert gas (MIG)

machine and requires a trained operator. Equipment maintenance is also high because of the vacuum pumps required to maintain the high level of vacuum. Also, joint preparation must be much better than arc processes and the parts must be located much more precisely on the welding table. This leads to higher costs in setup time and may cause a delay in production. Setup times must also include time to evacuate the chamber before welding can take place. Additionally most electron beam welding jobs require several sample welds in order to optimize the process parameters (Engquist, 1968). This trial and error can be very time consuming and expensive. Finally, the EBW presents a safety concern as the process generates x-rays which humans must be shielded from. Even with these disadvantages EBW is used in the automotive, aerospace, atomic power plant, electric and heavy industries (Richards, Chaturvedi, Liu, & Mount, 1996).

2.2. Features of a Fusion Weld

A typical fusion weld will consist of several zones. These are: (1) the fusion zone, (2) the weld interface, (3) the heat affected zone, and (4) the unaffected base metal. Three zones can be seen in Figure 2-2.

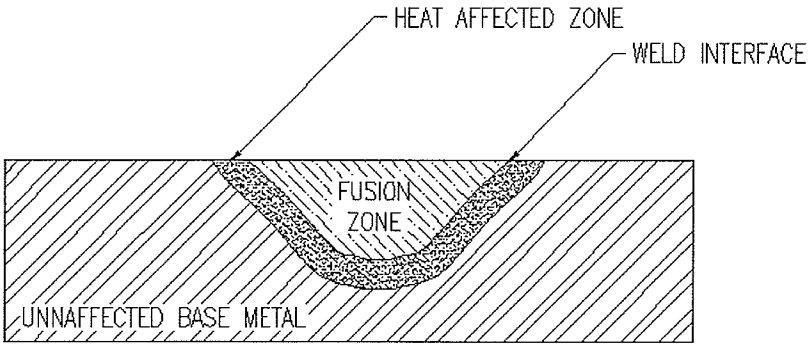

Figure 2-2 Fusion Weld Zones

2.2.1. The Fusion Zone

The fusion zone of a weld typically consists of a mixture of the filler metal and base metal that have completely been melted. In the case of electron beam welding there is no filler metal so the fusion zone only consists of melted base metal. The size and shape of the fusion zone is affected by the electron beam size, input power and oscillation amplitude (Li, 2006). The fusion zone has a high degree of homogeneity as the weld pool is mixed by convection. A weld interface zone separates the fusion zone from the heat affected zone. This narrow boundary consists of partially melted or melted base metal that solidified immediately before any mixing could take place.

2.2.2. The Heat Affected Zone

The zone where the material has experience temperatures below the melting point but high enough to cause microstructural changes is called the heat affected zone. This zone surrounds the fusion zone. The HAZ may be broken down further into sub zones such as grain growth, recrystallized zone, partially transformed zone, and tempered zone (Li, 2006). The extent of the material that has been affected by the rapid temperature rise depends on factors such as the amount of heat input; the peak temperature reached, the distance from the fusion zone, the length of time the material has been subjected to high temperatures, the cooling rate, and the materials thermal properties. The effect on the HAZ is usually detrimental to material properties and weld cracking frequently occurs in this zone. Furthest away from the fusion zone is the unaffected base metal. In this zone no metallurgical changes have occurred, but it is still likely to be in a high state of residual stress (Groover, 2002).

2.3. Grain Boundaries

A grain boundary is the region between two adjacent single crystals (grains). The grains meeting at this boundary have different orientations (Shackelford, 2000). A single crystal is ideally absence of any grain boundaries but there still may be the existence of sub grain boundaries. Many material properties are highly sensitive to the structure and size of the grains, and grain boundaries greatly affect the deformation and failure of materials. Grain size is a frequent parameter used to describe microstructures. According to the Hall-Petch relationship a materials' strength can be varied by changing the size of the grains. A material with fine grains has superior hardness, yield, tensile, and fatigue strength, and impact resistance at room temperature (Sullivan & Donachie, Feb. 1967). This is because grain boundaries act as pinning points which prevent dislocation propagation as well as dislocation sources. Coarse grained materials generally have superior creep properties at high temperatures. Even though grain boundaries have many positive attributes, they also have many negative. Carbides, nitrides and oxides tend to form on grain boundaries due to their high energy. Carbides can improve creep and rupture properties; however they may be very detrimental if the carbide forms a continuous film. This film may reduce impact strength significantly since cracks can nucleate and propagate through them (Chaturvedi, Richards, & Nakkalil, 1991). As well, many detrimental trace elements can be found on grain boundaries as they are rejected from the solute during solidification. This combination of factors makes failure analysis of grain boundaries very complex (Li, 2006).

2.4. Nickel-Based Superalloys

Overall efficiency of a gas turbine engine can be raised by increasing the operating temperature of the engine. This places great demands on the engineering materials used in the engine. To accomplish this, Nickel-based Superalloys are used extensively in the hot section components of modern long life jet aircraft engines and land-based gas turbine engines (Gaumann, 2001). A wide variety of elements are used in many combinations to provide the desired material properties in a Nickel-based Superalloy (Sullivan & Donachie, Feb. 1967). There can be over 20 elements that may be present or deliberately controlled during processing and may include elements such as aluminum, titanium, molybdenum, tungsten, and even heavy transition metals such as rhenium may be present. These elements and more may be present in varying quantities in each particular alloy. The critical properties that are required for a material to be useful in a turbine airfoil are: creep strength, thermal fatigue strength, and oxidation, and hot corrosion resistance.

Nickel Superalloys have a composite like structure with a solid solution matrix, γ, with an ordered FCC coherent or semi-coherent intermetallic precipitate γ'. Many other small phases are typically present but do not provide significant strengthening at low temperatures due to their low volume fraction. However, these phases provide significant creep and rupture strength. Inconel 738 is a cast precipitation-strengthened alloy that is used mainly because of its excellent elevated temperature strength and hot corrosion resistance (Ojo, Richards, & Chaturvedi, 2004). Rene 80 is a cast or directionally solidified material that has high rupture strength up to 1900°F, hot corrosion resistance,

and long term stability (Ross, Mar 1971). Single crystal materials have been developed as the elimination of grain boundaries further increases the high temperature creep resistance of the material (Park, Babu, Vitek, Kenik, & David, 2003).

2.4.1. IN 738

IN 738 is a nickel, chromium and cobalt based Superalloy that combines the strength of IN 713 and the sulphidation resistance of Udimet 500 (Thakur, Richards, & Chaturvedi, 2003). It is primarily used in the manufacturing of turbine blades and vanes. The alloy is vacuum melted and vacuum cast alloy that contains greater than six weight percent of Al and Ti. These elements form the ordered $L1_2$ intermetallic $Ni_3(Al,Ti)$ γ' phase. Solid solution hardening is the primary strengthener of cast alloys along with precipitation hardening. High temperature grain boundary strength is provided by $M_{23}C_6$ carbides. IN 738 can be used up to 980°C due to its excellent high temperature creep rupture strength and hot corrosion resistance.

2.4.2. Rene 80

The implementation of directionally solidified (DS) turbine airfoils in commercial engines in 1974 allowed significant increases in rotor speeds and hot section temperatures (Gell, Duhl, & Giamei, 1980). Rene 80 has been successfully used to cast small solid blades to large blades with complicated core passages. The alloy contains large amounts of Al and Ti which combines with nickel to precipitate the primary strengthening phase $Ni_3(Al,Ti)$. A minimum amount of eutectic gamma prime which is typically solutioned during heat treatment (Ross, Mar 1971). Rene 80 forms the MC matrix titanium carbide

during solidification that also breaks down during heat treatment to form M_6C and $M_{23}C_6$ grain boundary carbides. The molybdenum and tungsten present allow the formation of the M_6C carbide while chromium forms the $M_{23}C_6$ grain boundary carbide. The phase transition temperatures of the various components can be seen in Table 2-1 (H.A. Shahsavari, 2007).

Table 2-1 Rene 80 Phase Transition Temperatures

Liquidus	MC Carbide	Solidus	γ/γ' Eutectic	γ' Solvus
1318°C	1299 °C	1277 °C	1206 °C	1156 °C

2.4.3. Single Crystals

Single crystals were the next significant advancement in turbine airfoil technology after the advent of DS alloys. SX alloys have also been studied since the mid 1960's but did not see commercial use until the 1980's. A single crystal material is cast similarly to a DS alloy with the addition of a helix shaped crystal selector. The helix is usually of circular cross section with a diameter of 0.3 – 0.5 cm which minimizes the possibility of nucleation of grains at sharp edges. Two to six grains typically enter the helix where some of the grains are physically blocked from growing. After approximately two turns of the helix one grain emerges and continues to grow in the <001> orientation. High mold temperatures are maintained by radiant heating in order to ensure that no grains are nucleated on the surface of the mold as the casting solidifies. A schematic of the casting process can be seen in Figure 2-3 (Gell, Duhl, & Giamei, 1980).

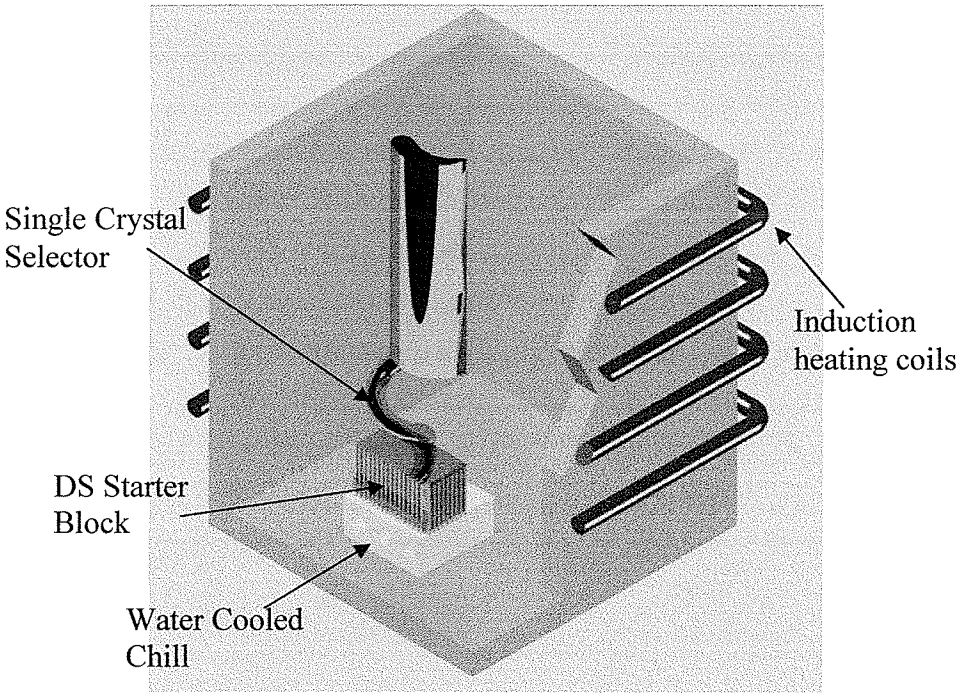

Figure 2-3 Single Crystal Casting Schematic

2.5. Strengthening of Superalloys

Many elements are added to nickel-based Superalloys for many different reasons. Solid solution strengthening, carbide precipitation strengthening, and γ' phase precipitation strengthening are used to improve the high temperature strength of the alloy. Elements such as cobalt, chromium, iron, molybdenum, tungsten and tantalum go into solid solution to provide strength. Chromium and aluminum provide oxidation resistance to the alloy, chromium also adds sulphidation resistance, and boron improves creep properties and rupture strength and may form borides if present in large amounts (Chaturvedi, Richards, & Nakkalil, 1991). Zirconium and carbides also increase the rupture strength of the alloy. Aluminum and titanium are added to the alloy and form the ordered face centered cubic intermetallic γ' phase. Other elements such as chromium and

cobalt may also be present in the γ'. It is this phase that is responsible for the high temperature properties of the alloys studied. The strength of the γ' phase increases to temperatures up to approximately 1400°C. However, there are several conditions that must be met in order to achieve the strengthening of the intermetallic phase. They are: (1) Volume fraction of at least 30%, (2) a strength greater than that of the matrix, (3) good lattice match with the matrix (within one percent), and (4) sufficient ductility to prevent a fracture path (Sullivan & Donachie, Feb. 1967).

Carbides are also an important part of a Superalloys' strength. They must be present at grain boundaries to produce the desired strength and ductility characteristics. There are several types of carbides that are possible that take the form MC, M_6C, $M_{23}C_6$, M_3C_2, and M_7C_3 where M stands for one or more types of metal atom. Normally the carbides transform from MC to $M_{23}C_6$ to M_6C sequentially with heat treatment. Elements including tungsten, tantalum, titanium, molybdenum and niobium form MC type carbides while chromium, molybdenum and tungsten form the $M_{23}C_6$ type carbide. Carbides typically form at the grain boundaries, but may form as a contiguous film on grain boundaries. This is extremely detrimental to material properties as it provides a continuous fracture path. The carbide distribution must be such that stresses can be relieved by a restricted degree of sliding so they therefore should be small and uniformly distributed.

2.6. Constitutional Supercooling

Many, if not all, useful engineering materials contain several constituents. During solidification of these multiconstituent materials the composition of the solid is given by

C_S and the composition of the liquid is given by C_L as determined from a phase diagram of the system. This can be seen in Figure 2-4.

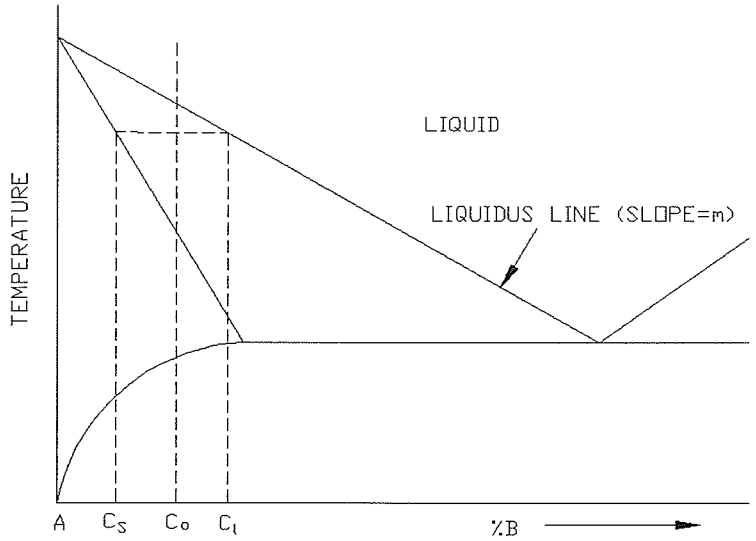

Figure 2-4 Phase Diagram

The partitioning coefficient, k is then given by:

$$k = \frac{C_S}{C_L} \tag{1}$$

This coefficient defines whether the solid in the solidifying system accepts or rejects solute. In most systems the coefficient is less than one and the liquid rejects solute. The concentration of the solute will be highest near the solid liquid interface and decrease exponentially with distance from the interface. Since the concentration of the solute is changed ahead of the solidification interface, the phase diagram also is affected depending on the partitioning coefficient. The slope of the solidus line typically increases due to the increased concentration ahead of the solidification front. Because of the increased concentration ahead of the interface and changes to the phase diagram, it is

possible for the solute to be at a temperature that is lower than its equilibrium solidification temperature as found on the phase diagram. The difference in the actual temperature of the solute and the liquidus temperature given by the phase diagram is the degree of supercooling. This can be seen in Figure 2-5. Constitutional supercooling is known as supercooling that is due to the segregation of solute (Jena & Chateurvedi, 1992).

The degree of supercooling is important as the type of solidification is determined by the amount of supercooling. For no undercooling the solidification interface is planar while for low undercooling the interface is cellular. With increasing undercooling the solidification interface changes to dendritic and equiaxed dendritic. This can also be seen in Figure 2-5 (Kurz, 1998).

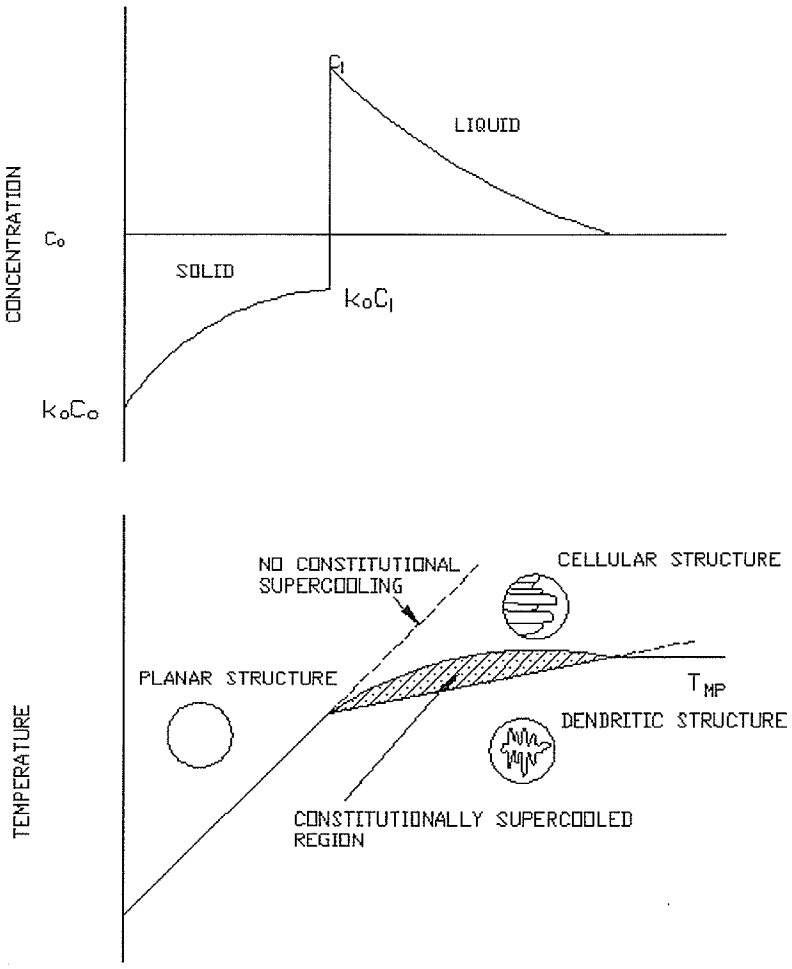

Figure 2-5 Constitutional Supercooling

2.7. Columnar to Equiaxed Transition

During the solidification of many metals three zones are typically formed. If hot metal is poured into a cool mould, a relatively thin zone of equiaxed grains commonly referred to as chill crystals are formed. The next zone is the columnar zone where dendrites grow preferentially in a direction that is normal to the liquidus isotherm. Hence they become elongated in one direction and are termed columnar. The preferred direction in which the dendrites freeze is in a direction such that the long axis is parallel to the

preferred crystallographic orientation. After some distance away from the mould wall there is typically a change from the columnar grains back to equiaxed grains which grow in suspension in a supercooled liquid. This change from columnar to equiaxed grains is termed the columnar to equiaxed transition (CET). The equiaxed grains are randomly oriented within the material. This transformation may occur abruptly or the equiaxed grains may be found dispersed among the dendrites before forming the full equiaxed zone. A typical cast structure showing the three regions can be seen in Figure 2-6 (Kurz, 1998).

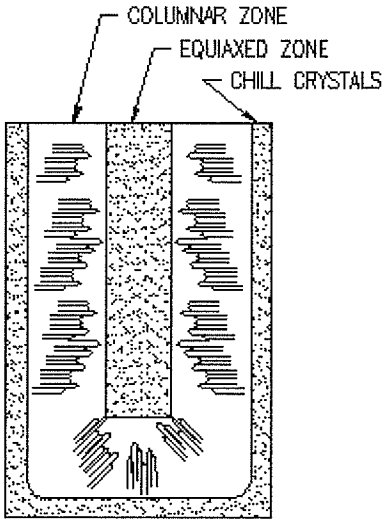

Figure 2-6 Columnar to Equiaxed Transition Zones

It is desirable in a commercial setting to produce either wholly columnar grains, such as the directionally solidified turbine blade where strength is improved along a particular crystal orientation, or wholly equiaxed structures. A fully equiaxed structure can provide less susceptibility to hot tearing in wrought alloys or improved fatigue life and better distribution of shrinkage porosity in castings. In order to produce a crystal

structure without a CET the cause of the transition must be understood. There are two requirements in order to form a structure with a CET which are: (1) the presence of a supercooled liquid ahead of or near the columnar front, and (2) that there are a sufficient number and size of equiaxed grains to arrest the columnar growth. These requirements are met due to one or more mechanisms that cause the CET. These mechanisms depend on such factors as cooling rate, freezing time, the temperature distribution ahead of the columnar front, thermal and constitutional supercooling, and the number and efficiency of potential nucleants within the melt. All of the mechanisms that are said to be responsible for the CET can be grouped into two categories: (1) those that involve the nucleation of equiaxed grains in the bulk liquid, and those that involve the detachment of dendrite fragments from the mould walls and/or the upper liquid-air boundary of the ingot.

The first hypothesis is that the CET is caused by constitutional supercooling. This hypothesis assumes that solute that accumulates at the dendrite tips leads to constitutional supercooling ahead of the growing dendrites (Spittle, 2006). If a critical supercooling is exceeded heterogeneous nucleation is suggested to occur. The condition necessary for the breakdown of planar growth due to constitutional supercooling is said to occur when:

$$\frac{G}{V} < mC_o(1-k)/kD \tag{2}$$

where G is the temperature gradient in the liquid, V is the interface velocity, m is the liquidus slope, C_o is the initial concentration, k is the equilibrium distribution coefficient, and D is the solute diffusion coefficient in the liquid (Spittle, 2006).

Another hypothesis is termed the "Big Bang". In this theory it is suggested that the grains in the equiaxed zone are nucleated at the time of pouring (Spittle, 2006). Some of the grains that are nucleated at the mould wall are swept into the melt by convection and pouring turbulence and those that survive remelting grow in the constitutionally supercooled region ahead of the dendrite interface.

A third theory is that dendrite tips are broken off and carried into the melt by buoyancy and convection (Spittle, 2006). The dendrite arms are said to break off due to the fact that secondary dendrite arms broaden once they have grown through the impurity layer that surrounds the main arm. This causes the arm to be attached by only a narrow neck that could be broken off by buoyancy and turbulence. It is suggested that these arms that break off are the nuclei of equiaxed grains that grow in the constitutionally supercooled melt.

The final theory that will be suggested is the showering of dendrite particles. This hypothesis attributes the CET to the formation of coarse dendrites at the surface of the ingot at the air-liquid interface (Spittle, 2006). It is suggested that these particles become dislodged and sink into the melt where they are the nuclei of the equiaxed zone. It has been observed experimentally that the grains in the equiaxed zone are comet shaped with a coarse dendritic head and a tail with the same structure as the columnar zone.

There are several other theories that may also attribute to the CET that will not be suggested here. Additionally many of these theories have aspects that some researchers may consider problematic. These debunking theories will also not be presented here.

Even with the theories that may or may not be correct, it is generally accepted that one or more of them will attribute to the formation of the CET.

2.8. Failure Modes

The general study of the failure of structural materials that have pre-existing flaws is called fracture mechanics. The cracking process consists of crack initiation and the crack propagation process. There are several mechanisms that this can occur by, but they are generally classified as brittle and ductile. Ductile fracture is found in many failures and is due to material overloading. A "cup and cone" is the typical fracture surface for a ductile failure. In brittle fracture there is rapid crack propagation without significant plastic deformation. Brittle fractures are very dangerous in practice as they typically occur instantly and often result in catastrophic failure. Under uniaxial loading plane strain conditions the critical stress intensity factor to produce catastrophic failure is termed K_{IC}. The value of fracture toughness describes flaw induced fracture and is given by:

$$K_{IC} = Y\sigma_f\sqrt{\pi a} \tag{3}$$

Where Y is a geometrical factor, σ_f is the applied stress at failure, and a is the length of a surface crack or ½ the length of an internal crack. Fracture toughness has units of $MPa\sqrt{m}$. If the applied stress is known then the critical crack length can be determine from this equation or the critical stress level can be obtained during design for a known size of flaw. Brittle materials with little ability to deform plastically have low K_{IC} values, while ductile materials that can undergo large amounts of plastic deformation have high values of K_{IC}.

2.8.1. Fatigue

Fatigue is defined as material failure after cyclical loading of a stress level that is below the ultimate tensile strength (Shackelford, 2000). This damage is plastically driven, and time and temperature independent. A fatigue crack is generally initiated at the surface of the material on any feature that concentrates local plastic strain and local stress. These features may include voids, inclusions, twin boundaries, grain boundaries, discontinuities or even uneven surface finish. Fatigue cracks will also preferentially start at a weld as there is a large discontinuity in mechanical properties near a weld. A "clamshell" fracture surface is typical for fatigue cracks. An *S-N curve* which is a logarithmic plot of stress, *S*, verses number of cycles, *N*, can be used to predict failure based on a known stress level or desired fatigue life. There are three stages in fatigue which are found on a typical *S-N curve*. Region I corresponds to a non-propagating fatigue crack. Region II represents unstable crack growth prior to catastrophic failure. In Region II cracking has a linear relationship which is given by (Paris, 1963):

$$\frac{d(2a)}{dN} = A(\Delta K)^m \tag{4}$$

where $2a$ is the crack length, A and m are material parameters which depend on the system, and ΔK is the stress intensity factor at the crack tip. K is a general stress intensity factor which is given by:

$$\Delta K = Y(\sigma_{max} - \sigma_{min})\sqrt{\pi a} \tag{5}$$

where Y is a geometrical factor and a is the length of a surface crack. Ferrous alloys typically have an endurance limit where the materials fatigue strength does not decrease with an increasing number of cycles after a certain number of cycles.

2.8.2. Oxidation

Oxidation is the general reaction between a metal and the oxygen that is present in the atmosphere. However, oxygen is not the only gas that can cause chemical attack. Nitrogen, sulphur and many other elements may also cause material degradation. In gas turbines sulphur from the fuel and salt in the air contribute greatly to hot corrosion. Almost all metals tend to form a stable oxide layer on their surface when exposed to air at high temperatures. Some of these oxides are protective against further environmental attack while others tend to crack. The salt and sulphur present in the air cause a molten sodium sulphate to form on the surface of a turbine blade. This sulphate dissolves elements such as molybdenum and vanadium which prevents the formation of a protective film (Gell, Duhl, & Giamei, 1980).

There are many mechanisms responsible for the build-up of oxides on a metallic surface, but they are all related to diffusion through the scale layer (Shackelford, 2000). The four diffusion mechanisms are: (1) an unprotective porous oxide film that oxygen can continuously pass though and react at the metal-oxide interface, (2) a nonporous film which cations diffuse through to react at the air-oxide interface, (3) a nonporous film which oxygen ions diffuse through to react at the metal-oxide interface, and (4) a nonporous film which cations and oxygen ions diffuse through at the same rate causing

the reaction to take place within the oxide itself. The diffusing ions are a result of two distinct mechanisms:

$$M \rightarrow M^{n+} + ne^-$$

$$O_2 + 4e^- \rightarrow 2O^{2-}$$

for the metal-oxide interface and air-oxide interface respectively.

The rate at which oxidation will occur can be determined by considering the diffusion rate. For an unprotective oxide the growth will be linear and given by:

$$y = c_1 t + c_2$$

where y is the thickness of the oxide film, t is the time and c_1 and c_2 are constants. The growth rate for a reaction limited by ionic diffusion is given by Fick's First Law and is:

$$y^2 = c_3 t + c_4$$

again where y is the thickness of the oxide film, t is the time and c_3 and c_4 are constants.

A metals tendency to form a protective oxide coating is given by the Pilling-Bedworth ratio which is given by:

$$R = \frac{Md}{amD} \tag{6}$$

where M is the molecular weight of the oxide with density D, and m is the atomic weight of the metal with density d. A protective coating will generally have an R value between 1 and 2 (Shackelford, 2000).

2.8.3. Creep

Creep is defined as permanent plastic deformation which occurs at high temperature under constant loading over long periods of time. In a typical creep curve, strain gradually increases over time through three stages of deformation. The first stage is called primary creep where the strain rate of the system decreases over time. In this stage the length of the material increases rapidly due to enhanced deformation mechanisms such as dislocation climb. This mechanism is enhanced as atom mobility is thermally activated. The second stage, also called secondary creep has a linear strain rate. In this stage the increased atom mobility is offset by an increase in the number of dislocations which reduces the strain rate. The final stage is called tertiary creep where strain rapidly increases to material failure. Since creep is a thermally activated phenomenon it can be modelled by the Arrhenius equation. The strain rate $\dot{\epsilon}$ is given by:

$$\dot{\epsilon} = Ce^{-Q/RT} \tag{7}$$

where C is a constant, Q is the activation energy, R is the universal gas constant, and T is the absolute temperature. By using this equation laboratory experimental data can be used to extrapolate the long term creep behaviour.

2.8.4. Reversing the Effects of Creep

Heat treatments are normally used in repair procedures of turbine blades in order to restore the creep rupture properties and improve the ductility of the material. However, when blades have long operation times (over 75000hrs) heat treatment alone cannot restore the creep rupture properties as the material is already in the second stage of creep damage. Hot isostatic compaction can be used to restore the creep rupture damage. This process is generally done at temperatures of 1100-1200°C in an argon purged autoclave at a pressure of 1000-2000bars (Haafkens, 1982).

2.8.5. Thermomechanical Fatigue

Isothermal fatigue tests have traditionally been used to estimate the life of engineering components used at high temperatures, however these tests do not consider many damage mechanisms that occur under thermomechanical fatigue (TMF). This type of fatigue is similar to mechanical fatigue except a thermal cycle is applied to the test material in addition to the cyclic loading. This type of test is very important as TMF is the primary life limiting failure mode for high temperature engineering materials. The thermal loading may be in phase (IP) or out of phase (OP) with respect to the cyclic loading. With IP tests, the maximum strain is applied at the maximum temperature, and in OP tests the maximum strain is applied at the minimum temperature. The phase shift may be applied from 0-360° in order to match the application parameters. Cycles may also include a large hysteresis to match realistic cycles. In TMF testing, there are three main failure damage mechanisms which are fatigue, oxidation, and creep. These three mechanisms may act independently or in combinations depending on the operating

parameters (Cai, Liaw, Ye, & Yu, 1999). The total strain applied is the sum of the thermal and mechanical components:

$$\varepsilon_{tot=}\alpha(T - T_o) + \varepsilon_{mech} \quad (8)$$

where T is the test temperature, T_o is the initial temperature, α is the coefficient of thermal expansion, and ε_{mech} is the sum of the elastic and inelastic strain components. Creep deformation contributes to the formation of microcracks and corrosion by oxidation is accelerated under TMF conditions. These brittle oxides can enhance the nucleation and propagation of microcracks. In a gas turbine blade TMF cracks typically initiate in the coating at the blade edge and propagate into the Superalloy.

2.9. Cracking Mechanisms

In spite of nickel Superalloys superior properties components suffer damage on extended use in the extremely hostile environment that exists in high temperature turbines. The extended use of materials in this environment results in cracking and material loss caused by thermal and mechanical stresses, corrosion, erosion, oxidation as well as mechanical damage due to the ingestion of foreign objects (Sidhu, Richards, & Chaturvedi, 2005). Since replacement parts have a very high cost, repair procedures have been necessitated. However, these procedures often require cracks to be welded and worn parts to be built up using a weld overlay on parts that are very difficult to weld (Banjeree, Richards, & Chaturvedi, July 2005). Nickel-based precipitation hardened Superalloys are generally considered difficult to weld due to their susceptibility to HAZ and weld cracking during welding and post weld heat treating. Weld cracking results from a competition between mechanical driving force for cracking and the materials resistance

to cracking (Ojo, Richards, & Chaturvedi, 2004). There are several mechanisms suggested that influence the cracking behaviour of the polycrystalline and single crystal alloys studied.

2.9.1. Grain Boundary Liquation

Liquation is the primary cause of low HAZ crack resistance in precipitation hardened Ni-based Superalloys (Owczarski, Duvall, & Sullivan, 1966). Liquation cracks are typically small and found in the HAZ of welds as shown in Figure 2-7 (Liu Y. N., 1996). Liquation occurs due to non-equilibrium interface melting below the alloys solidus or by equilibrium supersolidus melting. Thermally induced welding strain and or mechanically induced strain combined with low ductility that is caused by localized melting at grain boundaries results in the opening of the liquid film which is termed HAZ liquation cracking (Liu Y. N., 1996). Resolidified constituents were observed by Ojo in IN 738 along cracked grain boundaries in the HAZ and determined that grain boundary liquation is a factor in the cracking behaviour of this alloy (Ojo, Richards, & Chaturvedi, 2004). It was also noted that constitutional liquation of intergranular and intragranular γ' precipitates contributed significantly to HAZ liquation as extensive penetration and wetting of grain boundaries was present even at the sub-solidus region of the HAZ.

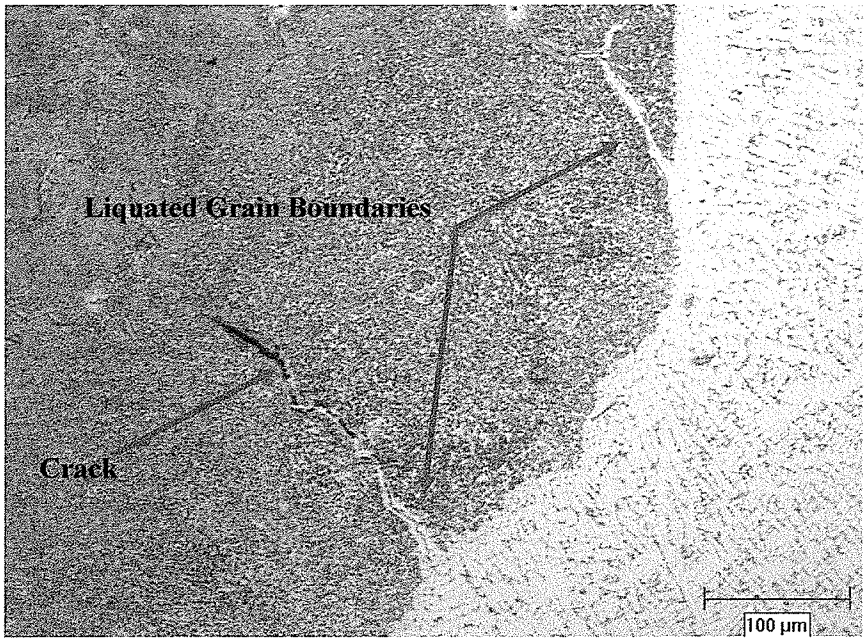

Figure 2-7 Optical Image of Liquated Grain Boundaries and Cracks in IN 738 200x

2.9.2. Stray Grain Formation

The formation of stray grains in nickel-based Superalloys is common over a wide range of alloys. A stray grain, which is a misoriented grain defect, may be present in castings and after welding. This can be expected as commercial single crystals do not contain grain boundary strengtheners that are common in polycrystalline and DS alloys. Welding of single crystal nickel-based alloys can lead to stray grain formation as well as preferential cracking which is associated to the stray grains. Vitek et al have suggested that the stray grains are caused by constitutional supercooling (CS) ahead of growing dendrite tips (Vitek, Babu, David, & Park, 2003). This CS would enable the nucleation of new grains ahead of the solidification front. In this mechanism solute is built up in front of the solidification front along with a low temperature gradient causes undercooling and

thus the nucleation of new grains. In order to avoid constitutional supercooling the following criterion can be applied:

$$G/V > \Delta T/D \tag{9}$$

where G is the thermal gradient in the liquid at the solidification front, V is the columnar dendrite growth velocity, ΔT is the solidification temperature range, and D is the liquid diffusivity. The solidification temperature range for the single crystal alloy studied is relatively large at 40°C, while the diffusivity is in the order of 10^{-8} m^2/s (Vitek, Babu, David, & Park, 2003). As these are constants, it suggests that a threshold value may exist for which a ratio $(G/V)_{cr}$ will predict the columnar to equiaxed transition of dendrites. By avoiding this transition and close process control, repair has been possible on damaged turbine blades (Gaumann, 2001). The thermal gradient along the weld centerline, G, can be calculated using analytical Rosenthal equations.

In addition to the level of constitutional supercooling, Park et al (Park, Babu, Vitek, Kenik, & David, 2003) have determined that the formation of stray grains is also very sensitive to the crystallographic orientation of growing dendrites as well as processing conditions. Laser welds were made on a proprietary single crystal alloy and it was found that stray grain formation was different on either side of the centerline of the weld. Stray grain formation was heavy on one side of the centerline and sometimes extended onto the other side, but the single crystal nature was generally maintained on the other side. It was found that this phenomenon correlates well to the ratio of G/V and a threshold value could be estimated from experimental observations. The formation of

stray grains depends on the *G/V* ratio being below the threshold value and also on the nucleation rate for forming new grains.

The fact that no abundant stray grains are found on one side of the weld was explained by Park using the *G/V* ratio (Park, Babu, Vitek, Kenik, & David, 2003). The *G/V* ratio will be smaller than the threshold value for a short distance before the transition line, bust since the formation of stray grains also depends on nucleation rate there is also time dependence. Since *G/V* is only below the threshold for a short distance and growth velocity is large near the centerline, it is suggested that there is insufficient time for abundant stray grains to nucleate.

Park et al also found that extensive stray grain formation was only observed when there was a large difference between the dendrite growth direction and the interface normal, ψ (Park, Babu, Vitek, Kenik, & David, 2003). The cooling rate, *GV*, was found to be symmetrical about the weld centerline while *G/V* was not. This is because the cooling rate depends on weld pool shape while *G/V* depends on the dendrite direction. Both parameters also vary with processing parameters. With increasing power and speed, ψ increases to the left side of the weld while ψ decreases on the right side of the weld. Therefore the difference in ψ becomes larger. If this value is not close to zero the dendrite tips are not aligned which changes the diffusion field and solidification temperature range. However, with increasing weld speed and power there were no stray grains formed unless ψ was very large.

3.0 Experimental Procedure

3.1. Equipment

3.1.1. Electron Beam Welder

Bead-on-plate electron beam welding was performed by a trained operator using a Sciaky 60kV, 30kW electron beam welder located at Bristol Aerospace, Winnipeg, MB. The welder chamber and controller can be seen in Figure 3-1.

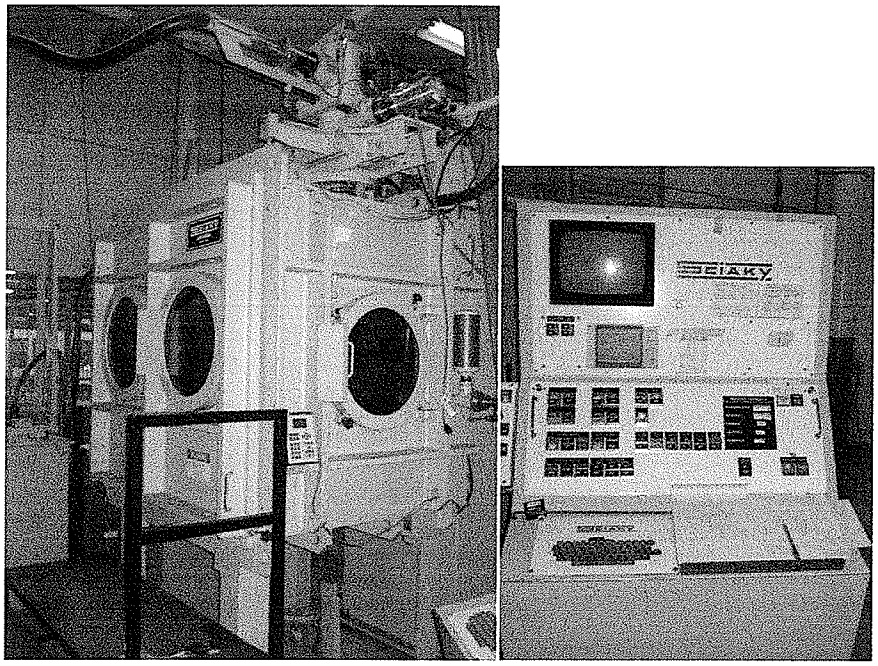

Figure 3-1 Sciaky Electron Beam Welder

3.1.2. Microscopic Examinations

Each sample was examined using a Zeiss Axiovert 25 CA Inverted Reflected-Light digital microscope equipped with Clemex image analysis software. Cracking was measured in both the HAZ and in the weld. Magnification varied during this process from

3x to 500x magnification depending on the size of the cracks present in the sample. The weld depth from the top of the parent material, top width and width at half of the maximum weld depth was measured. The HAZ of the IN 738 and Rene 80 samples were also measured using Clemex software. The HAZ area was visible on the samples so it was simply measured by tracing the outline by hand using the image area calculator in the Clemex software. The weld area was measured for all three alloys, again by simply tracing the outline of the visible weld area.

It was also of interest to obtain high magnification images of the pre and post heat treated microstructures and to perform chemical analysis on the microstructural constituents to determine the phases present. These high magnification images and chemical analysis were obtained using a JEOL JSM-5900LV Scanning Electron Microscope (SEM) which was equipped with an ultra-thin window Oxford Energy-Dispersive X-Ray Spectroscopy (EDS) system. Grain boundary types and presence were determined using electron back scattered diffraction (EBSD) orientation image microscope scans (OIM is a trademark of TexSEM Laboratories Ltd) using the JEOL JSM 5900LV SEM.

3.2. Materials

The investment castings used in this study were supplied in 0.35" x 2.0" x 7.9" (9mm x 50mm x 200mm) pieces by PCC Airfoils with the <001> direction being along the length of the casting. The castings were received in the solution treated condition and came complete with third party Certificate of Tests as well as x-ray radiographs. The elemental composition of IN 738 and Rene 80 as per the supplied certificates can be

found in Tables 3-1 and 3-2. The elemental composition of the single crystal alloy is proprietary and therefore will not be disclosed in this document; however it contains approximately 60% γ' phase.

Table 3-1 IN 738 Composition – wt. %

Carbon	Sulphur	Silicon	Manganese	Phosphorus
C	S	Si	Mn	P
0.112	0.001	0.04	<0.01	<0.005
Aluminum	Cobalt	Tungsten	Vanadium	Copper
Al	Co	W	V	Cu
3.4	8.17	2.58	<0.01	<0.01
Chromium	Molybdenum	Iron	Titanium	Hafnium
Cr	Mo	Fe	Ti	Hf
16.02	1.77	0.03	3.44	<0.02
Zirconium	Boron	Niobium	Tantalum	Rhenium
Zr	B	Nb	Ta	Re
0.028	0.009	0.9	1.71	0.02

Table 3-2 Rene 80 Composition – wt. %

Carbon	Sulphur	Silicon	Manganese	Phosphorus
C	S	Si	Mn	P
0.2	0.001	0.04	<0.01	<0.015
Aluminum	Cobalt	Tungsten	Vanadium	Copper
Al	Co	W	V	Cu
2.9	9.52	4	<0.01	0.02
Chromium	Molybdenum	Iron	Titanium	Hafnium
Cr	Mo	Fe	Ti	Hf
14.1	3.98	0.18	4.98	0.02
Zirconium	Boron	Niobium	Tantalum	Rhenium
Zr	B	Nb	Ta	Re
0.028	0.013	0.02	<0.02	<.02

3.3. Sample Preparation

Since the materials used in this study are very expensive and difficult to obtain, they were cut in varying thicknesses according to the target weld depths. In the cases of the directionally solidified and single crystal materials, the castings were cut so that the crystal orientation would be aligned to what would be typically found in a trailing edge repair of a gas turbine blade. This orientation was normal to the (001) plane. Before cutting each sample the x-ray radiographs supplied by the vendor were checked for casting defects. Some of the castings had visible defects including porosity and voids which were avoided during cutting. The material was cut using the wire EDM process which does not significantly alter the microstructure of the material due to its low heat input.

Once the material was cut, they were UMT heat treated. This treatment was 1120°C for two hours, air quench followed by 1020°C for 16 hours with a water quench for IN 738. The heat treatment for Rene 80 was at 1020°C for 16 hours with water quench and the treatment for the single crystal alloy was at 1200°C for 16 hours with water quench. Vickers hardness was measured before and after heat treating on a pyramid hardness testing machine with a load of 10kg. After heat treating the specimens were prepared on 180 grit silicon carbide paper to remove any oxides formed during the heat treating process. This also removed the recast layer caused by the EDM process and yielded a clean surface to weld on. All samples were tack welded using GTAW to a large 0.2" (5mm) thick stainless steel plate. This was done to prevent the material from warping during welding as well as to provide a heat sink for the material to aid in cooling

samples that were adjacent to the welded samples. The prepared samples can be seen in Figure 3-2.

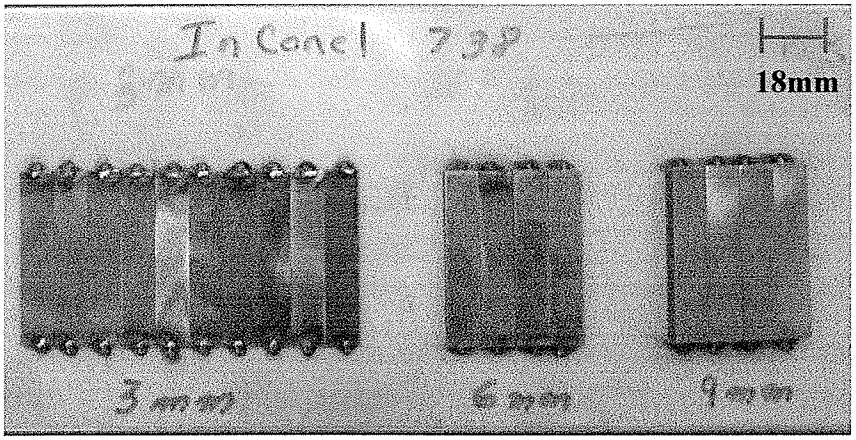

Figure 3-2 Photograph of Prepared Samples.

In order to minimize experimental error, all of the welding for each alloy was completed within one working day. Once the samples were welded, they were removed from the stainless steel plate by grinding. Each trial was then sectioned using EDM to obtain 10 one millimetre thick samples. These samples were mounted in Bakelite and polished to 1μm using standard metallographic specimen preparation techniques. The samples were then electrolytically etched for approximately 3 seconds at 5.0V in a γ' etchant containing 24ml of H_3PO_4, 80ml of HNO_3, and 96ml of H_2SO_4. For OIM examination samples were further polished using a rotary wheel with 0.05 micron colloidal silica for at least 30 minutes.

3.4. Development of Experimental Parameters

Since all of the materials studied are very expensive and difficult to obtain, experimental parameters were first developed on stainless steel. Initial testing parameters were obtained from previous work at the University of Manitoba under Liu (Liu, Richards, & Chateurvedi, 1995). The first test was run at 44kV, 79mA, 60ipm (25 mm/s), no oscillation and a working distance of 9.5" (24cm). The focus coil current was varied to focus the electron beam below the surface of the material, on the surface of the material, and above the surface. The welds were then sectioned and the weld depth and width were measured. These values were then compared with Liu and can be seen in Figure 3-3. This data was analysed and determined that the target weld depths could be reached with the parameters that were tested.

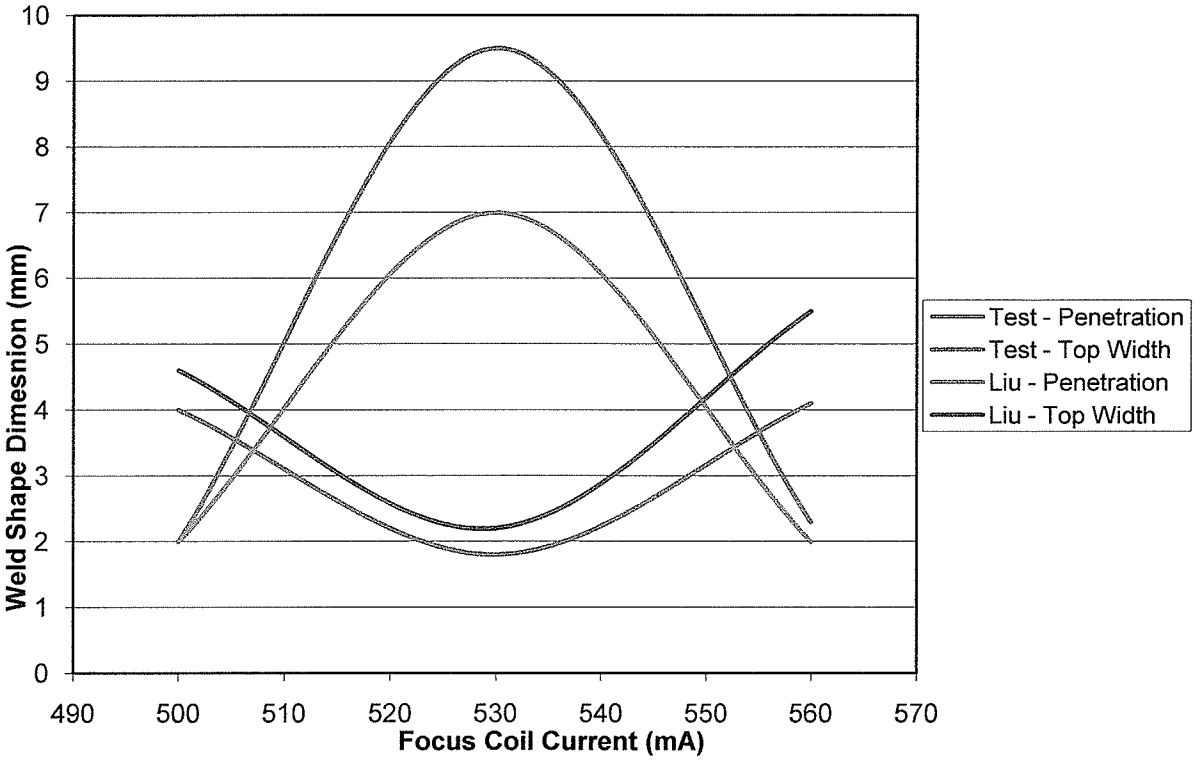

Figure 3-3 Development of Focus Parameters

The second weld parameter that was desired to be varied was weld speed. Initial testing parameters were again obtained from Liu (Liu, Richards, & Chateurvedi, 1995) and were 44kV, 45mA, sharp focus, working distance of 9.5" (24cm) with oscillation set at approximately 10% of maximum. Weld speed was then varied in inches per minute at 10 (4mm/s), 20 (8mm/s) and 40 (17mm/s). The welds were again sectioned and compared to Liu (Liu, Richards, & Chateurvedi, 1995). The data can be seen in Figure 3-4.

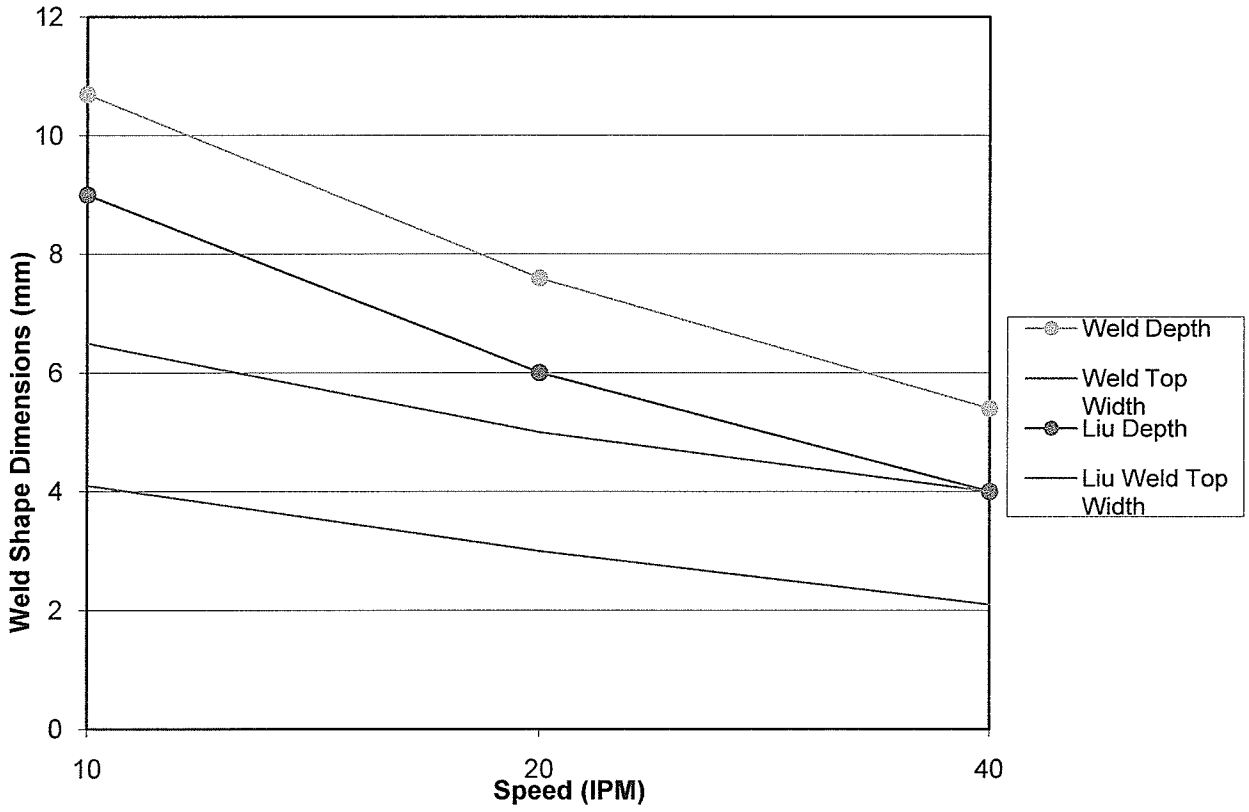

Figure 3-4 Development of Speed Parameters

All of the welds obtained with these parameters had a spike shape which is undesirable for testing. It was also determined that the target weld depths could not be

reached with the initial testing parameters so a second test was designed with increased oscillation to 50% of maximum. Previous work by Li indicated that this setting would yield approximately 0.04" (1mm) amplitude of oscillation on the welder used during the experiment (Li, 2006). The increased oscillation should give a bowl shaped weld with less penetration. The weld depth and width data with increased oscillation can be seen in Figure 3-5.

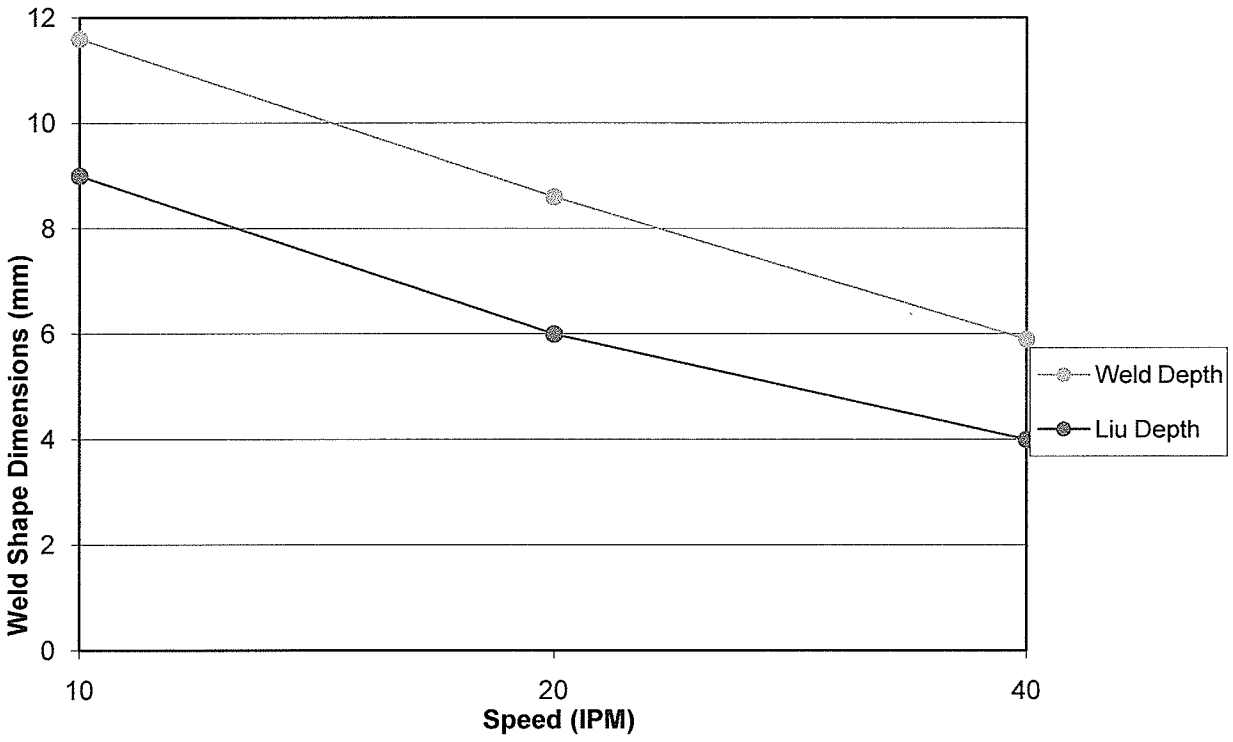

Figure 3-5 Development of Speed Parameters Trial 2

Again the weld depth was too large to reach the target weld depths for the experiment, so a third focus test was done with a defocused beam. Focus coil current was varied to focus the beam above and below the surface of the steel. It was determined that

by focusing the beam below the surface of the sample, a bowl shaped weld with suitable depth could be obtained. The weld dimensions can be seen in Figure 3-6.

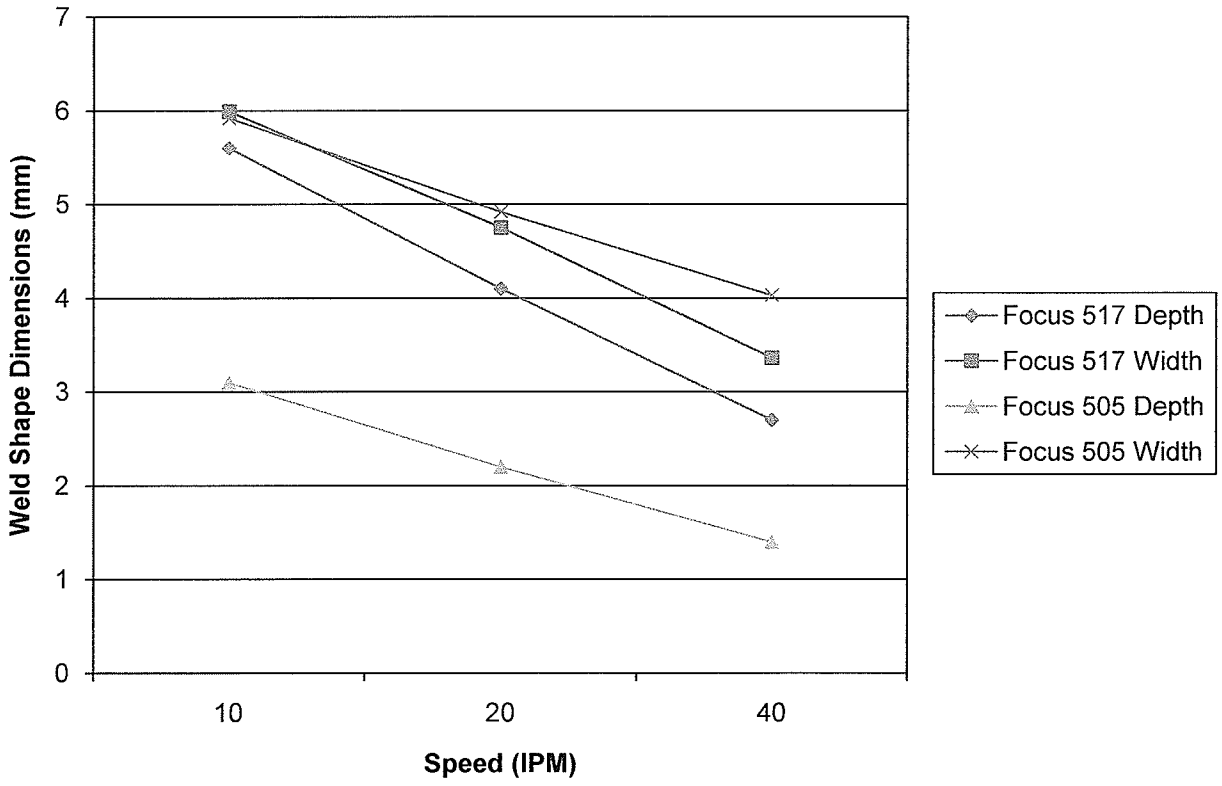

Figure 3-6 Development of Speed Parameters Trial 3

From Figures 3-3 through 3-6, the final weld parameters for the experimental trials were chosen. The final eleven parameters would yield target weld depth ranging from 0.12" (3mm) to 0.43" (11mm) as shown in Table 3-3 and 3-4.

Table 3-3 Focus Experimental Parameters

	Fixed Parameters	
	Accelerating Voltage	44kV
	Amperage	79mA
	Speed	60ipm (25mm/s)
	Working Distance	9.5" (24cm)
	No Oscillation	
Sample	**Target Depth inches (mm)**	**Focus (mA)**
2	0.08 (2)	505
3	0.24 (6)	513
4	0.31 (8)	520
5	0.31 (8)	541
6	0.24 (6)	548
7	0.12 (3)	558

Table 3-4 Speed Experimental Parameters

Fixed Parameters	
Accelerating Voltage	44kV
Amperage	45mA
Focus Coil Current	505mA
Working Distance	9.5" (24cm)
No Oscillation	

Sample	Target Depth inches (mm)	Speed ipm (mm/s)
9	0.12 (3)	10 (4)
10	0.08 (2)	20 (8)

Fixed Parameters	
Accelerating Voltage	44kV
Amperage	45mA
Focus Coil Current	530mA
Working Distance	9.5" (24cm)
Xsf=Ysf	500

Sample	Target Depth inches (mm)	Speed ipm (mm/s)
11	0.43 (11)	10 (4)
12	0.35 (9)	20 (8)
13	0.24 (6)	40 (17)

4.0 Results and Discussion

4.1. Microstructure Characterization

4.1.1. IN 738 – As-Received

The as-received castings were heat treated at 1120°C for 2hrs followed by a furnace cool which is the standard heat treatment for this alloy. The castings had a Vickers hardness of 418 ± 14VPN. A sample image of the IN 738 microstructure can be seen in Figure 4-1. Primary and secondary γ' are visible along with a γ - γ' eutectic in a fan shaped configuration. Also visible in this figure is a Ni-Zr rich intermetallic. The EDS spectrum for the Ni-Zr intermetallic can be seen in Figure 4-2. Other microstructural constituents that were present in the microstructure that are not visible in the figure included MC type carbides, TiZr-rich sulphocarbides, Cr-Mo rich borides and Ni-Ti rich intermetallics.

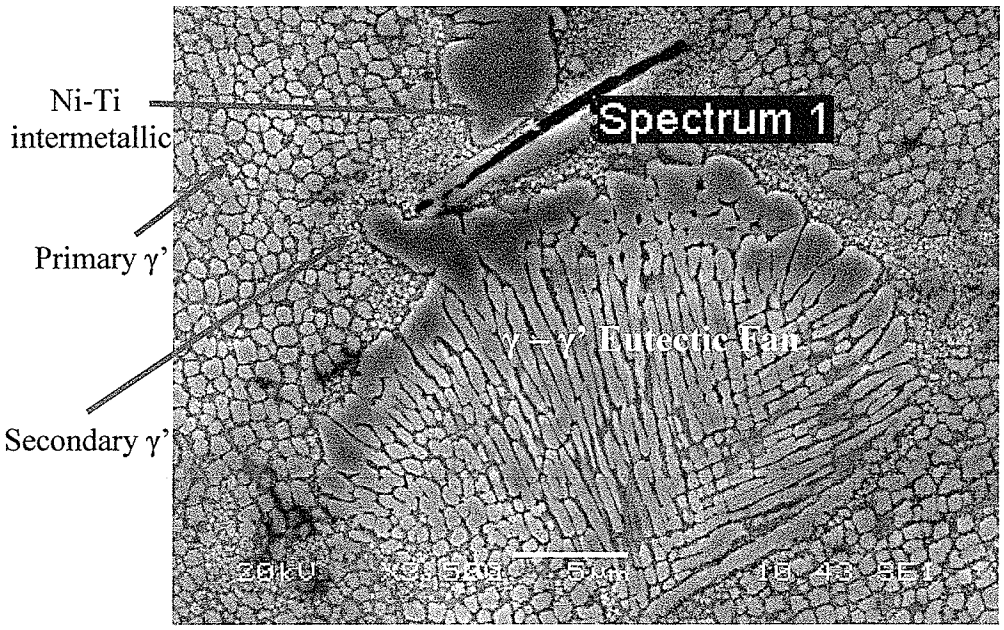

Figure 4-1 SEM SEI Image of As-Received IN 738 3500x

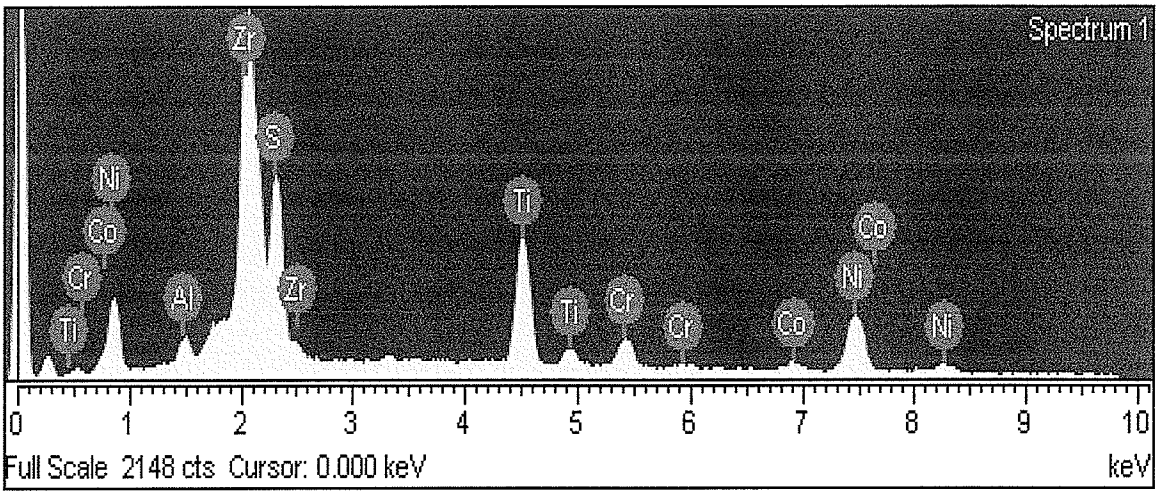

Figure 4-2 EDS Spectrum for Ni-Zr Rich Intermetallic in As-Received In 738

4.1.2. IN 738 - UMT Treated

The as-received castings were heat treated for 16hrs at 1020°C followed by a water quench. This treatment lowered the hardness of the alloy by approximately 100VPN to 307 ± 17VPN. It was noticed in the 0.35" (9mm) samples that the hardness was reduced to approximately 320VPN, while the 0.04" (1mm) samples (not used) hardness was reduced to approximately 280VPN. The phases present in the alloy were the same as those found in the as-received condition with the exception of the addition of $M_{23}C_6$ carbides that were found on the grain boundaries. With the SEM set to back scattered electron image mode the type of carbide can be distinguished by contrast. For example MC type carbides will be grey while $M_{23}C_6$ carbide will show up as white (H.A. Shahsavari, 2007). Primary and secondary γ' are still present, although there was significant coarsening. These phases along with two $M_{23}C_6$ grain boundary carbides are

visible in Figure 4-3. The EDS spectrum for one of the $M_{23}C_6$ carbides can be seen in Figure 4-4.

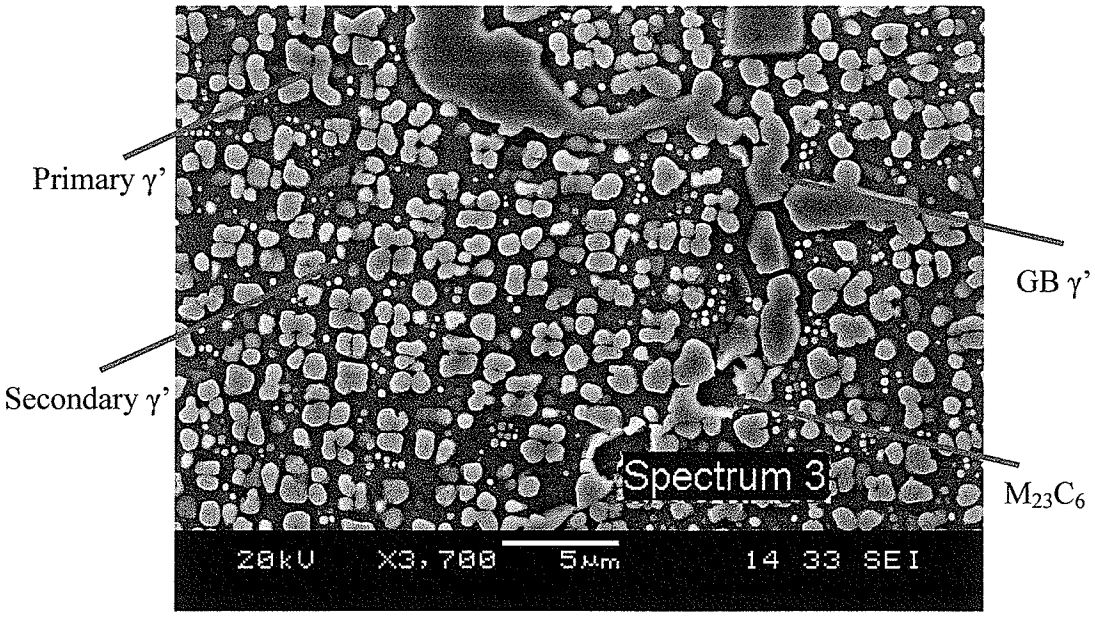

Figure 4-3 SEM SEI Image of UMT Heat Treated IN 738 3700x

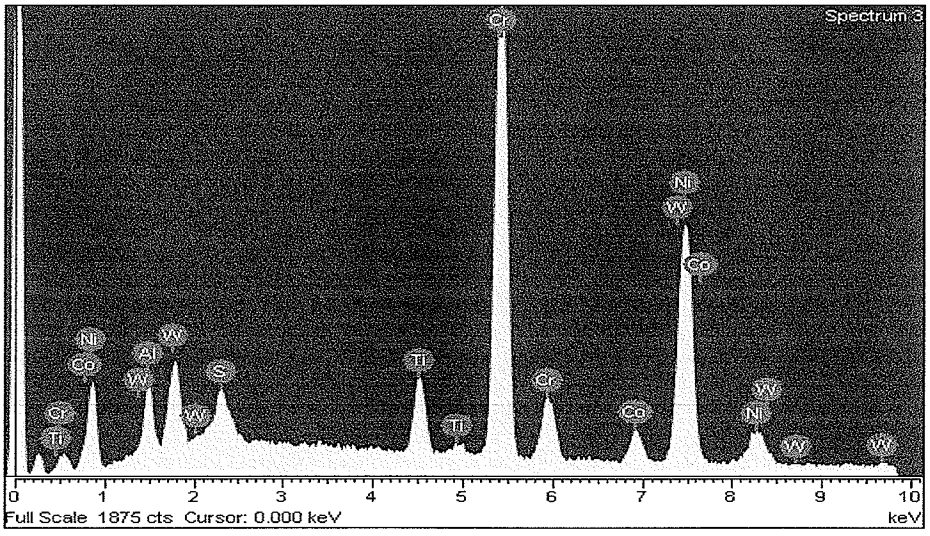

Figure 4-4 EDS Spectrum of Grain Boundary $M_{23}C_6$ in UMT Heat Treated IN 738

4.1.3. Rene 80 – As-Received

The Rene 80 castings were received in a heat treated condition, having been heat treated by the casting supplier at 1204°C for two hours followed by a slow furnace cool. This condition had a hardness of 453 ± 29VPN. A typical as-received microstructure for this alloy can be seen in Figure 4-5. No primary γ' was observed, only secondary γ' was evident. Also visible in this figure are several Ni-Ti rich intermetallics. An EDS spectrum for one of the intermetallics can be found in Figure 4-6. Other phases that were found include MC type carbides, Ti-Zr rich sulphocarbides, Ni-Zr and Ni-Ti rich intermetallics, and Cr-Mo rich borides.

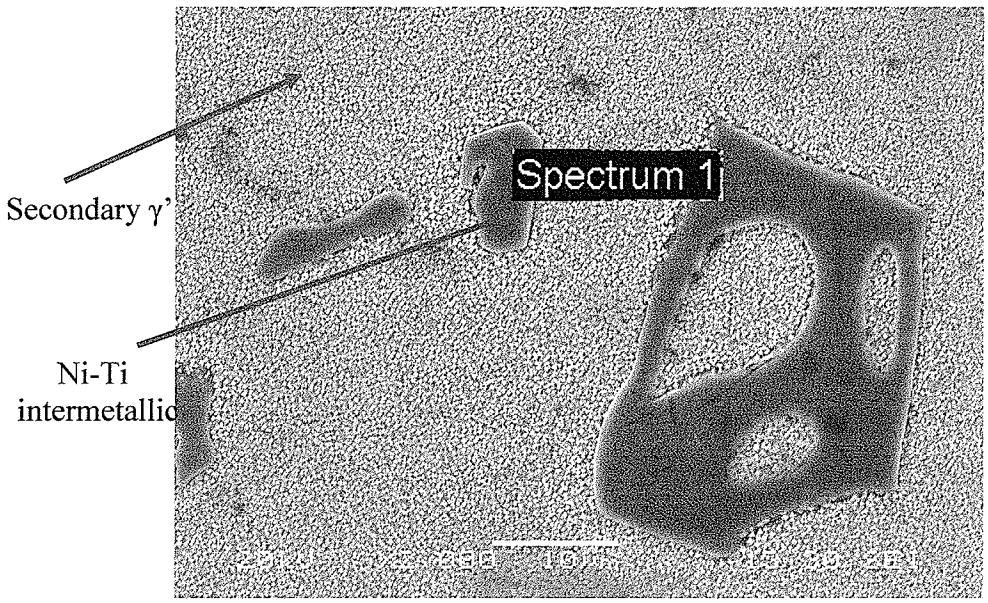

Figure 4-5 SEM SEI Image of As-Received Rene 80 2000x

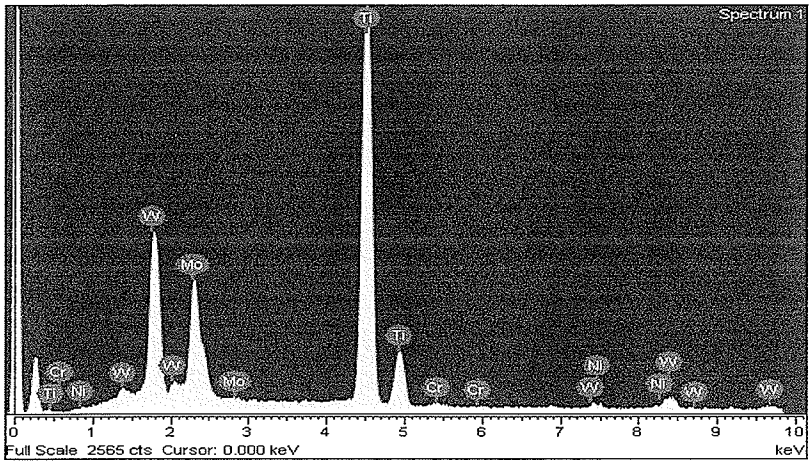

Figure 4-6 EDS Spectrum of Ni-Ti Rich Intermetallic in As-Received Rene 80

4.1.4. Rene 80 - UMT Treated

The castings were treated at 1025°C for 16hrs followed by a water quench. In this form they had a hardness of 365 ± 23VPN. After heat treated the γ' coarsened; as well, M_6C carbides were found along grain boundaries. An example of the UMT heat treated microstructure including several Ni-Ti intermetallics can be viewed in Figure 4-7. The EDS spectrum for the intermetallic can be seen in Figure 4-8. An EDS image and spectrum of a Ti-Zr rich sulphocarbide can be seen in Figure 4-9.

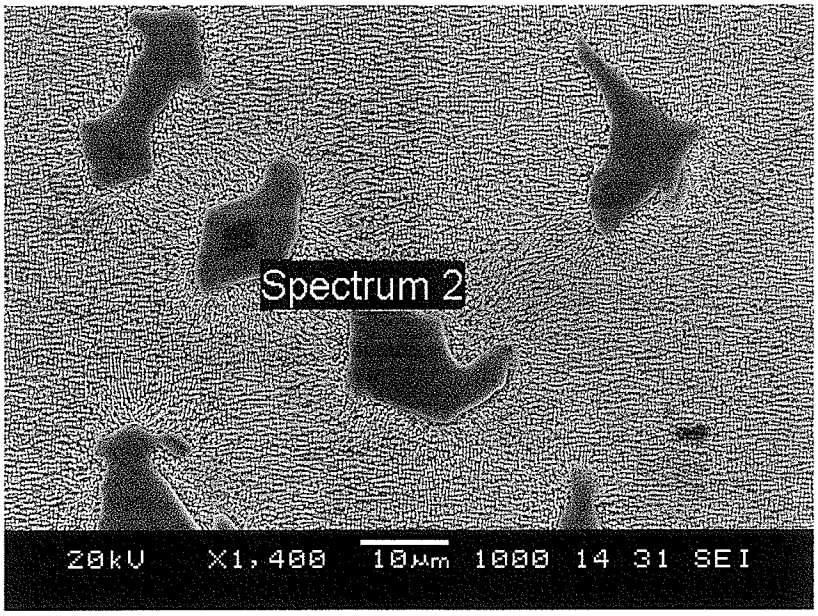

Figure 4-7 SEM SEI Image of UMT Heat Treated Rene 80 1400x

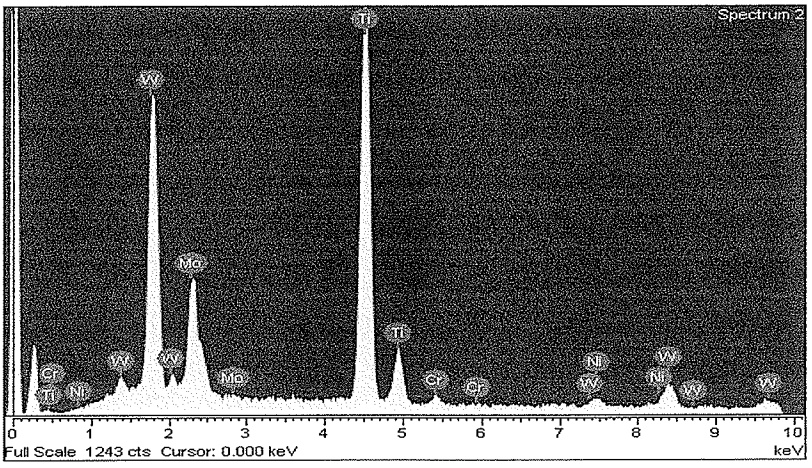

Figure 4-8 EDS Spectrum for Rene 80 Heat Treated Intermetallic

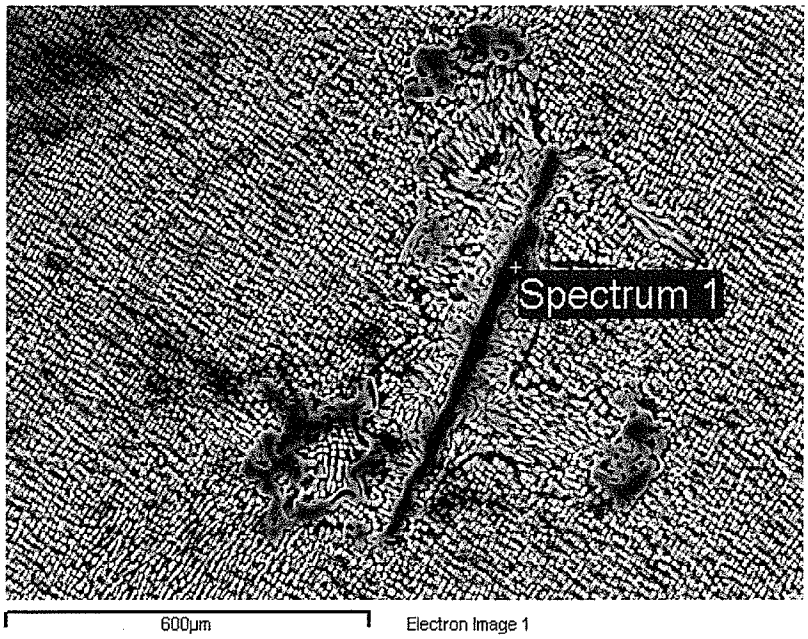

(a)

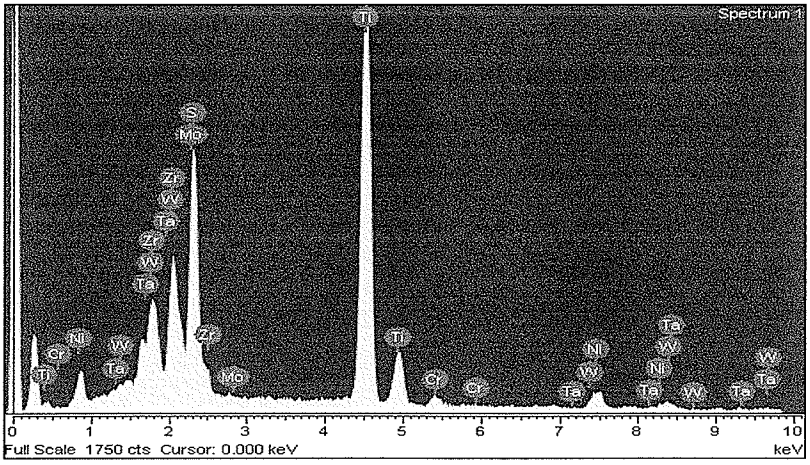

(b)

Figure 4-9 (a) EDS Image and (b) Spectrum of a Ti-Zr Rich Sulphocarbide

4.1.5. Single Crystal – As-Received

The as-received castings were provided solution heat treated at 1289°C for 2hrs followed by a slow furnace cool. In this condition, the castings had a hardness of 444 ± 15VPN. Only primary γ' was found along with some MC carbides rich in Ta and Hf. The as-received microstructure can be seen in Figure 4-10. No EDS spectrums will be given due to the confidential nature of the material.

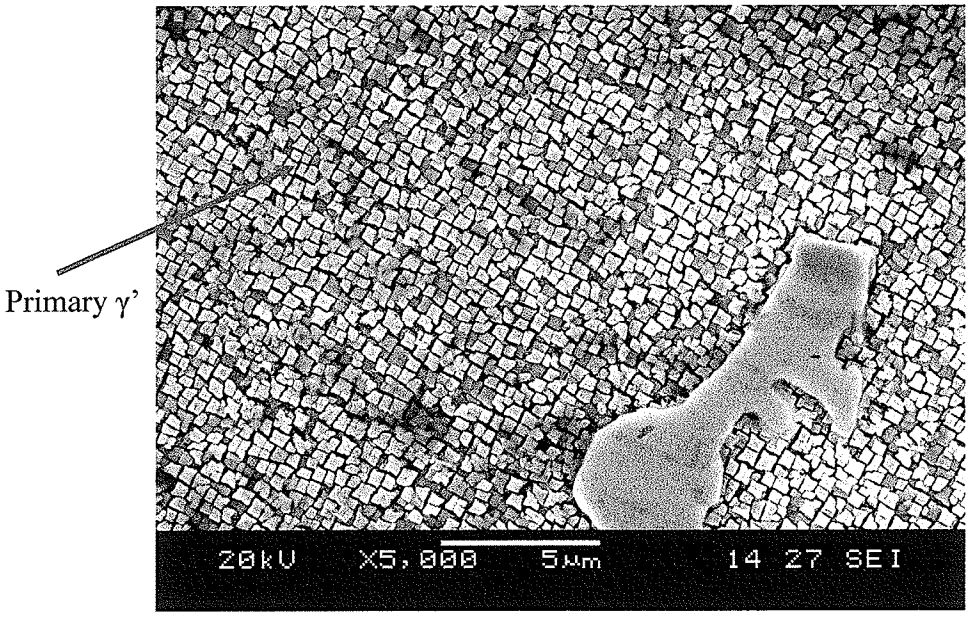

Figure 4-10 SEM SEI Image of As-Received SX 5000x

4.1.6. Single Crystal - UMT Treated

After heat treating at 1200°C for 16hrs followed by an ice water quench, the castings had a hardness of 410 ± 20VPN. Very few changes to the microstructure were evident, only some coarsening of the γ' as shown in Figure 4-11. Some γ' particles were observed to form long chains. This type of formation can also be seen in Figure 4-11.

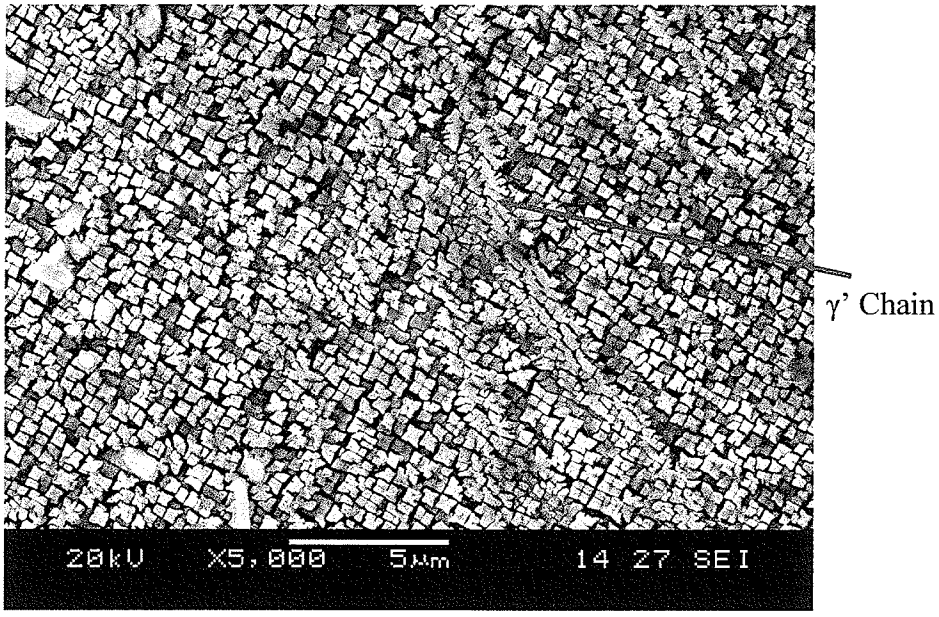

Figure 4-11 SEM SEI Image of UMT Heat Treated SX 5000x

4.2. Crack Length Measurement

Cracking was measured in the heat affected zone and the weld fusion area. Total cracking for the each sample was obtained by adding these two measured lengths together. The area of both the heat affected zone and the weld area were also measured and the total affected area was obtained by adding these two areas together. The cracking index (CI) for each alloy of interest was calculated which gives a measure of the total

cracking per unit area of interest. The CI was obtained by summing the individual crack length by the area of interest. For example, when the heat affected zone cracking index was calculated the sum of HAZ cracks for a sample were divided by the area of the heat affected zone for that sample. Similarly the weld cracking index was calculated with the total weld area cracking divided by the area of the weld and the total cracking index was calculated by summing the HAZ and weld cracking divided by the sum of the HAZ and weld areas. The cracking index is therefore given by:

$$CI = \frac{\sum_{i=1}^{n} L_i}{A} \tag{10}$$

Where L_i is the length of the crack, n is the number of cracks in the area of interest, and A is the area of interest. These values were then averaged and plotted. There were 330 sections measured which contained several thousand cracks. The measured data as well as the calculated depth ratios and cracking indices can be found in Appendix A Tables A1 – A3. A summary of this data including minimum, maximum and average values can be found in Tables 4-1 through 4-3.

Table 4-1 IN 738 Data Summary

		Weld Depth from parent material (mm)	Weld Width at Half Max (mm)	Weld Top Width (mm)	Crack Length in HAZ (mm)	Crack Length in Weld (mm)	Total Crack Length (mm)	Weld Area (mm^2)	HAZ Area (mm^2)	CI Weld (/mm)	CI Total (/mm)
Sample 2	Average	2.4	2.5	5.5	0.7	0.0	0.7	8.26	0.59	0.00	0.08
	Max	2.6	2.8	5.8	1.2	0.0	1.2	8.98	0.82	0.00	0.14
	Min	1.9	2.1	5.2	0.3	0.0	0.3	7.48	0.43	0.00	0.04
Sample 3	Average	3.7	1.8	4.7	1.5	0.0	1.5	8.48	0.56	0.00	0.17
	Max	3.9	1.8	5.3	2.6	0.0	2.6	9.28	0.73	0.00	0.30
	Min	3.1	1.7	4.4	0.6	0.0	0.6	7.89	0.40	0.00	0.07
Sample 4	Average	5.6	1.2	3.4	0.5	1.2	1.7	8.36	0.59	0.14	0.19
	Max	5.9	1.2	3.7	1.0	6.7	7.3	8.76	0.75	0.79	0.80
	Min	4.8	1.1	3.2	0.2	0.0	0.2	7.89	0.46	0.00	0.02
Sample 5	Average	5.5	1.1	3.9	0.9	0.4	1.4	8.35	0.61	0.05	0.15
	Max	5.8	1.2	4.1	2.0	4.2	5.2	8.80	0.78	0.48	0.56
	Min	5.2	1.0	3.8	0.5	0.0	0.5	7.79	0.33	0.00	0.05
Sample 6	Average	3.8	1.6	4.8	1.0	0.3	1.4	8.54	0.64	0.04	0.15
	Max	4.0	1.6	5.1	3.6	3.1	4.3	9.19	0.85	0.36	0.47
	Min	3.3	1.5	4.5	0.0	0.0	0.0	7.71	0.45	0.00	0.00
Sample 7	Average	2.3	2.9	5.5	0.6	0.0	0.6	7.27	0.52	0.00	0.08
	Max	2.4	3.2	5.7	1.6	0.2	1.6	7.94	0.59	0.03	0.21
	Min	2.2	2.6	5.3	0.2	0.0	0.2	6.52	0.41	0.00	0.03

		Weld Depth from parent material (mm)	Weld Width at Half Max (mm)	Weld Top Width (mm)	Crack Length in HAZ (mm)	Crack Length in Weld (mm)	Total Crack Length (mm)	Weld Area (mm^2)	HAZ Area (mm^2)	CI Weld (/mm)	CI Total (/mm)
Sample 9	Average	2.2	9.0	9.0	2.0	0.0	2.0	19.81	2.41	0.00	0.09
	Max	2.5	9.0	9.0	4.6	0.0	4.6	21.31	3.11	0.00	0.21
	Min	2.1	9.0	9.0	0.6	0.0	0.6	19.18	1.86	0.00	0.03
Sample 10	Average	2.3	4.3	7.2	0.2	0.0	0.2	10.16	2.70	0.00	0.02
	Max	2.4	4.9	8.0	0.7	0.0	0.7	10.52	3.85	0.00	0.06
	Min	2.1	3.9	6.7	0.0	0.0	0.0	9.67	1.57	0.00	0.00
Sample 11	Average	9.6	1.8	7.3	6.1	2.2	8.3	23.36	5.20	0.11	0.32
	Max	9.7	1.9	7.6	9.5	5.2	12.5	24.41	5.95	0.24	0.46
	Min	9.1	1.6	7.0	3.8	0.0	4.9	21.94	4.72	0.04	0.23
Sample 12	Average	8.1	1.4	4.9	2.4	1.7	4.1	13.55	2.12	0.12	0.26
	Max	8.5	1.4	5.4	3.6	3.2	5.7	14.41	2.65	0.24	0.37
	Min	7.4	1.3	4.5	1.4	0.1	2.4	12.38	1.57	0.01	0.16
Sample 13	Average	6.1	0.9	3.1	0.9	0.5	1.5	6.98	0.75	0.07	0.19
	Max	6.3	0.9	3.4	1.6	1.2	2.5	7.29	0.99	0.18	0.32
	Min	5.8	0.8	2.8	0.6	0.0	0.6	6.69	0.64	0.00	0.08

Table 4-2 Rene 80 Data Summary

		Weld Depth from parent material (mm)	Weld Width at Half Max (mm)	Weld Top Width (mm)	Crack Length in HAZ (mm)	Crack Length in Weld (mm)	Total Crack Length (mm)	Weld Area (mm^2)	HAZ Area (mm^2)	CI Weld (/mm)	CI Total (/mm)
Sample 2	Average	2.3	3.2	5.3	0.1	0.0	0.1	7.52	0.72	0.00	0.01
	Max	2.4	3.3	5.7	0.3	0.0	0.3	8.31	0.85	0.00	0.03
	Min	2.2	3.0	5.1	0.0	0.0	0.0	7.31	0.51	0.00	0.00
Sample 3	Average	3.4	1.8	4.9	0.5	0.3	0.8	8.48	0.86	0.03	0.08
	Max	3.6	1.9	5.4	1.5	1.6	3.1	9.48	1.11	0.19	0.35
	Min	3.2	1.8	4.6	0.0	0.0	0.0	8.21	0.45	0.00	0.00
Sample 4	Average	4.8	1.3	3.7	0.7	0.0	0.7	8.62	0.79	0.00	0.08
	Max	5.1	1.4	3.8	1.1	0.3	1.1	9.04	1.22	0.04	0.11
	Min	4.6	1.3	3.5	0.2	0.0	0.2	8.36	0.51	0.00	0.02
Sample 5	Average	5.6	1.0	3.9	0.9	0.2	1.1	8.42	0.84	0.02	0.12
	Max	6.1	1.1	4.1	2.2	1.8	2.2	8.86	1.40	0.22	0.22
	Min	5.2	1.0	3.8	0.0	0.0	0.4	8.20	0.52	0.00	0.04
Sample 6	Average	3.6	1.6	4.8	1.0	0.0	1.0	8.39	0.70	0.00	0.11
	Max	3.7	1.7	5.2	1.7	0.0	1.7	9.45	0.89	0.00	0.17
	Min	3.5	1.5	4.6	0.4	0.0	0.4	7.90	0.55	0.00	0.04
Sample 7	Average	2.2	3.0	5.3	0.1	0.0	0.1	7.33	0.48	0.00	0.01
	Max	2.3	3.4	5.6	0.2	0.0	0.2	7.60	0.65	0.00	0.03
	Min	1.9	2.8	4.5	0.0	0.0	0.0	6.79	0.35	0.00	0.00

		Weld Depth from parent material (mm)	Weld Width at Half Max (mm)	Weld Top Width (mm)	Crack Length in HAZ (mm)	Crack Length in Weld (mm)	Total Crack Length (mm)	Weld Area (mm^2)	HAZ Area (mm^2)	CI Weld (/mm)	CI Total (/mm)
Sample 9	Average	2.5	9.8	9.0	0.5	0.0	0.5	18.06	4.50	0.00	0.02
	Max	2.7	9.8	9.0	1.1	0.0	1.1	18.54	5.32	0.00	0.05
	Min	2.4	9.8	9.0	0.0	0.0	0.0	17.39	3.83	0.00	0.00
Sample 10	Average	1.7	6.3	7.1	0.3	0.0	0.3	10.24	4.91	0.00	0.02
	Max	1.9	7.0	7.4	1.6	0.0	1.6	10.49	5.94	0.00	0.10
	Min	1.4	5.8	7.0	0.0	0.0	0.0	9.46	1.73	0.00	0.00
Sample 11	Average	9.5	1.7	7.2	5.3	2.3	7.6	22.58	5.91	0.10	0.27
	Max	10.2	1.9	7.6	7.8	4.2	10.1	23.43	7.44	0.19	0.34
	Min	8.1	1.6	7.0	2.5	1.4	5.5	21.60	4.61	0.06	0.19
Sample 12	Average	7.8	1.3	4.9	0.8	0.3	1.2	13.13	2.05	0.02	0.08
	Max	8.7	1.4	5.4	1.8	1.8	2.5	13.76	2.78	0.14	0.17
	Min	7.0	1.3	4.6	0.2	0.0	0.2	12.57	1.20	0.00	0.01
Sample 13	Average	6.3	0.9	3.2	0.2	0.1	0.4	7.36	1.45	0.02	0.04
	Max	6.8	1.0	3.3	0.8	1.2	2.0	7.74	1.81	0.17	0.22
	Min	5.8	0.9	3.1	0.0	0.0	0.0	7.00	1.13	0.00	0.00

Table 4-3 SX Data Summary

		Weld Depth from parent material (mm)	Weld Width at Half Max (mm)	Weld Top Width (mm)	Crack Length in HAZ (mm)	Crack Length in Weld (mm)	Total Crack Length (mm)	Weld Area (mm^2)	CI Weld (/mm)
Sample 2	Average	2.2	3.0	5.4	0.0	0.6	0.6	7.29	0.08
	Max	2.5	3.3	6.4	0.0	2.2	2.2	8.18	0.31
	Min	1.8	2.2	5.0	0.0	0.0	0.0	6.96	0.00
Sample 3	Average	3.4	1.9	4.9	0.0	5.6	5.6	7.94	0.75
	Max	3.6	2.0	5.8	0.0	9.2	9.2	9.13	1.16
	Min	3.0	1.8	4.5	0.0	3.8	3.8	7.66	0.54
Sample 4	Average	4.7	1.4	3.5	0.0	4.3	4.3	8.02	0.54
	Max	5.1	1.5	4.1	0.0	6.4	6.4	8.30	0.82
	Min	4.1	1.3	3.1	0.0	1.3	1.3	7.79	0.16
Sample 5	Average	5.8	1.0	3.7	0.0	5.4	5.4	7.80	0.69
	Max	6.2	1.1	4.0	0.0	14.5	14.5	8.49	1.85
	Min	5.2	0.9	3.5	0.0	2.8	2.8	7.40	0.38
Sample 6	Average	3.7	1.6	4.7	0.0	8.3	8.3	7.98	1.05
	Max	3.9	1.8	5.3	0.0	13.7	13.7	8.91	1.72
	Min	3.5	1.5	4.4	0.0	2.8	2.8	7.57	0.35
Sample 7	Average	2.2	3.1	5.3	0.0	1.2	1.2	6.91	0.18
	Max	2.3	3.3	5.8	0.0	4.4	4.4	7.50	0.66
	Min	1.9	2.8	5.1	0.0	0.0	0.0	6.46	0.00

		Weld Depth from parent material (mm)	Weld Width at Half Max (mm)	Weld Top Width (mm)	Crack Length in HAZ (mm)	Crack Length in Weld (mm)	Total Crack Length (mm)	Weld Area (mm^2)	CI Weld (/mm)
Sample 9	Average	3.2	9.0	9.0	0.0	0.0	0.0	16.90	0.00
	Max	3.4	9.0	9.0	0.0	0.0	0.0	18.03	0.00
	Min	2.8	9.0	9.0	0.0	0.0	0.0	15.64	0.00
Sample 10	Average	2.4	4.1	6.4	0.0	0.0	0.0	9.14	0.00
	Max	2.5	4.3	7.0	0.0	0.0	0.0	9.53	0.00
	Min	2.0	3.8	6.1	0.0	0.0	0.0	8.91	0.00
Sample 11	Average	9.7	1.8	6.8	0.0	12.1	12.1	20.13	0.60
	Max	10.0	1.9	7.7	0.0	15.3	15.3	20.72	0.77
	Min	8.2	1.7	6.0	0.0	9.3	9.3	19.82	0.46
Sample 12	Average	8.1	1.3	4.5	0.0	8.6	8.6	11.74	0.74
	Max	8.8	1.4	5.1	0.0	12.0	12.0	12.04	1.05
	Min	7.4	1.2	4.2	0.0	5.6	5.6	11.29	0.48
Sample 13	Average	6.2	0.9	3.0	0.0	3.8	3.8	6.38	0.59
	Max	6.6	0.9	3.3	0.0	4.9	4.9	6.73	0.73
	Min	5.9	0.8	2.8	0.0	3.0	3.0	5.83	0.48

4.3. Effect of Focus Coil Current

The electron beam can be focused sharply on the surface of the work piece, above the work piece, or below the work piece by varying the current supplied to the focus coils. By altering this parameter the shape of the weld can be varied greatly without changing the heat input. By examining Figure 4-12 it can be seen that the weld shape varies from a bowl shape to a champagne glass to a spike by focusing the beam far below, then below and then sharply above the surface of the work piece. This effect is mirrored if the beam is focused progressively further above the surface of the workpiece (i.e. a bowl shape can be obtained by focusing the beam far above the surface). The weld shape will be a bowl when the beam is focused far above the surface of the workpiece and change to a champagne glass shape as the beam is focused closer to the surface of the workpiece. This effect was observed for all three alloys; however the effect of varying the focus coil current on the cracking index of the alloy was different for each. The focus coil current for each sample is also given in Figure 4-12. All other welding variables can be found in Table 3-3.

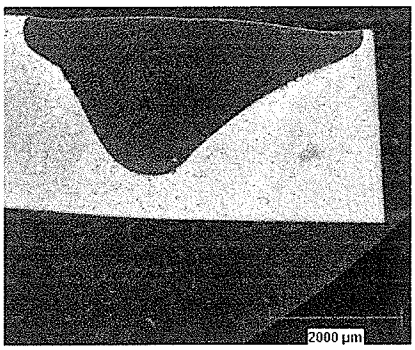

(a) 505mA

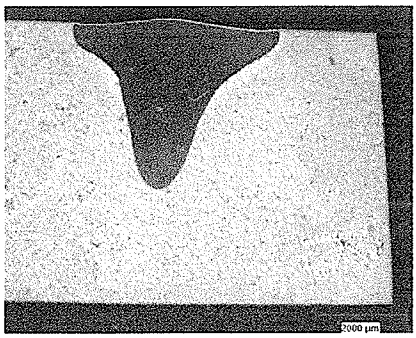

(b) 513mA

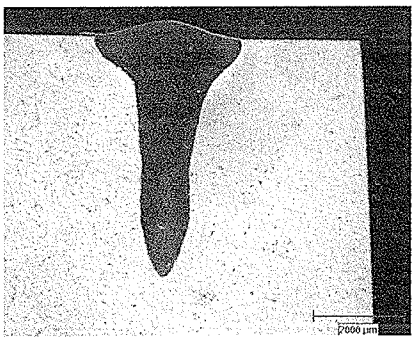

(c) 520mA

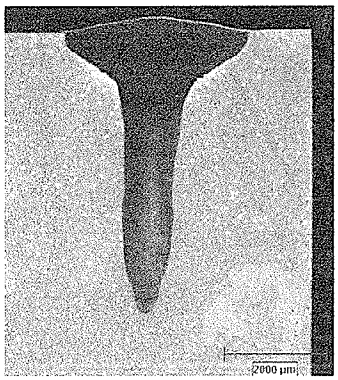

(d) 541mA

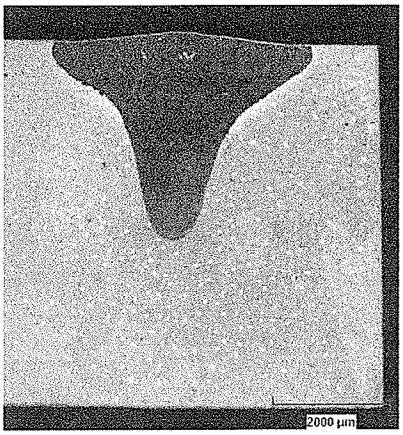

(e) 548mA

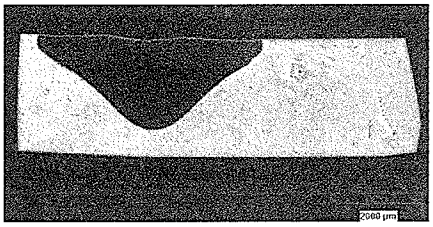

(f) 558mA

Figure 4-12 Optical Micrographs of Weld Shapes for IN 738 Samples 2-7 10x

4.3.1. IN 738

It can be seen from Figure 4-13 that heat affected zone cracking can be greatly reduced by using very large defocus when considering the raw data. Weld cracking was completely eliminated by using large defocus values. These effects indicate that shape has a great affect on the cracking susceptibility of the weld. It appears that the data points for focus values of 520 (sample 4) do not fit the overall trends as shown in Figure 4-13. Heat affected zone cracking for this data point was likely reduced due to an increase in weld zone cracking. Even though weld cracking and heat affected zone cracking cannot be explained by an appropriate trend line, total cracking still correlates very well to focus. It was found that the crack length correlates to focus values with a R^2=0.89 by:

$$Total\ Crack\ Length_{IN\ 738} = -.0015(Focus)^2 + 1.5729(Focus) - 415.07 \qquad (11)$$

although cracking can be reduced by using large defocus values, the total cracking is still very significant at approximately 0.7mm for a 2mm deep weld with a bowl shape. Deeper welds that had a spike weld shape had significantly more overall cracking.

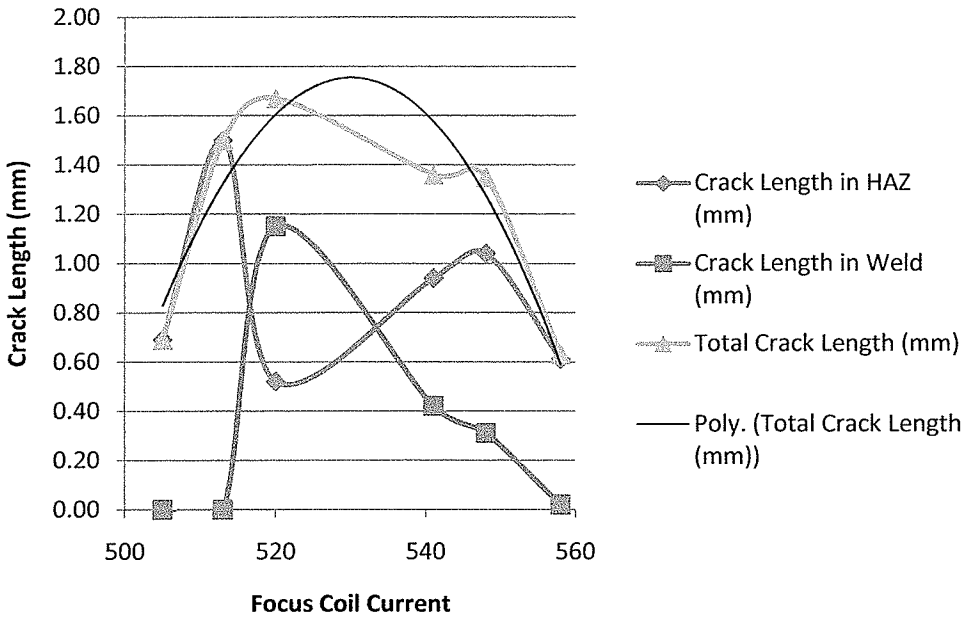

Figure 4-13 IN 738 Raw Data

By normalizing the raw data with the cracking index, the effect of varying parameters is eliminated. It can be seen from Figure 4-14 that weld cracking and total cracking are not affected by varying the focus coil current and therefore do not correlate to this parameter. As mentioned above, the heat affected zone cracking value does not follow the trend for focus values of 520. The cracking index value for this point also does not fit the overall trend, so a second graph was generated without this data point. This graph can be seen in Figure 4-15. When this data point is eliminated the heat affected zone cracking index correlates reasonably well to focus coil current with a R^2 value of 0.45. The correlation is:

$$HAZ\ Cracking\ Index_{IN\ 738} = -.0012(Focus)^2 + 1.2844(Focus) - 335.56. \quad (12)$$

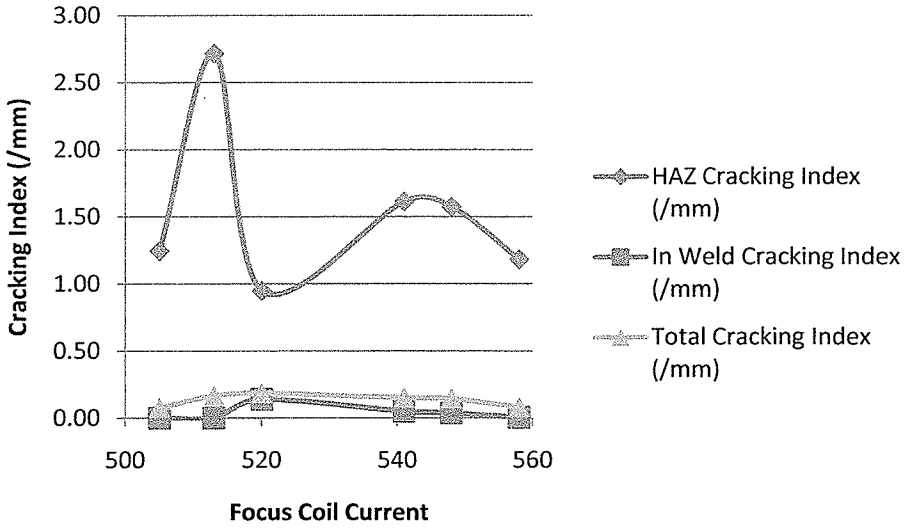

Figure 4-14 IN 738 Normalized Data

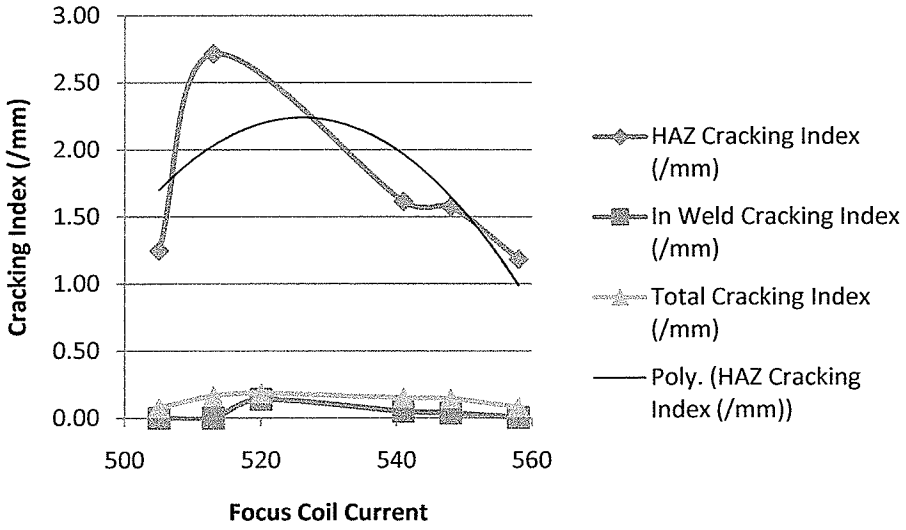

Figure 4-15 Normalized IN 738 Data Without Sample 3

4.3.2. Rene 80

HAZ cracking was least for largely defocused beam values and most for sharp focus when considering the raw data. The weld cracking index was independent of focus, and nearly zero for all test parameters. This can be seen in Figure 4-16. These effects again indicate that weld shape has a great effect on the heat affect zone cracking susceptibility of the alloy. It was found that total cracking correlates very well to focus coil current with a R^2 value of 0.90 by:

$$Total\ Crack\ Length_{Rene\ 80} = -.0015(Focus)^2 + 1.618(Focus) - 429.39. \quad (13)$$

Cracking is almost insignificant for large defocus value at less than 0.1mm for a 2mm deep weld with a bowl shape. Again cracking was most for deep weld with a spike shape.

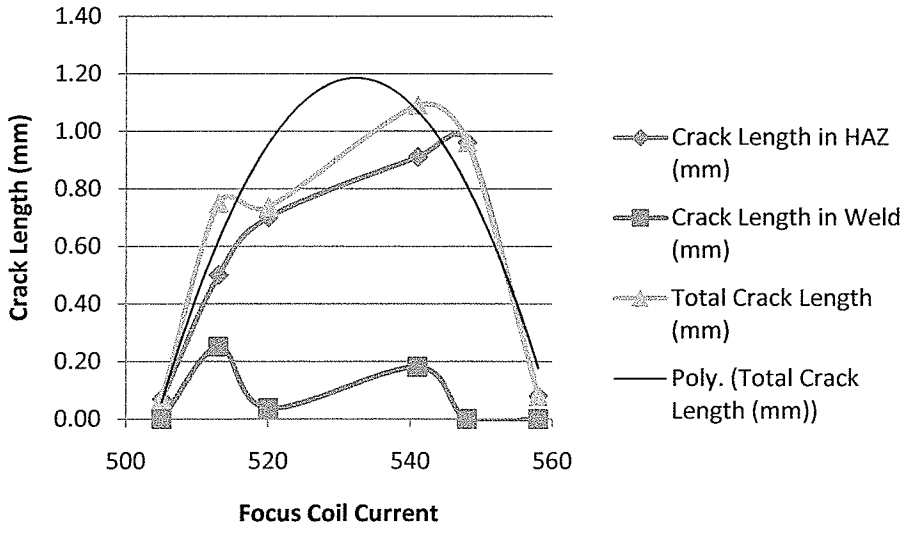

Figure 4-16 Rene 80 Crack Length Data

Data that has been normalized using the cracking index described previously can be seen in Figure 4-17. In weld cracking and total cracking appear independent of focus coil current and do not correlate to this parameter. The heat affected zone cracking index does correlate to focus coil current very well with a R^2 value of 0.82 by:

$$HAZ\ CI_{\ Rene\ 80} = -2E^{-5}(Focus)^3 + .0293(Focus)^2 - 14.7(Focus) + 2452.2 \quad (14)$$

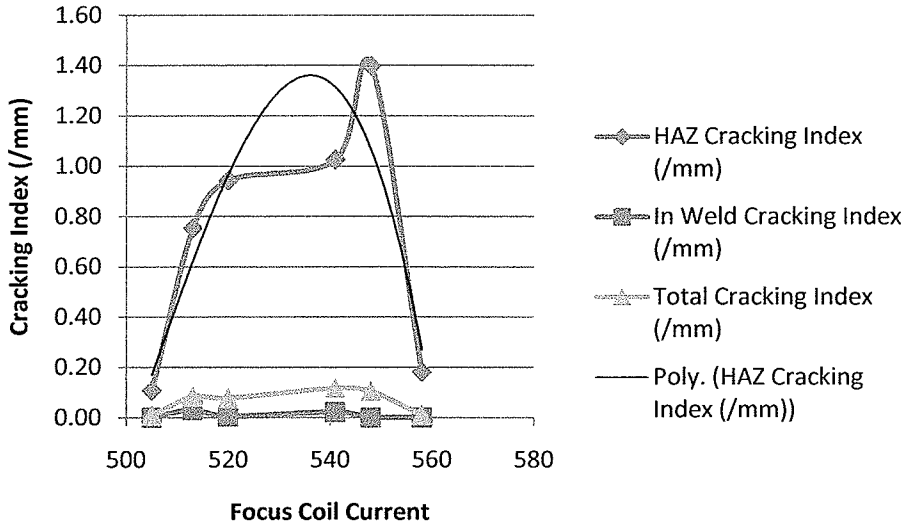

Figure 4-17 Normalized Rene 80

4.3.3. Single Crystal

The proprietary SX cracked only in the weld and was significantly affected by varying focus coil current. This can be seen in Figure 4-18. Since the cracking only occurred in the weld total cracking equals weld cracking. For large values of defocus the weld cracking was greatly reduced. However, cracking was still very significant at over 0.04" (1mm) for weld cracks in a 0.12" (3mm) deep weld. This once again indicates that

the shape of the weld has a great effect on the cracking susceptibility of this alloy as well. The focus coil current correlates very well to both cracking index and crack length for the normalized and raw data respectively. The correlation for crack length had a R^2 value of 0.62 and is:

$$In\ Weld\ Crack\ Length_{SX} = -.0081(Focus)^2 + 8.6464(Focus) - 2297.7. \quad (15)$$

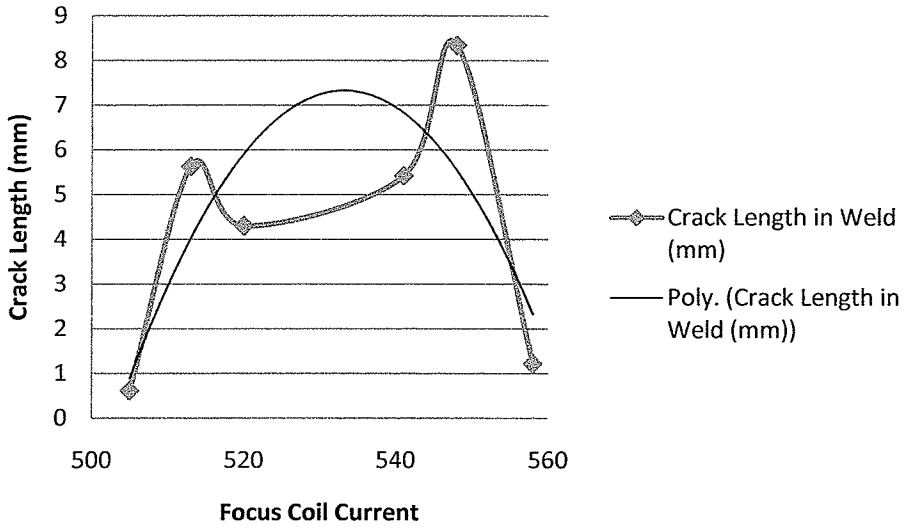

Figure 4-18 Raw SX Data

The normalized data can be seen in Figure 4-19. The correlation for the normalized data had a R^2 value of 0.60 and is:

$$In\ Weld\ Cracking\ Index_{SX} = -.001(Focus)^2 + 1.0681(Focus) - 283.83. \quad (16)$$

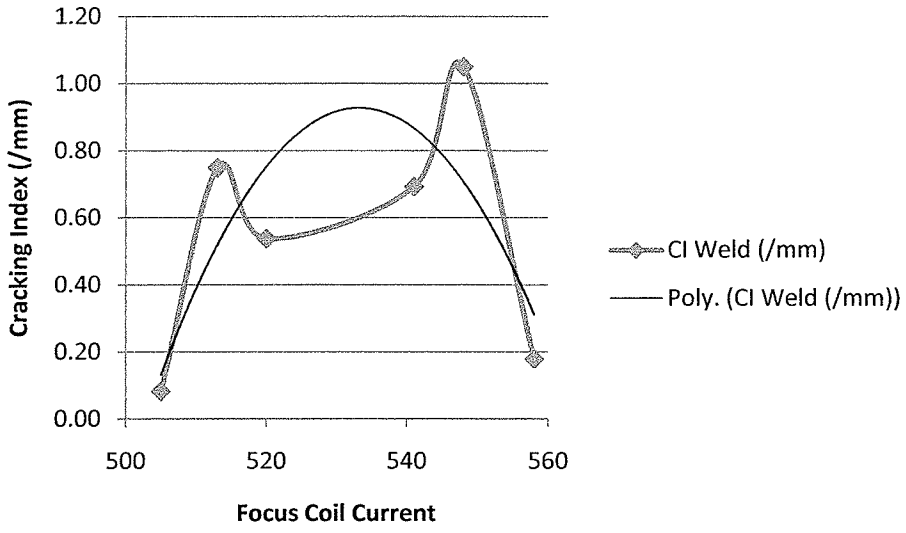

Figure 4-19 Normalized SX Data

4.4. Effect of Welding Velocity

Welding velocity is the speed at which the electron beam translates across the work piece. This velocity is directly related to the heat input rate which is inversely proportional to the welding velocity. Therefore the higher the welding velocity, the lower the heat input rate. For many alloys the CI can be reduced by increasing the heat input rate, or lowering welding velocity. The shape of the weld is also affected by the heat input and can be seen in Figure 4-20. Sample 9 which can be seen in Figure 4-20(a) was welded at a slow speed with a large defocus. This yielded a very wide shallow weld. With an increase in weld speed for sample 10 the shape changed to a bowl which can be seen in Figure 4-20(b). With sharp focus values the weld shape was a spike for all welding velocities. However, the depth of the weld decreased with increasing welding speed. This can be seen with Samples 11, 12 and 13 which are shown in Figure 4-20(c), (d), and (e). Welding speed and focus coil current (FCC) values are also given in Figure 4-20.

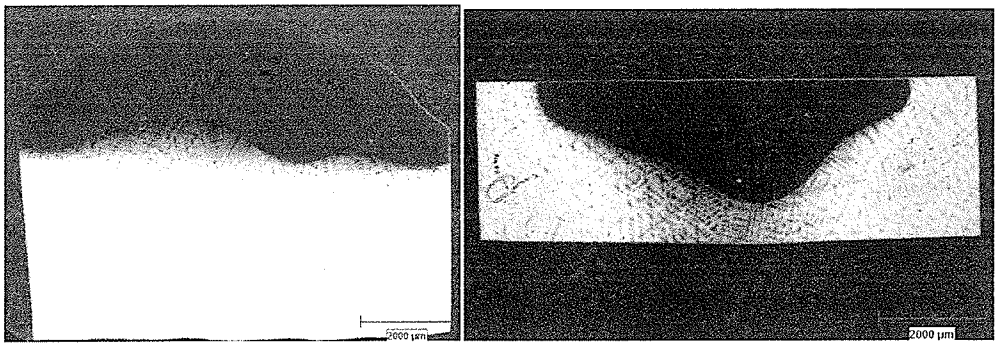

(a) FCC=505mA, V=10ipm (b) FCC=505mA, V=20ipm

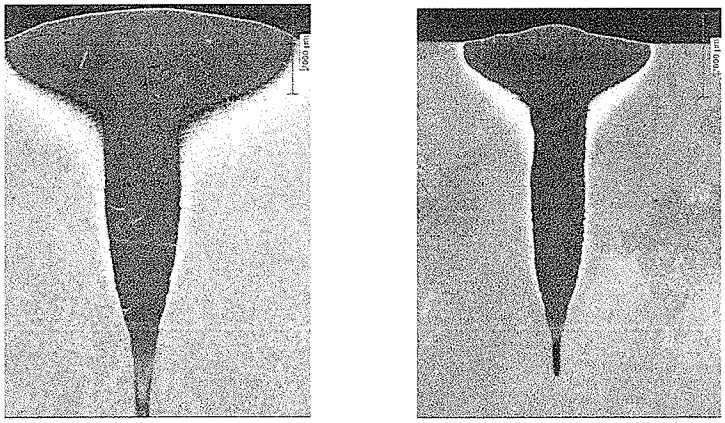

(c) Sharp Focus, V=10ipm (d) Sharp Focus, V=20ipm

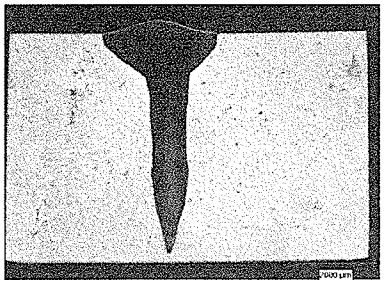

(e) Sharp Focus, V=40ipm

Figure 4-20 Optical Micrographs of Weld Shapes for IN 738 Samples 9-13 10x

Unlike most alloys where the CI can be reduced by using lower welding velocities, for all three alloys tested the CI dropped with increasing welding velocity when considering the raw data. Even when using a defocused beam, the CI was reduced with an increase in velocity.

4.4.1. IN 738

Both HAZ cracking and weld cracking was greatly reduced with increasing welding velocity for a sharply focused beam when considering the raw data. This can be seen in Figure 4-21. For a defocused beam cracking was again reduced in the HAZ for increasing weld velocities, but weld cracking was completely eliminated. This indicates that weld shape is again greatly affecting the cracking behaviour but that welding velocity also has a great effect as the weld shape was similar for all focused trials. Cracking was almost eliminated by using a defocused beam and medium welding velocities. By increasing the welding velocity further the cracking may be completely eliminated. For a defocused beam the total crack length correlates to welding speed with a R^2 value of 0.99 by:

$$Total\ Crack\ Length_{Focused\ IN738} = 13.939e^{-.135(Velocity)}. \quad (17)$$

Since there was no weld cracking the total cracking equals the heat affected zone cracking for the defocused condition. For the defocused condition the relationship is linear with a R^2 value of 1.0 and is given by:

$$Total\ Crack\ Length_{Defocused\ IN738} = -.4252(Velocity) + 3.38. \quad (18)$$

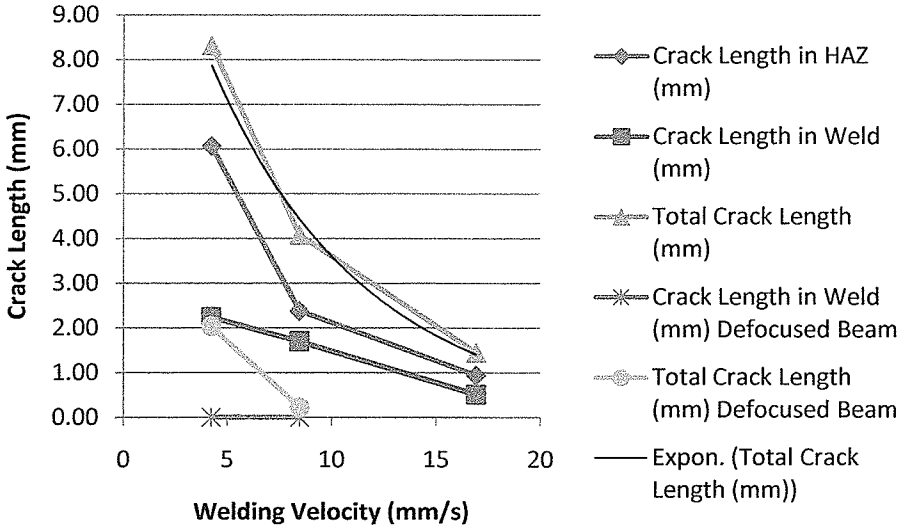

Figure 4-21 IN 738 Welding Speed Data

After normalizing the data using the cracking index, it can be seen in Figure 4-22 that HAZ cracking does not correlate to welding velocity within experimental error. It does appear that both total cracking for a defocused and focused beam slope downward indicating that cracking index is reduced by increasing welding velocity. The relationship between total cracking index and welding velocity is linear with a R^2 value of 0.98 and is given by:

$$Total\ Cracking\ Index_{IN\ 738} = -.01(Velocity) + .3537. \tag{19}$$

Again since there was no weld cracking the heat affected zone cracking index equals the total cracking index. For the defocused condition the trend is also linear with a R^2 value of 1.0 and is given by:

$$Total\ Cracking\ Index_{Defocused\ IN738} = -.0171(Velocity) + .1642. \tag{20}$$

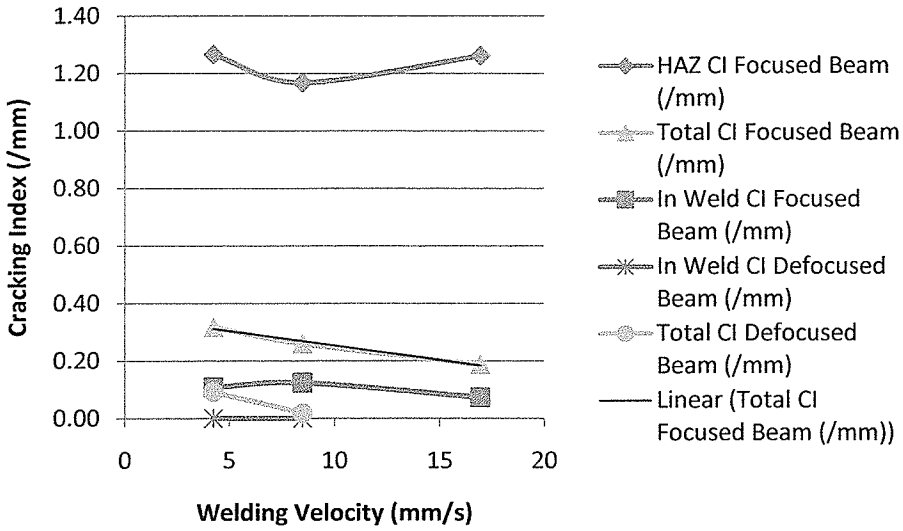

Figure 4-22 IN 738 Normalized Data

4.4.2. Rene 80

HAZ cracking and weld cracking were reduced dramatically by increasing welding velocity for a focused beam as shown in Figure 4-23. This is very similar to the results of IN 738. Since all weld shapes were similar for the focused beam there is a distinct correlation between the welding velocity and the crack susceptibility of Rene 80. HAZ cracking for a defocused beam was reduced by the increasing velocity but not as dramatically. In weld cracking was again eliminated for the defocused beam conditions. The correlation between total crack length for the focused beam was exponential with a R^2 value of 0.90 and is given by:

$$Total\ Crack\ Length_{Focused\ Rene\ 80} = 13.669e^{-.225(Velocity)}. \quad (21)$$

The correlation for total crack length with the defocused condition is linear. It is equal to heat affected zone cracking due to the absence of weld cracking. The correlation has an R^2 value of 1.0 and is:

$$Total\ Crack\ Length_{Defocused\ Rene\ 80} = -0.0543(Velocity) + 0.76. \quad (22)$$

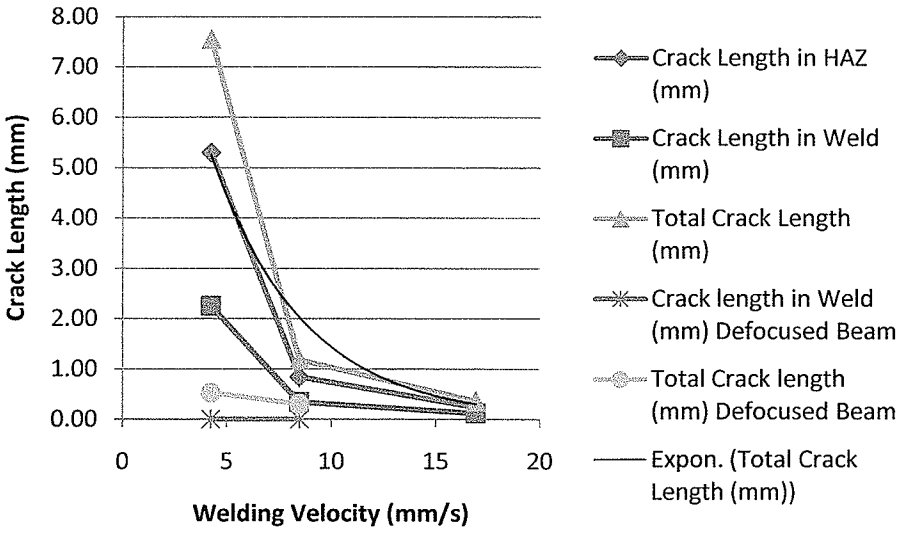

Figure 4-23 Rene 80 Welding Velocity Data

For normalized data only the focused beam condition correlated well to welding velocity as shown in Figure 4-24. The defocused condition may correlate with additional data points, but the cracking index is very small and may be insignificant. For a focused beam the total cracking index correlated to welding velocity with a R^2 of 0.97 with a power relationship given by:

$$Total\ Cracking\ Index_{Defocused\ Rene\ 80} = 1.7085(Velocity)^{-1.359}. \quad (23)$$

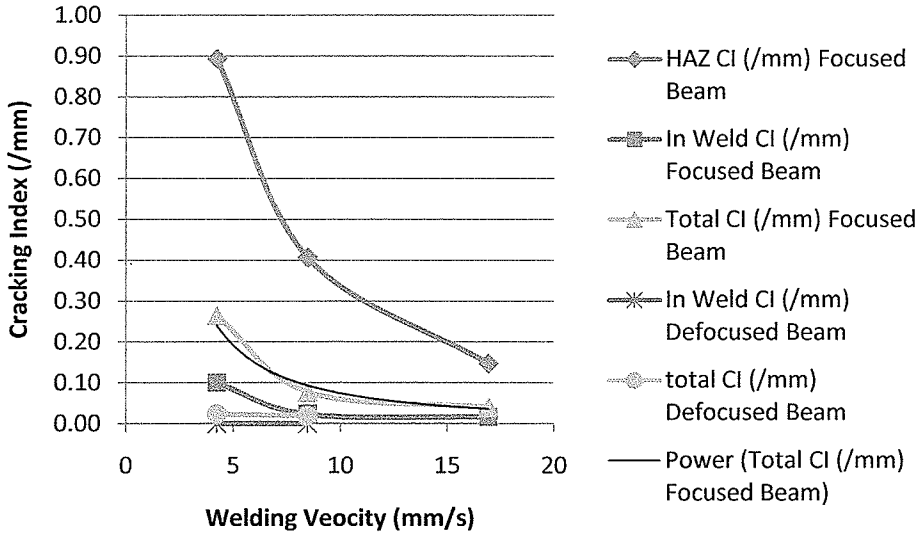

Figure 4-24 Rene 80 Welding Velocity Normalized Data

4.4.3. Single Crystal

There was no heat affected zone cracking for any of the SX samples so weld cracking equals total cracking for all cases. For the defocused welding condition cracking was completely eliminated. For the focused condition weld cracking reduced significantly with increasing welding velocity. These results can be seen in Figure 4-25. Weld shape was similar for all focused trials which indicates that welding velocity has a strong impact on the cracking susceptibility of the alloy when considering the raw data. However, when the cracking index has been applied to normalize the data, there appears to be no correlation between weld cracking and welding velocity as shown in Figure 4-26. For the focused raw data the trend was linear between welding velocity and cracking with an R^2 value of 0.99 and was given by:

$$Total\ Cracking_{Defocused\ SX} = -.6393(Velocity) + 14.475. \quad (24)$$

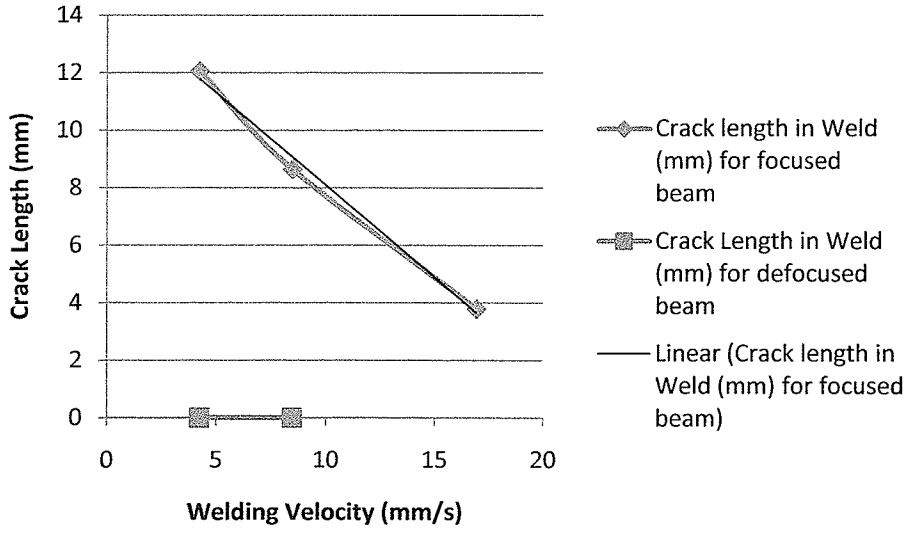

Figure 4-25 Raw SX Data

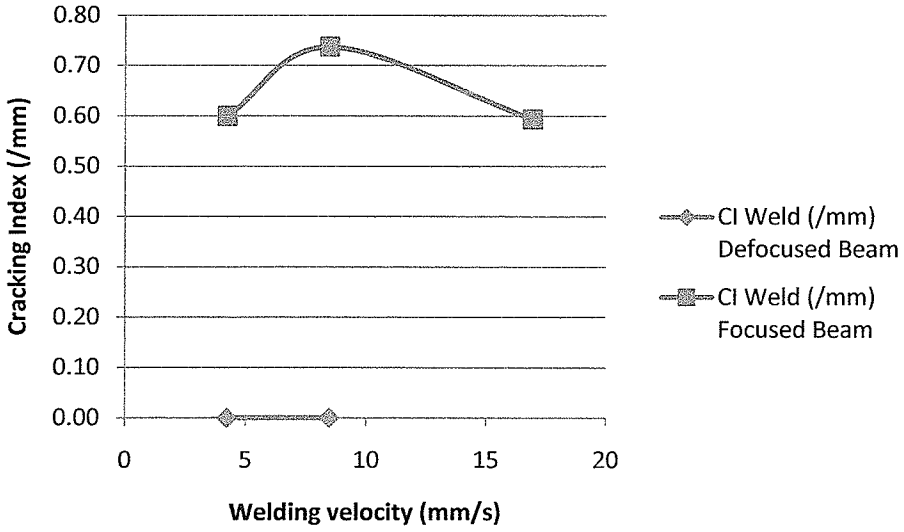

Figure 4-26 Normalized SX Data

4.5. Orientation Image Microscopy (OIM) Analysis

This technique was be used to determine the microstructural phase and crystal orientation at specific points of the sample (Orientation Imaging Microscopy). The grey scale in the image indicates the quality of the Kikuchi pattern. The lighter points correlate to a more confident pattern.

4.5.1. Rene 80

Figure 4-27 was obtained by performing an OIM analysis on Rene 80 sample number 12. The magnification used was 200x and the step size was 4μm. It can be seen that there are no grains present on the left side of the Figure, while there are abundant stray grains on the right side. The heat affected zone of the weld is to the left of the Figure while the center of the weld is at the right of the Figure. A crack is evident as shown in red and continues into the area toward the right side of the Figure where the grains are present.

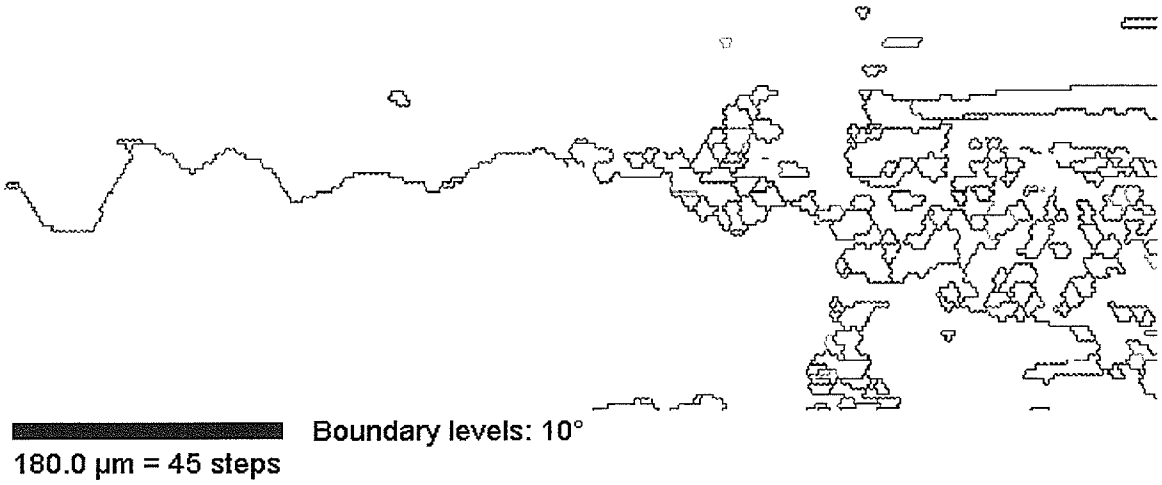

Figure 4-27 Rene 80 OIM Image

4.5.2. Single Crystal

Figure 4-28 was obtained by performing an OIM analysis on Sample 3 over the cracked area. The step sized used was 6μm and magnification on the SEM was 100x. It can be seen that there are many stray grains present around the crack which is shown in black near the center of the Figure. There are abundant stray grains on the right side of the crack which extend onto the left side of the crack. The single crystal structure tends to be maintained on the left side of the crack even with the extension of the new grains. This tends to support the findings of Park (Park, Babu, Vitek, Kenik, & David, 2003).

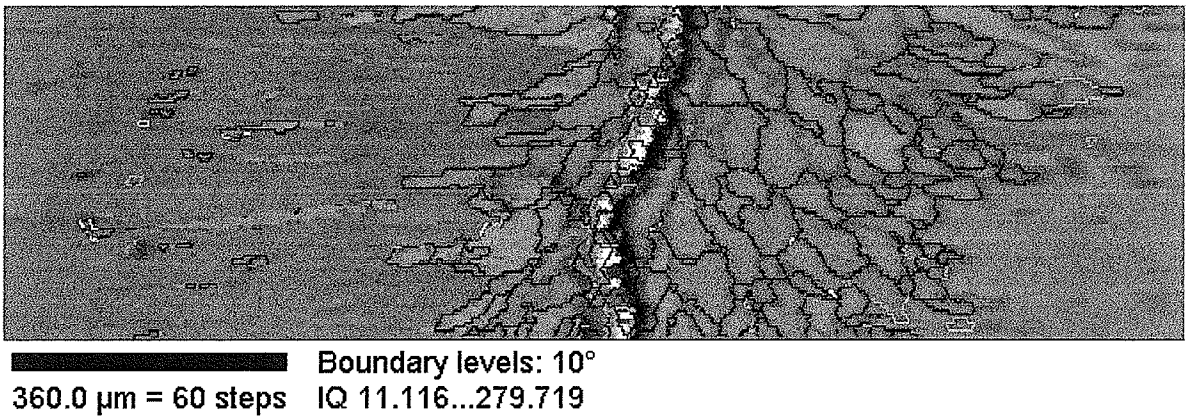

Figure 4-28 SX OIM Image

5.0 Conclusion

In the present study, the effect of welding parameters on the heat affected zone and weld cracking susceptibility was studied on Inconel 738, Rene 80, and a proprietary single crystal nickel based Superalloy. The alloys were studied under a scanning electron microscope to determine their as-received and post heat treated microstructures. The effect of varying welding parameters was investigated through changing welding speed and focus coil current on 11 samples of ranging thicknesses on each alloy. The welded samples were then sectioned and the average total, weld, and HAZ cracking index was measured using an optical microscope equipped with an image analysis system. The following conclusions were obtained by examining the plots of cracking index verses welding parameter:

1. The hardness of all three alloys can be significantly reduced by heat treating using the UMT treatment procedures. The degree of hardness reduction was affected by the thickness of the material.
2. IN 738 had an initial microstructure consisting of primary and secondary γ' with typical carbides. The microstructure was unaffected by heat treating other than the addition of $M_{23}C_6$ carbides and coarsening of the γ' phase.
3. Rene 80 exhibited a base microstructure of fine secondary γ' with MC type carbides along with several intermetallics. After heat treating the gamma prime coarsened and there were M_6C carbides present.

4. The proprietary single crystal material had only secondary γ' along with some MC type carbides both pre and post UMT heat treating.
5. By varying the focus coil current and welding speeds the shape of the cross section of the weld is changed. With large defocus the weld is "bowl" shaped, and for sharp focus the weld shape is a "spike" for all three alloys
6. Weld, HAZ and total crack length in each section varied with electron beam welding parameters. A summary of the data is found in Tables 4.2.1 through 4.2.3 while the complete data is found in Appendix A.
7. Cracking in all three alloys can be reduced by using a largely defocused beam during welding. It can also be reduced by using higher welding speeds. By combining a defocused beam and large welding speeds a nearly crack free weld can be obtained.
8. The weld cracking of the proprietary single crystal alloy appears to be caused by the formation of stray grains which supports the work of J.M. Vitek et al (Vitek, Babu, David, & Park, 2003).

6.0 Future Work

Based on the achievements of the present study, the following future work is suggested:

1. The results have shown that welding velocity and focus coil current both play a large role in the cracking susceptibility of all three alloys. Thus, cracking may be completely eliminated by further increasing the velocity and defocus. Further studies should be conducted to determine if cracking may be eliminated with increased values.
2. There are many more processing parameters such as working distance, oscillation, spin, current, and accelerating voltage that can vary the electron beam weld which have not been considered in this study. Further studies could investigate the contribution of these parameters to the cracking susceptibility of the alloys.
3. Further microstructural analysis should be undertaken to determine the cracking mechanisms present in each alloy.

7.0 References

Banjeree, K., Richards, N., & Chaturvedi, M. (July 2005). Effect of Filler Alloys on Heat Affected Zone Cracking in Preweld Heat Treated IN 738 LC Gas-Tungsten-Arc Welds. *Metallurgical and Materials Transactions vol36A* , 1881-90.

Cai, C., Liaw, P., Ye, M., & Yu, J. (1999, April). *Recent Developments in Thermomechanical Fatigue Life Prediction of Superalloys.* Retrieved November 28, 2007, from TMS: http://www.tms.org/pubs/journals/JOM/9904/Cai/Cai-9904.html#ToC1

Chaturvedi, M., Richards, N., & Nakkalil, R. (1991). High Temperature Alloys. *The Thirteenth Canadian Congress on Applied Mechanics*, (p. 102~113). Winnipeg.

Engquist, R. D. (1968, November). Parameters Affecting Electron Beam Welding. *Metals Engineering Quarterly - American Society for Metals* , pp. 56-63.

Gaumann, M. C. (2001). Single Crystal Laser Deposition of Superalloys: Processing-Microstructure Maps. *Acta mater. 49* , 1051–1062.

Gell, M., Duhl, D., & Giamei, A. (1980). The Development of Single Crystal Superalloy Turbine Blades. *Superalloys* , 205-214.

Groover, M. P. (2002). *Fundamentals of Modern Manufacturing, 2nd Edition.* Wiley.

H.A. Shahsavari, A. K. (2007). Effect of Preweld Microstructure on HAZ Liquation Cracking of Rene 80 Superalloy. *Materials Science and Technology vol23 n5* , 547-555.

Haafkens, M. (1982). Blade Repair and Recovery. *High Temperature Alloys for Gas Turbines 1982* (pp. 931-954). D. Reidel Publ Co.

Jena, A., & Chateurvedi, M. (1992). *Phase Transformations in Materials.* Prentice Hall.

Kelly Ferjutz, J. D. (1993). *ASM Handbook: Volume 6: Welding, Brazing, and Soldering.* ASM International Materials Information Society.

Kurz, W. D. (1998). *Fundamentals of Solidification Fourth Revised Edition.* Trans Tech Publications Ltd.

Li, Q. (2006). *The Influence of Electron Beam Welding Parameters on Heat Affected Zone Cracking in Allvac 718Plus Alloy.* Winnipeg, MB: University of Manitoba, Department of Mechanical and Manufacturing Engineering.

Liu, Y. N. (1996). Study on the Effect of the Electron Beam Welding Variables on Heat-Affected-Zone Liquation Cracking and the Relationship of Cracks to Weld Shape in Wrought Incoloy 903.

Liu, Y., Richards, N., & Chateurvedi, M. (1995). The Effect of Beam Oscillation in EB Welding on the Weld Shape and Penetration. *Unpublished work at the University of Manitoba* .

Ojo, O., Richards, N., & Chaturvedi, M. (2004). Contribution of Constitutional Liquation of Gamma Prime Precipitate to Weld HAZ Cracking of Cast Inconel 738 Superalloy. *Scripta Materialia 50* , 641-646.

Orientation Imaging Microscopy. (n.d.). Retrieved March 20, 2008, from Stanford University: http://www.stanford.edu/group/snl/SEM/OIMIntro.htm

Owczarski, W., Duvall, D., & Sullivan, C. (1966). Model for Heat-Affected Zone Cracking in Nickel-Base Superalloys. *Weld Journal vol45 n4* , 145-155.

Paris, P. P. (1963). Fracture Mechanics Approach to Fatigue. *Sagamore Army Materials Research Conference* , 107-132.

Park, J.-W., Babu, S., Vitek, J., Kenik, E., & David, S. (2003). Stray Grain Formation in Single Crystal Ni-Base Superalloy Welds. *Journal of Applied Physics vol 94 n6* , 4203-4209.

Qiang, L. (2006). *The influence of electron beam welding parameters on heat affected zone cracking in Allvac 718plus alloy.* University of Manitoba.

Richards, N., Chaturvedi, M., Liu, Y., & Mount, K. (1996). Optimization of Electron Beam Welding Parameters for Incoloy 903. *International Journal of Materials and Product Technology vol11 n3 of 4* , 284-299.

Ross, E. (Mar 1971). Rene 80: A Cast Turbine Blade Alloy. *Metal Progress, vol99, n3* , 93-94.

Shackelford, J. F. (2000). *Introduction to Materials Science for Engineers 5th Ed.* Upper Saddle River, New Jersey: Prentice Hall.

Sidhu, R., Richards, N., & Chaturvedi, M. (2005). Effect of Aluminium Concentration in Filler Alloys on HAZ Cracking in TIG Welded Cast Inconel 738LC Superalloy. *Materials Science and Technology vol21 n10* , 119-1131.

Spittle, J. (2006). Columnar to Equiaxed Grain Transition in as Solidified Alloys. *International Materials Reviews vol51 n4* , 247-269.

Sullivan, C., & Donachie, M. (Feb. 1967). Some Effects of Microstructure on the Mechanical Properties of Nickel Base Superalloys. *Materials Engineering Quarterly* , 250-258.

Thakur, A., Richards, N., & Chaturvedi, M. (2003). On Crack Free Welding of Cast Inconel 738. *International Journal for the Joining of Materials vol15 part 4* , 21-25.

Vitek, J., Babu, S., David, S., & Park, J. (2003). Microstructure Development in Single Crystal Welds. *Materials Science Forum vol426 n5* , 4123-8.

Appendices

APPENDIX A

A.1 IN 738

Table A-1 IN 738 Raw Data

	Trial	Weld Depth from parent material (mm)	Weld Width at Half Max (mm)	Weld Top Width (mm)	Crack Length in HAZ (mm)	Crack Length in Weld (mm)	Total Crack Length (mm)	Depth/ Weld Top Width	Weld Area (mm^2)	HAZ Area (mm^2)	CI HAZ (/mm)	CI Weld (/mm)	CI Total (/mm)
Sample 2	a	2.5	2.8	5.2	0.6	0	0.6	0.48	7.48	0.57	1.05	0.00	0.07
	b	2.3	2.4	5.6	0.4	0	0.4	0.41	8.59	0.82	0.49	0.00	0.04
	c	2.6	2.7	5.5	0.3	0	0.3	0.47	7.97	0.43	0.69	0.00	0.04
	d	2.6	2.6	5.4	0.7	0	0.7	0.48	8.50	0.50	1.40	0.00	0.08
	e	1.9	2.1	5.5	0.5	0	0.5	0.35	7.91	0.74	0.68	0.00	0.06
	f	2.3	2.3	5.5	1	0	1	0.42	8.32	0.50	2.02	0.00	0.11
	g	2.5	2.5	5.8	0.6	0	0.6	0.43	8.98	0.67	0.90	0.00	0.06
	h	2.4	2.6	5.8	0.9	0	0.9	0.41	8.20	0.60	1.49	0.00	0.10
	I	2.6	2.7	5.7	0.7	0	0.7	0.46	8.40	0.55	1.28	0.00	0.08
	j	2.5	2.6	5.4	1.2	0	1.2	0.46	8.23	0.49	2.46	0.00	0.14
	Average	**2.42**	**2.53**	**5.54**	**0.69**	**0.00**	**0.69**	**0.44**	**8.26**	**0.59**	**1.25**	**0.00**	**0.08**
	Max	**2.60**	**2.80**	**5.80**	**1.20**	**0.00**	**1.20**	**0.48**	**8.98**	**0.82**	**2.46**	**0.00**	**0.14**
	Min	**1.90**	**2.10**	**5.20**	**0.30**	**0.00**	**0.30**	**0.35**	**7.48**	**0.43**	**0.49**	**0.00**	**0.04**

	Trial	Weld Depth from parent material (mm)	Weld Width at Half Max (mm)	Weld Top Width (mm)	Crack Length in HAZ (mm)	Crack Length in Weld (mm)	Total Crack Length (mm)	Depth/ Weld Top Width	Weld Area (mm^2)	HAZ Area (mm^2)	CI HAZ (/mm)	CI Weld (/mm)	CI Total (/mm)
Sample 3	a	3.8	1.7	5.3	1.3	0	1.3	0.72	9.28	0.60	2.15	0.00	0.13
	b	3.9	1.8	4.5	2.6	0	2.6	0.87	8.11	0.66	3.94	0.00	0.30
	c	3.6	1.8	4.4	1.5	0	1.5	0.82	7.89	0.40	3.72	0.00	0.18
	d	3.7	1.8	4.9	1.2	0	1.2	0.76	8.59	0.73	1.64	0.00	0.13
	e	3.9	1.8	4.7	0.8	0	0.8	0.83	8.51	0.40	1.98	0.00	0.09
	f	3.6	1.7	4.4	0.6	0	0.6	0.82	7.89	0.53	1.13	0.00	0.07
	g	3.8	1.8	4.5	2.2	0	2.2	0.84	8.68	0.58	3.79	0.00	0.24
	h	3.6	1.8	4.6	2.3	0	2.3	0.78	8.26	0.52	4.41	0.00	0.26
	l	3.7	1.8	4.7	1.5	0	1.5	0.79	8.52	0.55	2.73	0.00	0.17
	j	3.1	1.8	5.3	1	0	1	0.58	9.08	0.60	1.66	0.00	0.10
	Average	**3.67**	**1.78**	**4.73**	**1.50**	**0.00**	**1.50**	**0.78**	**8.48**	**0.56**	**2.71**	**0.00**	**0.17**
	Max	**3.90**	**1.80**	**5.30**	**2.60**	**0.00**	**2.60**	**0.87**	**9.28**	**0.73**	**4.41**	**0.00**	**0.30**
	Min	**3.10**	**1.70**	**4.40**	**0.60**	**0.00**	**0.60**	**0.58**	**7.89**	**0.40**	**1.13**	**0.00**	**0.07**

Sample 4	a	5.8	1.2	3.4	0.2	0	0.2	1.71	8.69	0.49	0.41	0.00	0.02
	b	5.8	1.2	3.6	0.4	0	0.4	1.61	8.48	0.46	0.87	0.00	0.04
	c	5.8	1.2	3.4	0.6	6.7	7.3	1.71	8.49	0.62	0.97	0.79	0.80
	d	5.6	1.2	3.7	0.8	0	0.8	1.51	8.76	0.46	1.73	0.00	0.09
	e	4.8	1.1	3.5	0.7	1.7	2.4	1.37	7.89	0.53	1.32	0.22	0.29
	f	5.3	1.1	3.4	0.6	0	0.6	1.56	8.22	0.68	0.88	0.00	0.07
	g	5.7	1.1	3.2	0.4	0	0.4	1.78	8.21	0.61	0.65	0.00	0.05
	h	5.9	1.1	3.2	0.3	3.1	3.4	1.84	8.33	0.74	0.40	0.37	0.37
	l	5.8	1.2	3.3	1	0	1	1.76	8.51	0.51	1.98	0.00	0.11
	j	5.5	1.1	3.2	0.2	0	0.2	1.72	8.00	0.75	0.27	0.00	0.02
	Average	**5.60**	**1.15**	**3.39**	**0.52**	**1.15**	**1.67**	**1.66**	**8.36**	**0.59**	**0.95**	**0.14**	**0.19**
	Max	**5.90**	**1.20**	**3.70**	**1.00**	**6.70**	**7.30**	**1.84**	**8.76**	**0.75**	**1.98**	**0.79**	**0.80**
	Min	**4.80**	**1.10**	**3.20**	**0.20**	**0.00**	**0.20**	**1.37**	**7.89**	**0.46**	**0.27**	**0.00**	**0.02**

	Trial	Weld Depth from parent material (mm)	Weld Width at Half Max (mm)	Weld Top Width (mm)	Crack Length in HAZ (mm)	Crack Length in Weld (mm)	Total Crack Length (mm)	Depth/ Weld Top Width	Weld Area (mm^2)	HAZ Area (mm^2)	CI HAZ (/mm)	CI Weld (/mm)	CI Total (/mm)
Sample 5	a	5.7	1	3.8	0.6	0	0.6	1.50	8.21	0.60	0.99	0.00	0.07
	b	5.3	1.1	4.1	0.6	0	0.6	1.29	8.36	0.78	0.77	0.00	0.07
	c	5.4	1.1	3.9	0.6	0	0.6	1.38	8.19	0.33	1.80	0.00	0.07
	d	5.2	1.1	4.1	0.8	0	0.8	1.27	8.20	0.70	1.14	0.00	0.09
	e	5.3	1.2	4	1	4.2	5.2	1.33	8.68	0.57	1.75	0.48	0.56
	f	5.3	1.1	3.8	2	0	2	1.39	7.79	0.63	3.17	0.00	0.24
	g	5.5	1	3.8	1.4	0	1.4	1.45	8.01	0.50	2.81	0.00	0.16
	h	5.6	1	3.8	1	0	1	1.47	8.70	0.70	1.44	0.00	0.11
	l	5.8	1.1	3.8	0.5	0	0.5	1.53	8.80	0.72	0.70	0.00	0.05
	j	5.6	1	3.9	0.9	0	0.9	1.44	8.53	0.58	1.56	0.00	0.10
	Average	**5.47**	**1.07**	**3.90**	**0.94**	**0.42**	**1.36**	**1.40**	**8.35**	**0.61**	**1.61**	**0.05**	**0.15**
	Max	**5.80**	**1.20**	**4.10**	**2.00**	**4.20**	**5.20**	**1.53**	**8.80**	**0.78**	**3.17**	**0.48**	**0.56**
	Min	**5.20**	**1.00**	**3.80**	**0.50**	**0.00**	**0.50**	**1.27**	**7.79**	**0.33**	**0.70**	**0.00**	**0.05**
Sample 6	a	3.8	1.6	4.6	1.1	0	1.1	0.83	8.36	0.50	2.22	0.00	0.12
	b	4	1.5	4.7	1	0	1	0.85	8.72	0.66	1.51	0.00	0.11
	c	3.6	1.6	4.6	0.2	0	0.2	0.78	7.71	0.64	0.31	0.00	0.02
	d	3.8	1.5	5	0.2	0	0.2	0.76	8.81	0.57	0.35	0.00	0.02
	e	3.6	1.6	4.5	0	0	0	0.80	7.77	0.45	0.00	0.00	0.00
	f	4	1.5	4.9	2.2	0	2.2	0.82	9.19	0.69	3.17	0.00	0.22
	g	3.3	1.5	5.1	1.2	3.1	4.3	0.65	8.52	0.55	2.17	0.36	0.47
	h	3.8	1.5	4.9	0.2	0	0.2	0.78	9.14	0.85	0.24	0.00	0.02
	l	3.8	1.6	4.8	0.7	0	0.7	0.79	8.76	0.72	0.97	0.00	0.07
	j	3.9	1.6	4.7	3.6	0	3.6	0.83	8.44	0.75	4.81	0.00	0.39
	Average	**3.76**	**1.55**	**4.78**	**1.04**	**0.31**	**1.35**	**0.79**	**8.54**	**0.64**	**1.57**	**0.04**	**0.15**
	Max	**4.00**	**1.60**	**5.10**	**3.60**	**3.10**	**4.30**	**0.85**	**9.19**	**0.85**	**4.81**	**0.36**	**0.47**
	Min	**3.30**	**1.50**	**4.50**	**0.00**	**0.00**	**0.00**	**0.65**	**7.71**	**0.45**	**0.00**	**0.00**	**0.00**

	Trial	Weld Depth from parent material (mm)	Weld Width at Half Max (mm)	Weld Top Width (mm)	Crack Length in HAZ (mm)	Crack Length in Weld (mm)	Total Crack Length (mm)	Depth/ Weld Top Width	Weld Area (mm^2)	HAZ Area (mm^2)	CI HAZ (/mm)	CI Weld (/mm)	CI Total (/mm)
Sample 7	a	2.3	3.2	5.3	0.4	0	0.4	0.43	6.98	0.41	0.99	0.00	0.05
	b	2.3	2.9	5.4	0.2	0	0.2	0.43	7.03	0.47	0.43	0.00	0.03
	c	2.4	2.8	5.6	0.3	0	0.3	0.43	6.97	0.44	0.68	0.00	0.04
	d	2.3	3	5.3	1.6	0	1.6	0.43	7.28	0.48	3.32	0.00	0.21
	e	2.3	3.1	5.6	0.4	0	0.4	0.41	7.35	0.56	0.72	0.00	0.05
	f	2.4	3	5.6	0.7	0	0.7	0.43	7.57	0.53	1.31	0.00	0.09
	g	2.2	2.6	5.5	0.4	0.2	0.6	0.40	7.57	0.58	0.68	0.03	0.07
	h	2.2	2.7	5.6	0.4	0	0.4	0.39	7.44	0.54	0.74	0.00	0.05
	l	2.4	3	5.7	1	0	1	0.42	6.52	0.59	1.70	0.00	0.14
	j	2.3	3	5.3	0.7	0	0.7	0.43	7.94	0.56	1.26	0.00	0.08
	Average	**2.31**	**2.93**	**5.49**	**0.61**	**0.02**	**0.63**	**0.42**	**7.27**	**0.52**	**1.18**	**0.00**	**0.08**
	Max	**2.40**	**3.20**	**5.70**	**1.60**	**0.20**	**1.60**	**0.43**	**7.94**	**0.59**	**3.32**	**0.03**	**0.21**
	Min	**2.20**	**2.60**	**5.30**	**0.20**	**0.00**	**0.20**	**0.39**	**6.52**	**0.41**	**0.43**	**0.00**	**0.03**

Sample 9	a	2.1	9	9	1.5	0	1.5	0.23	19.43	2.64	0.57	0.00	0.07
	b	2.4	9	9	0.6	0	0.6	0.27	19.18	2.16	0.28	0.00	0.03
	c	2.2	9	9	1.6	0	1.6	0.24	19.55	2.06	0.78	0.00	0.07
	d	2.3	9	9	0.8	0	0.8	0.26	19.59	3.11	0.26	0.00	0.04
	e	2.1	9	9	2	0	2	0.23	19.40	2.68	0.75	0.00	0.09
	f	2.5	9	9	1.2	0	1.2	0.28	19.99	2.76	0.43	0.00	0.05
	g	2.3	9	9	1.3	0	1.3	0.26	21.31	2.24	0.58	0.00	0.06
	h	2.2	9	9	4.6	0	4.6	0.24	20.40	1.86	2.48	0.00	0.21
	l	2.1	9	9	2.2	0	2.2	0.23	19.80	2.07	1.06	0.00	0.10
	j	2.1	9	9	4.5	0	4.5	0.23	19.47	2.47	1.82	0.00	0.21
	Average	**2.23**	**9.00**	**9.00**	**2.03**	**0.00**	**2.03**	**0.25**	**19.81**	**2.41**	**0.90**	**0.00**	**0.09**
	Max	**2.50**	**9.00**	**9.00**	**4.60**	**0.00**	**4.60**	**0.28**	**21.31**	**3.11**	**2.48**	**0.00**	**0.21**
	Min	**2.10**	**9.00**	**9.00**	**0.60**	**0.00**	**0.60**	**0.23**	**19.18**	**1.86**	**0.26**	**0.00**	**0.03**

	Trial	Weld Depth from parent material (mm)	Weld Width at Half Max (mm)	Weld Top Width (mm)	Crack Length in HAZ (mm)	Crack Length in Weld (mm)	Total Crack Length (mm)	Depth/ Weld Top Width	Weld Area (mm^2)	HAZ Area (mm^2)	CI HAZ (/mm)	CI Weld (/mm)	CI Total (/mm)
Sample 10	a	2.4	4.4	6.7	0.7	0	0.7	0.36	9.67	1.57	0.45	0.00	0.06
	b	2.4	3.9	6.8	0.4	0	0.4	0.35	9.81	2.74	0.15	0.00	0.03
	c	2.4	4	7.3	0	0	0	0.33	10.52	3.41	0.00	0.00	0.00
	d	2.4	4	7	0.3	0	0.3	0.34	10.14	2.45	0.12	0.00	0.02
	e	2.4	4.1	6.9	0	0	0	0.35	10.31	1.96	0.00	0.00	0.00
	f	2.4	4.3	6.9	0.2	0	0.2	0.35	10.23	2.52	0.08	0.00	0.02
	g	2.2	4.9	7.9	0	0	0	0.28	10.15	3.85	0.00	0.00	0.00
	h	2.3	4.9	7.5	0	0	0	0.31	10.32	3.72	0.00	0.00	0.00
	I	2.1	4.6	8	0	0	0	0.26	10.10	2.79	0.00	0.00	0.00
	j	2.4	4.2	6.8	0.7	0	0.7	0.35	10.32	2.02	0.35	0.00	0.06
	Average	**2.34**	**4.33**	**7.18**	**0.23**	**0.00**	**0.23**	**0.33**	**10.16**	**2.70**	**0.11**	**0.00**	**0.02**
	Max	**2.40**	**4.90**	**8.00**	**0.70**	**0.00**	**0.70**	**0.36**	**10.52**	**3.85**	**0.45**	**0.00**	**0.06**
	Min	**2.10**	**3.90**	**6.70**	**0.00**	**0.00**	**0.00**	**0.26**	**9.67**	**1.57**	**0.00**	**0.00**	**0.00**
Sample 11	a	9.7	1.6	7.2	4.4	2.8	7.2	1.35	24.41	4.90	0.90	0.11	0.25
	b	9.6	1.8	7.5	3.8	2.3	6.1	1.28	-	-	-	-	-
	c	9.6	1.7	7.2	3.8	2.8	6.6	1.33	23.60	5.46	0.70	0.12	0.23
	d	9.5	1.7	7.4	4.9	0	4.9	1.28	-	-	-	-	-
	e	9.7	1.9	7	6.6	1.1	7.7	1.39	23.01	5.95	1.11	0.05	0.27
	f	9.6	1.7	7.6	7.7	2	9.7	1.26	23.67	4.82	1.60	0.08	0.34
	g	9.7	1.7	7.4	7.7	0.9	8.6	1.31	23.51	5.33	1.45	0.04	0.30
	h	9.7	1.9	7.2	9.5	3	12.5	1.35	22.73	4.72	2.01	0.13	0.46
	I	9.1	1.6	7	6.6	5.2	11.8	1.30	21.94	5.21	1.27	0.24	0.43
	j	9.4	1.9	7.4	5.7	2.3	8	1.27	24.01	5.18	1.10	0.10	0.27
	Average	**9.56**	**1.75**	**7.29**	**6.07**	**2.24**	**8.31**	**1.31**	**23.36**	**5.20**	**1.27**	**0.11**	**0.32**
	Max	**9.70**	**1.90**	**7.60**	**9.50**	**5.20**	**12.50**	**1.39**	**24.41**	**5.95**	**2.01**	**0.24**	**0.46**
	Min	**9.10**	**1.60**	**7.00**	**3.80**	**0.00**	**4.90**	**1.26**	**21.94**	**4.72**	**0.70**	**0.04**	**0.23**

	Trial	Weld Depth from parent material (mm)	Weld Width at Half Max (mm)	Weld Top Width (mm)	Crack Length in HAZ (mm)	Crack Length in Weld (mm)	Total Crack Length (mm)	Depth/ Weld Top Width	Weld Area (mm^2)	HAZ Area (mm^2)	CI HAZ (/mm)	CI Weld (/mm)	CI Total (/mm)
Sample 12	a	7.4	1.4	5.4	2.7	2.2	4.9	1.37	14.37	2.65	1.02	0.15	0.29
	b	7.9	1.4	5.2	2.7	3	5.7	1.52	14.16	1.87	1.44	0.21	0.36
	c	8.1	1.4	4.8	2.9	2.8	5.7	1.69	13.65	1.93	1.50	0.21	0.37
	d	8.3	1.4	4.8	1.7	3.2	4.9	1.73	13.56	2.18	0.78	0.24	0.31
	e	8	1.3	4.6	2.3	0.1	2.4	1.74	12.38	2.51	0.92	0.01	0.16
	f	8.4	1.3	4.5	1.7	1.7	3.4	1.87	12.95	2.15	0.79	0.13	0.23
	g	8.5	1.4	4.7	1.4	1.4	2.8	1.81	13.76	1.74	0.80	0.10	0.18
	h	8.1	1.3	5.4	2.4	1	3.4	1.50	14.41	2.49	0.96	0.07	0.20
	I	8.4	1.3	4.9	2.4	1.5	3.9	1.71	13.26	2.08	1.15	0.11	0.25
	j	7.9	1.4	4.6	3.6	0.1	3.7	1.72	12.98	1.57	2.30	0.01	0.25
	Average	**8.10**	**1.36**	**4.89**	**2.38**	**1.70**	**4.08**	**1.67**	**13.55**	**2.12**	**1.17**	**0.12**	**0.26**
	Max	**8.50**	**1.40**	**5.40**	**3.60**	**3.20**	**5.70**	**1.87**	**14.41**	**2.65**	**2.30**	**0.24**	**0.37**
	Min	**7.40**	**1.30**	**4.50**	**1.40**	**0.10**	**2.40**	**1.37**	**12.38**	**1.57**	**0.78**	**0.01**	**0.16**

Sample 13	a	6	0.9	3	1	0.7	1.7	2.00	6.99	0.99	1.01	0.10	0.21
	b	6	0.9	3.2	0.8	1.2	2	1.88	6.69	0.68	1.17	0.18	0.27
	c	6.3	0.9	3	1.2	0.5	1.7	2.10	6.90	0.71	1.69	0.07	0.22
	d	5.8	0.9	3.4	0.7	0.1	0.8	1.71	6.82	0.79	0.89	0.01	0.11
	e	6.1	0.9	3.1	1	0.5	1.5	1.97	6.81	0.69	1.45	0.07	0.20
	f	6.2	0.9	3.1	0.6	0	0.6	2.00	7.14	0.73	0.82	0.00	0.08
	g	6.3	0.9	3	1.6	0.9	2.5	2.10	7.04	0.78	2.05	0.13	0.32
	h	6.1	0.9	3	0.7	0	0.7	2.03	7.15	0.74	0.94	0.00	0.09
	I	6.3	0.9	3.2	1.1	1.2	2.3	1.97	7.29	0.74	1.48	0.16	0.29
	j	6.3	0.8	2.8	0.7	0	0.7	2.25	6.92	0.64	1.10	0.00	0.09
	Average	**6.14**	**0.89**	**3.08**	**0.94**	**0.51**	**1.45**	**2.00**	**6.98**	**0.75**	**1.26**	**0.07**	**0.19**
	Max	**6.30**	**0.90**	**3.40**	**1.60**	**1.20**	**2.50**	**2.25**	**7.29**	**0.99**	**2.05**	**0.18**	**0.32**
	Min	**5.80**	**0.80**	**2.80**	**0.60**	**0.00**	**0.60**	**1.71**	**6.69**	**0.64**	**0.82**	**0.00**	**0.08**

A.2 Rene 80

Table A-2 Rene 80 Raw Data

	Trial	Weld Depth from parent material (mm)	Weld Width at Half Max (mm)	Weld Top Width (mm)	Crack Length in HAZ (mm)	Crack Length in Weld (mm)	Total Crack Length (mm)	Depth/ Weld Top Width	Weld Area (mm^2)	HAZ Area (mm^2)	CI HAZ (/mm)	CI Weld (/mm)	CI Total (/mm)
Sample 2	a	2.4	3.0	5.1	0	0	0	0.47	7.37	0.70	0.00	0.00	0.00
	b	2.2	3.3	5.5	0	0	0	0.40	7.69	0.69	0.00	0.00	0.00
	c	2.4	3.1	5.1	0	0	0	0.47	7.32	0.85	0.00	0.00	0.00
	d	2.4	3.1	5.1	0	0	0	0.47	7.31	0.73	0.00	0.00	0.00
	e	2.3	3.2	5.7	0.3	0	0.3	0.40	8.31	0.69	0.44	0.00	0.03
	f	2.4	3.1	5.2	0	0	0	0.46	7.42	0.77	0.00	0.00	0.00
	g	2.3	3.2	5.3	0.1	0	0.1	0.43	7.46	0.51	0.20	0.00	0.01
	h	2.3	3.3	5.2	0.1	0	0.1	0.44	7.40	0.85	0.12	0.00	0.01
	I	2.2	3.1	5.5	0	0	0	0.40	7.55	0.80	0.00	0.00	0.00
	j	2.3	3.3	5.2	0.2	0	0.2	0.44	7.41	0.62	0.32	0.00	0.02
	Average	**2.32**	**3.17**	**5.29**	**0.07**	**0.00**	**0.07**	**0.44**	**7.52**	**0.72**	**0.11**	**0.00**	**0.01**
	Max	**2.40**	**3.30**	**5.70**	**0.30**	**0.00**	**0.30**	**0.47**	**8.31**	**0.85**	**0.44**	**0.00**	**0.03**
	Min	**2.20**	**3.00**	**5.10**	**0.00**	**0.00**	**0.00**	**0.40**	**7.31**	**0.51**	**0.00**	**0.00**	**0.00**

	Trial	Weld Depth from parent material (mm)	Weld Width at Half Max (mm)	Weld Top Width (mm)	Crack Length in HAZ (mm)	Crack Length in Weld (mm)	Total Crack Length (mm)	Depth/ Weld Top Width	Weld Area (mm^2)	HAZ Area (mm^2)	Cl HAZ (/mm)	Cl Weld (/mm)	Cl Total (/mm)
Sample 3	a	3.6	1.8	4.7	1.3	0.2	1.5	0.77	8.24	0.81	1.60	0.02	0.17
	b	3.6	1.8	4.7	0.1	0	0.1	0.77	8.23	0.87	0.11	0.00	0.01
	c	3.2	1.8	5.2	0.1	0	0.1	0.62	8.96	0.75	0.13	0.00	0.01
	d	3.4	1.8	4.7	0.6	0	0.6	0.72	8.23	0.96	0.63	0.00	0.07
	e	3.6	1.8	4.7	1.5	1.6	3.1	0.77	8.35	0.45	3.34	0.19	0.35
	f	3.4	1.8	5.0	0.2	0	0.2	0.68	8.30	1.07	0.19	0.00	0.02
	g	3.5	1.9	4.8	0.5	0	0.5	0.73	8.41	0.72	0.70	0.00	0.05
	h	3.2	1.8	5.0	0	0	0	0.64	8.39	1.11	0.00	0.00	0.00
	l	3.5	1.9	4.6	0.7	0.7	1.4	0.76	8.21	0.85	0.82	0.09	0.15
	j	3.2	1.8	5.4	0	0	0	0.59	9.48	0.99	0.00	0.00	0.00
	Average	**3.42**	**1.82**	**4.88**	**0.50**	**0.25**	**0.75**	**0.70**	**8.48**	**0.86**	**0.75**	**0.03**	**0.08**
	Max	**3.60**	**1.90**	**5.40**	**1.50**	**1.60**	**3.10**	**0.77**	**9.48**	**1.11**	**3.34**	**0.19**	**0.35**
	Min	**3.20**	**1.80**	**4.60**	**0.00**	**0.00**	**0.00**	**0.59**	**8.21**	**0.45**	**0.00**	**0.00**	**0.00**

	Trial	Weld Depth from parent material (mm)	Weld Width at Half Max (mm)	Weld Top Width (mm)	Crack Length in HAZ (mm)	Crack Length in Weld (mm)	Total Crack Length (mm)	Depth/ Weld Top Width	Weld Area (mm^2)	HAZ Area (mm^2)	Cl HAZ (/mm)	Cl Weld (/mm)	Cl Total (/mm)
Sample 4	a	4.9	1.3	3.5	0.8	0	0.8	1.40	8.47	0.65	1.23	0.00	0.09
	b	4.6	1.3	3.7	0.4	0	0.4	1.24	8.37	0.71	0.57	0.00	0.04
	c	5.1	1.3	3.6	1.1	0	1.1	1.42	8.67	1.22	0.90	0.00	0.11
	d	4.6	1.4	3.6	0.7	0.3	1	1.28	8.36	0.94	0.74	0.04	0.11
	e	4.6	1.3	3.8	0.6	0	0.6	1.21	8.82	0.87	0.69	0.00	0.06
	f	4.8	1.3	3.7	0.2	0	0.2	1.30	8.73	0.73	0.27	0.00	0.02
	g	4.9	1.3	3.8	0.9	0	0.9	1.29	9.04	0.65	1.37	0.00	0.09
	h	4.9	1.3	3.6	0.9	0	0.9	1.36	8.46	0.51	1.76	0.00	0.10
	Average	**4.80**	**1.31**	**3.66**	**0.70**	**0.04**	**0.74**	**1.31**	**8.62**	**0.79**	**0.94**	**0.00**	**0.08**
	Max	**5.10**	**1.40**	**3.80**	**1.10**	**0.30**	**1.10**	**1.42**	**9.04**	**1.22**	**1.76**	**0.04**	**0.11**
	Min	**4.60**	**1.30**	**3.50**	**0.20**	**0.00**	**0.20**	**1.21**	**8.36**	**0.51**	**0.27**	**0.00**	**0.02**

	Trial	Weld Depth from parent material (mm)	Weld Width at Half Max (mm)	Weld Top Width (mm)	Crack Length in HAZ (mm)	Crack Length in Weld (mm)	Total Crack Length (mm)	Depth/ Weld Top Width	Weld Area (mm^2)	HAZ Area (mm^2)	CI HAZ (/mm)	CI Weld (/mm)	CI Total (/mm)
Sample 5	a	5.6	1.0	3.8	2.2	0	2.2	1.47	8.78	1.40	1.57	0.00	0.22
	b	6.1	1.0	3.9	0.5	0	0.5	1.56	8.20	0.94	0.53	0.00	0.05
	c	5.5	1.0	3.9	0.4	0	0.4	1.41	8.34	0.80	0.50	0.00	0.04
	d	5.6	1.0	4.0	0.6	0	0.6	1.40	8.37	0.76	0.79	0.00	0.07
	e	5.2	1.0	4.1	1.7	0	1.7	1.27	8.39	0.71	2.41	0.00	0.19
	f	5.5	1.0	3.8	0	1.8	1.8	1.45	8.28	0.52	0.00	0.22	0.20
	g	5.4	1.0	3.9	1	0	1	1.38	8.86	0.83	1.21	0.00	0.10
	h	5.7	1.1	3.8	1.3	0	1.3	1.50	8.29	0.96	1.35	0.00	0.14
	l	5.5	1.0	3.8	0.8	0	0.8	1.45	8.36	0.74	1.09	0.00	0.09
	j	5.7	1.0	3.9	0.6	0	0.6	1.46	8.30	0.74	0.81	0.00	0.07
	Average	**5.58**	**1.01**	**3.89**	**0.91**	**0.18**	**1.09**	**1.44**	**8.42**	**0.84**	**1.03**	**0.02**	**0.12**
	Max	**6.10**	**1.10**	**4.10**	**2.20**	**1.80**	**2.20**	**1.56**	**8.86**	**1.40**	**2.41**	**0.22**	**0.22**
	Min	**5.20**	**1.00**	**3.80**	**0.00**	**0.00**	**0.40**	**1.27**	**8.20**	**0.52**	**0.00**	**0.00**	**0.04**

Sample 6	a	3.6	1.5	4.6	0.7	0	0.7	0.78	8.42	0.55	1.28	0.00	0.08
	b	3.5	1.5	5.0	0.7	0	0.7	0.70	7.90	0.60	1.16	0.00	0.08
	c	3.6	1.6	4.6	1	0	1	0.78	8.28	0.74	1.35	0.00	0.11
	d	3.5	1.7	4.6	0.8	0	0.8	0.76	7.99	0.72	1.11	0.00	0.09
	e	3.6	1.5	5.2	1.7	0	1.7	0.69	9.45	0.79	2.15	0.00	0.17
	f	3.6	1.5	4.7	1.2	0	1.2	0.77	8.22	0.60	2.01	0.00	0.14
	g	3.7	1.6	4.9	0.4	0	0.4	0.76	8.58	0.89	0.45	0.00	0.04
	h	3.5	1.5	5.0	1	0	1	0.70	8.59	0.69	1.44	0.00	0.11
	l	3.6	1.6	4.7	0.9	0	0.9	0.77	8.16	0.71	1.27	0.00	0.10
	j	3.6	1.6	4.8	1.2	0	1.2	0.75	8.31	0.69	1.75	0.00	0.13
	Average	**3.58**	**1.56**	**4.81**	**0.96**	**0.00**	**0.96**	**0.75**	**8.39**	**0.70**	**1.40**	**0.00**	**0.11**
	Max	**3.70**	**1.70**	**5.20**	**1.70**	**0.00**	**1.70**	**0.78**	**9.45**	**0.89**	**2.15**	**0.00**	**0.17**
	Min	**3.50**	**1.50**	**4.60**	**0.40**	**0.00**	**0.40**	**0.69**	**7.90**	**0.55**	**0.45**	**0.00**	**0.04**

	Trial	Weld Depth from parent material (mm)	Weld Width at Half Max (mm)	Weld Top Width (mm)	Crack Length in HAZ (mm)	Crack Length in Weld (mm)	Total Crack Length (mm)	Depth/ Weld Top Width	Weld Area (mm^2)	HAZ Area (mm^2)	CI HAZ (/mm)	CI Weld (/mm)	CI Total (/mm)
Sample 7	a	1.9	3.0	4.5	0.2	0	0.2	0.42	6.79	0.39	0.52	0.00	0.03
	b	2.3	2.9	5.5	0.1	0	0.1	0.42	7.56	0.61	0.16	0.00	0.01
	c	2.1	2.9	5.6	0	0	0	0.38	7.47	0.38	0.00	0.00	0.00
	d	2.1	2.8	5.6	0	0	0	0.38	7.55	0.41	0.00	0.00	0.00
	e	2.3	3.0	5.2	0	0	0	0.44	7.19	0.40	0.00	0.00	0.00
	f	2.2	3.1	5.4	0.2	0	0.2	0.41	7.27	0.35	0.57	0.00	0.03
	g	2.2	3.3	5.4	0.1	0	0.1	0.41	7.33	0.56	0.18	0.00	0.01
	h	2.3	2.9	5.5	0.1	0	0.1	0.42	7.60	0.63	0.16	0.00	0.01
	I	2.3	3.1	5.3	0.1	0	0.1	0.43	7.22	0.47	0.21	0.00	0.01
	j	2.2	3.4	5.2	0	0	0	0.42	7.33	0.65	0.00	0.00	0.00
	Average	**2.19**	**3.04**	**5.32**	**0.08**	**0.00**	**0.08**	**0.41**	**7.33**	**0.48**	**0.18**	**0.00**	**0.01**
	Max	**2.30**	**3.40**	**5.60**	**0.20**	**0.00**	**0.20**	**0.44**	**7.60**	**0.65**	**0.57**	**0.00**	**0.03**
	Min	**1.90**	**2.80**	**4.50**	**0.00**	**0.00**	**0.00**	**0.38**	**6.79**	**0.35**	**0.00**	**0.00**	**0.00**
Sample 9	a	2.5	9.8	9.0	0.6	0	0.6	0.28	18.20	4.35	0.14	0.00	0.03
	b	2.7	9.8	9.0	0.7	0	0.7	0.30	17.39	4.72	0.15	0.00	0.03
	c	2.6	9.8	9.0	0.8	0	0.8	0.29	17.63	4.45	0.18	0.00	0.04
	d	2.5	9.8	9.0	0	0	0	0.28	18.01	3.83	0.00	0.00	0.00
	e	2.5	9.8	9.0	0.2	0	0.2	0.28	18.21	4.29	0.05	0.00	0.01
	f	2.5	9.8	9.0	0.4	0	0.4	0.28	18.31	5.32	0.08	0.00	0.02
	g	2.6	9.8	9.0	0	0	0	0.29	18.54	4.72	0.00	0.00	0.00
	h	2.5	9.8	9.0	1	0	1	0.28	18.35	4.81	0.21	0.00	0.04
	I	2.5	9.8	9.0	1.1	0	1.1	0.28	18.31	4.59	0.24	0.00	0.05
	j	2.4	9.8	9.0	0.5	0	0.5	0.27	17.71	3.96	0.13	0.00	0.02
	Average	**2.53**	**9.80**	**9.00**	**0.53**	**0.00**	**0.53**	**0.28**	**18.06**	**4.50**	**0.12**	**0.00**	**0.02**
	Max	**2.70**	**9.80**	**9.00**	**1.10**	**0.00**	**1.10**	**0.30**	**18.54**	**5.32**	**0.24**	**0.00**	**0.05**
	Min	**2.40**	**9.80**	**9.00**	**0.00**	**0.00**	**0.00**	**0.27**	**17.39**	**3.83**	**0.00**	**0.00**	**0.00**

	Trial	Weld Depth from parent material (mm)	Weld Width at Half Max (mm)	Weld Top Width (mm)	Crack Length in HAZ (mm)	Crack Length in Weld (mm)	Total Crack Length (mm)	Depth/ Weld Top Width	Weld Area (mm^2)	HAZ Area (mm^2)	CI HAZ (/mm)	CI Weld (/mm)	CI Total (/mm)
Sample 10	a	1.6	5.8	7.2	0.1	0	0.1	0.22	10.42	5.71	0.02	0.00	0.01
	b	1.8	6.4	7.1	0	0	0	0.25	10.23	5.53	0.00	0.00	0.00
	c	1.8	6.5	7.0	1.6	0	1.6	0.26	10.18	5.76	0.28	0.00	0.10
	d	1.9	6.1	7.1	0.7	0	0.7	0.27	10.47	5.29	0.13	0.00	0.04
	e	1.8	6.2	7.1	0	0	0	0.25	10.49	5.86	0.00	0.00	0.00
	f	1.5	7.0	7.3	0	0	0	0.21	9.73	2.46	0.00	0.00	0.00
	g	1.4	6.7	7.2	0	0	0	0.19	9.46	1.73	0.00	0.00	0.00
	h	1.8	6.0	7.0	0.6	0	0.6	0.26	10.45	5.52	0.11	0.00	0.04
	I	1.9	5.9	7.0	0	0	0	0.27	10.46	5.94	0.00	0.00	0.00
	j	1.7	6.6	7.4	0	0	0	0.23	10.49	5.34	0.00	0.00	0.00
	Average	**1.72**	**6.32**	**7.14**	**0.30**	**0.00**	**0.30**	**0.24**	**10.24**	**4.91**	**0.05**	**0.00**	**0.02**
	Max	**1.90**	**7.00**	**7.40**	**1.60**	**0.00**	**1.60**	**0.27**	**10.49**	**5.94**	**0.28**	**0.00**	**0.10**
	Min	**1.40**	**5.80**	**7.00**	**0.00**	**0.00**	**0.00**	**0.19**	**9.46**	**1.73**	**0.00**	**0.00**	**0.00**
Sample 11	a	9.7	1.7	7.0	6	2.1	8.1	1.39	21.60	5.40	1.11	0.10	0.30
	b	10.0	1.6	7.0	4.7	4.2	8.9	1.43	22.29	6.20	0.76	0.19	0.31
	c	9.1	1.8	7.1	7.4	1.7	9.1	1.28	22.32	6.30	1.17	0.08	0.32
	d	8.1	1.8	7.5	2.5	3.7	6.2	1.08	22.28	4.61	0.54	0.17	0.23
	e	8.8	1.8	7.6	5.7	1.4	7.1	1.16	22.33	5.78	0.99	0.06	0.25
	f	9.2	1.9	7.1	3.8	1.7	5.5	1.30	23.43	5.72	0.66	0.07	0.19
	g	9.8	1.7	7.0	7.8	2.3	10.1	1.40	22.93	6.56	1.19	0.10	0.34
	h	9.9	1.7	7.2	5.1	1.5	6.6	1.38	23.11	6.10	0.84	0.06	0.23
	I	10.2	1.6	7.1	5.2	1.9	7.1	1.44	22.32	7.44	0.70	0.09	0.24
	j	10.1	1.8	7.2	4.8	2	6.8	1.40	23.27	4.97	0.97	0.09	0.24
	Average	**9.49**	**1.74**	**7.18**	**5.30**	**2.25**	**7.55**	**1.32**	**22.58**	**5.91**	**0.89**	**0.10**	**0.27**
	Max	**10.20**	**1.90**	**7.60**	**7.80**	**4.20**	**10.10**	**1.44**	**23.43**	**7.44**	**1.19**	**0.19**	**0.34**
	Min	**8.10**	**1.60**	**7.00**	**2.50**	**1.40**	**5.50**	**1.08**	**21.60**	**4.61**	**0.54**	**0.06**	**0.19**

	Trial	Weld Depth from parent material (mm)	Weld Width at Half Max (mm)	Weld Top Width (mm)	Crack Length in HAZ (mm)	Crack Length in Weld (mm)	Total Crack Length (mm)	Depth/ Weld Top Width	Weld Area (mm^2)	HAZ Area (mm^2)	CI HAZ (/mm)	CI Weld (/mm)	CI Total (/mm)
Sample 12	a	7.6	1.4	4.7	0.7	1.8	2.5	1.62	13.01	1.82	0.38	0.14	0.17
	b	7.8	1.3	4.6	0.9	0.3	1.2	1.70	12.86	1.79	0.50	0.02	0.08
	c	8.7	1.3	4.7	1	1	2	1.85	-	-	-	-	-
	d	7.0	1.3	5.4	0.4	0	0.4	1.30	-	-	-	-	-
	e	8.4	1.3	5.0	1.8	0	1.8	1.68	13.54	2.78	0.65	0.00	0.11
	f	7.7	1.3	4.8	0.8	0.2	1	1.60	12.57	2.73	0.29	0.02	0.07
	g	7.6	1.3	4.8	0.2	0	0.2	1.58	12.96	1.20	0.17	0.00	0.01
	h	7.6	1.3	5.3	0.2	0.1	0.3	1.43	13.62	1.94	0.10	0.01	0.02
	l	8.4	1.4	5.0	0.8	0	0.8	1.68	13.76	2.07	0.39	0.00	0.05
	j	7.6	1.3	4.7	1.6	0	1.6	1.62	12.71	2.07	0.77	0.00	0.11
	Average	**7.84**	**1.32**	**4.90**	**0.84**	**0.34**	**1.18**	**1.61**	**13.13**	**2.05**	**0.41**	**0.02**	**0.08**
	Max	**8.70**	**1.40**	**5.40**	**1.80**	**1.80**	**2.50**	**1.85**	**13.76**	**2.78**	**0.77**	**0.14**	**0.17**
	Min	**7.00**	**1.30**	**4.60**	**0.20**	**0.00**	**0.20**	**1.30**	**12.57**	**1.20**	**0.10**	**0.00**	**0.01**
Sample 13	a	6.8	0.9	3.2	0.2	0	0.2	2.13	7.33	1.64	0.12	0.00	0.02
	b	5.8	1.0	3.3	0.1	0	0.1	1.76	7.42	1.23	0.08	0.00	0.01
	c	5.9	0.9	3.2	0	0	0	1.84	7.13	1.13	0.00	0.00	0.00
	d	6.6	1.0	3.1	0	0	0	2.13	7.47	1.47	0.00	0.00	0.00
	e	6.3	0.9	3.2	0.2	0	0.2	1.97	7.51	1.21	0.17	0.00	0.02
	f	6.1	0.9	3.1	0.1	0	0.1	1.97	7.24	1.26	0.08	0.00	0.01
	g	6.3	0.9	3.2	0.8	0	0.8	1.97	7.00	1.81	0.44	0.00	0.09
	h	6.4	1.0	3.2	0.1	0	0.1	2.00	7.74	1.39	0.07	0.00	0.01
	l	6.3	0.9	3.2	0.1	0	0.1	1.97	7.55	1.61	0.06	0.00	0.01
	j	6.0	1.0	3.1	0.8	1.2	2	1.94	7.22	1.79	0.45	0.17	0.22
	Average	**6.25**	**0.94**	**3.18**	**0.24**	**0.12**	**0.36**	**1.97**	**7.36**	**1.45**	**0.15**	**0.02**	**0.04**
	Max	**6.80**	**1.00**	**3.30**	**0.80**	**1.20**	**2.00**	**2.13**	**7.74**	**1.81**	**0.45**	**0.17**	**0.22**
	Min	**5.80**	**0.90**	**3.10**	**0.00**	**0.00**	**0.00**	**1.76**	**7.00**	**1.13**	**0.00**	**0.00**	**0.00**

A.3 Single Crystal

Table A-3 SX Raw Data

	Trial	Weld Depth from parent material (mm)	Weld Width at Half Max (mm)	Weld Top Width (mm)	Crack Length in HAZ (mm)	Crack Length in Weld (mm)	Total Crack Length (mm)	Depth/ Top Width	Depth/ Mid Width	Weld Area (mm^2)	CI Weld (/mm)
Sample 2	a	2.2	3.1	5.5	0	0	0	0.40	0.71	7.20	0.00
	b	2.3	3.3	5.2	0	0	0	0.44	0.70	7.01	0.00
	c	1.9	2.6	5.8	0	0	0	0.33	0.73	7.83	0.00
	d	2.5	3.1	5.1	0	0	0	0.49	0.81	7.13	0.00
	e	2.4	3.3	5.2	0	2.2	2.2	0.46	0.73	7.01	0.31
	f	2.1	3.3	5.5	0	1.2	1.2	0.38	0.64	6.96	0.17
	g	2.4	3.1	5	0	0.4	0.4	0.48	0.77	7.29	0.05
	h	2.4	3	5	0	0	0	0.48	0.80	7.04	0.00
	I	1.8	2.2	6.4	0	2	2	0.28	0.82	8.18	0.24
	j	2.3	3	5.2	0	0.3	0.3	0.44	0.77	7.20	0.04
	Average	**2.23**	**3**	**5.39**	**0**	**0.61**	**0.61**	**0.42**	**0.75**	**7.29**	**0.08**
	Max	**2.5**	**3.3**	**6.4**	**0**	**2.2**	**2.2**	**0.49**	**0.82**	**8.18**	**0.31**
	Min	**1.8**	**2.2**	**5**	**0**	**0**	**0**	**0.28**	**0.64**	**6.96**	**0.00**

	Trial	Weld Depth from parent material (mm)	Weld Width at Half Max (mm)	Weld Top Width (mm)	Crack Length in HAZ (mm)	Crack Length in Weld (mm)	Total Crack Length (mm)	Depth/ Top Width	Depth/ Mid Width	Weld Area (mm^2)	CI Weld (/mm)
Sample 3	a	3.4	2	4.5	0	4.7	4.7	0.76	1.70	7.84	0.60
	b	3.4	1.9	5	0	4.9	4.9	0.68	1.79	7.72	0.64
	c	3.5	2	4.7	0	7.9	7.9	0.74	1.75	7.75	1.02
	d	3.6	2	4.6	0	3.8	3.8	0.78	1.80	-	-
	e	3	1.8	5.4	0	5.2	5.2	0.56	1.67	-	-
	f	3.5	2	4.5	0	9.2	9.2	0.78	1.75	7.91	1.16
	g	3.5	2	4.6	0	5.8	5.8	0.76	1.75	7.67	0.76
	h	3.2	1.9	4.9	0	5.2	5.2	0.65	1.68	7.66	0.68
	I	3.5	2	4.6	0	4.9	4.9	0.76	1.75	9.13	0.54
	j	3	1.8	5.8	0	4.7	4.7	0.52	1.67	7.81	0.60
	Average	**3.36**	**1.94**	**4.86**	**0**	**5.63**	**5.63**	**0.69**	**1.73**	**7.94**	**0.75**
	Max	**3.6**	**2**	**5.8**	**0**	**9.2**	**9.2**	**0.78**	**1.80**	**9.13**	**1.16**
	Min	**3**	**1.8**	**4.5**	**0**	**3.8**	**3.8**	**0.52**	**1.67**	**7.66**	**0.54**

Sample 4	a	4.8	1.4	3.5	0	5.3	5.3	1.37	3.43	8.11	0.65
	b	4.1	1.5	4.1	0	5.2	5.2	1.00	2.73	7.98	0.65
	c	5.1	1.4	3.3	0	3.7	3.7	1.55	3.64	8.30	0.45
	d	4.8	1.3	3.4	0	4.1	4.1	1.41	3.69	7.82	0.52
	e	4.4	1.3	3.8	0	4.5	4.5	1.16	3.38	8.06	0.56
	f	5.1	1.3	3.2	0	6.4	6.4	1.59	3.92	7.79	0.82
	g	4.8	1.3	3.1	0	1.3	1.3	1.55	3.69	8.12	0.16
	h	4.5	1.3	3.7	0	4	4	1.22	3.46	7.82	0.51
	I	5	1.3	3.1	0	2.9	2.9	1.61	3.85	8.15	0.36
	j	4.6	1.4	3.6	0	5.6	5.6	1.28	3.29	8.07	0.69
	Average	**4.72**	**1.35**	**3.48**	**0**	**4.3**	**4.3**	**1.36**	**3.50**	**8.02**	**0.54**
	Max	**5.1**	**1.5**	**4.1**	**0**	**6.4**	**6.4**	**1.61**	**3.92**	**8.30**	**0.82**
	Min	**4.1**	**1.3**	**3.1**	**0**	**1.3**	**1.3**	**1.00**	**2.73**	**7.79**	**0.16**

	Trial	Weld Depth from parent material (mm)	Weld Width at Half Max (mm)	Weld Top Width (mm)	Crack Length in HAZ (mm)	Crack Length in Weld (mm)	Total Crack Length (mm)	Depth/ Top Width	Depth/ Mid Width	Weld Area (mm^2)	CI Weld (/mm)
Sample 5	a	5.9	1	3.6	0	4.6	4.6	1.64	5.90	7.62	0.60
	b	6	1.1	3.6	0	3.8	3.8	1.67	5.45	8.08	0.47
	c	5.9	1	3.6	0	14.5	14.5	1.64	5.90	7.85	1.85
	d	6.1	1	3.5	0	3.4	3.4	1.74	6.10	7.80	0.44
	e	5.2	0.9	4	0	2.8	2.8	1.30	5.78	7.40	0.38
	f	5.8	1	3.7	0	5.3	5.3	1.57	5.80	7.62	0.70
	g	5.7	1	3.9	0	5.2	5.2	1.46	5.70	7.76	0.67
	h	5.6	1	3.8	0	3.7	3.7	1.47	5.60	7.76	0.48
	l	6.2	1	3.6	0	4.5	4.5	1.72	6.20	7.63	0.59
	j	5.7	0.9	3.5	0	6.4	6.4	1.63	6.33	8.49	0.75
	Average	**5.81**	**0.99**	**3.68**	**0**	**5.42**	**5.42**	**1.58**	**5.87**	**7.80**	**0.69**
	Max	**6.2**	**1.1**	**4**	**0**	**14.5**	**14.5**	**1.74**	**6.33**	**8.49**	**1.85**
	Min	**5.2**	**0.9**	**3.5**	**0**	**2.8**	**2.8**	**1.30**	**5.45**	**7.40**	**0.38**

Sample 6	a	3.6	1.8	4.4	0	7.7	7.7	0.82	2.00	7.65	1.01
	b	3.7	1.5	4.8	0	2.8	2.8	0.77	2.47	8.01	0.35
	c	3.7	1.6	4.4	0	8.4	8.4	0.84	2.31	7.61	1.10
	d	3.9	1.6	4.6	0	8.4	8.4	0.85	2.44	8.17	1.03
	e	3.6	1.5	4.9	0	13.7	13.7	0.73	2.40	7.95	1.72
	f	3.8	1.6	4.5	0	8.6	8.6	0.84	2.38	7.69	1.12
	g	3.6	1.6	4.4	0	4.9	4.9	0.82	2.25	7.57	0.65
	h	3.7	1.5	4.8	0	12.6	12.6	0.77	2.47	7.94	1.59
	l	3.8	1.5	4.8	0	4.4	4.4	0.79	2.53	8.91	0.49
	j	3.5	1.6	5.3	0	11.9	11.9	0.66	2.19	8.26	1.44
	Average	**3.69**	**1.58**	**4.69**	**0**	**8.34**	**8.34**	**0.79**	**2.34**	**7.98**	**1.05**
	Max	**3.9**	**1.8**	**5.3**	**0**	**13.7**	**13.7**	**0.85**	**2.53**	**8.91**	**1.72**
	Min	**3.5**	**1.5**	**4.4**	**0**	**2.8**	**2.8**	**0.66**	**2.00**	**7.57**	**0.35**

	Trial	Weld Depth from parent material (mm)	Weld Width at Half Max (mm)	Weld Top Width (mm)	Crack Length in HAZ (mm)	Crack Length in Weld (mm)	Total Crack Length (mm)	Depth/ Top Width	Depth/ Mid Width	Weld Area (mm^2)	Cl Weld (/mm)
Sample 7	a	2.2	3	5.5	0	0.8	0.8	0.40	0.73	7.15	0.11
	b	2.3	3.2	5.2	0	0	0	0.44	0.72	6.46	0.00
	c	2.3	3.1	5.1	0	1.7	1.7	0.45	0.74	6.75	0.25
	d	2	3	5.7	0	3	3	0.35	0.67	6.72	0.45
	e	2.2	3.2	5.3	0	1.4	1.4	0.42	0.69	7.30	0.19
	f	2.3	3.3	5.2	0	0	0	0.44	0.70	6.63	0.00
	g	2.2	3.1	5.4	0	0.9	0.9	0.41	0.71	7.16	0.13
	h	1.9	2.8	5.8	0	4.4	4.4	0.33	0.68	6.68	0.66
	l	2.3	3.2	5.1	0	0	0	0.45	0.72	7.50	0.00
	j	2.3	3	5.1	0	0	0	0.45	0.77	6.79	0.00
	Average	**2.2**	**3.09**	**5.34**	**0**	**1.22**	**1.22**	**0.41**	**0.71**	**6.91**	**0.18**
	Max	**2.3**	**3.3**	**5.8**	**0**	**4.4**	**4.4**	**0.45**	**0.77**	**7.50**	**0.66**
	Min	**1.9**	**2.8**	**5.1**	**0**	**0**	**0**	**0.33**	**0.67**	**6.46**	**0.00**
Sample 9	a	3.3	9	9	0	0	0	0.37	0.37	17.96	0.00
	b	2.9	9	9	0	0	0	0.32	0.32	15.64	0.00
	c	2.8	9	9	0	0	0	0.31	0.31	17.35	0.00
	d	3.3	9	9	0	0	0	0.37	0.37	17.50	0.00
	e	3.3	9	9	0	0	0	0.37	0.37	15.94	0.00
	f	3.2	9	9	0	0	0	0.36	0.36	18.03	0.00
	g	3.4	9	9	0	0	0	0.38	0.38	16.36	0.00
	h	3.1	9	9	0	0	0	0.34	0.34	16.46	0.00
	l	3	9	9	0	0	0	0.33	0.33	17.12	0.00
	j	3.2	9	9	0	0	0	0.36	0.36	16.62	0.00
	Average	**3.15**	**9**	**9**	**0**	**0**	**0**	**0.35**	**0.35**	**16.90**	**0.00**
	Max	**3.4**	**9**	**9**	**0**	**0**	**0**	**0.38**	**0.38**	**18.03**	**0.00**
	Min	**2.8**	**9**	**9**	**0**	**0**	**0**	**0.31**	**0.31**	**15.64**	**0.00**

	Trial	Weld Depth from parent material (mm)	Weld Width at Half Max (mm)	Weld Top Width (mm)	Crack Length in HAZ (mm)	Crack Length in Weld (mm)	Total Crack Length (mm)	Depth/ Top Width	Depth/ Mid Width	Weld Area (mm^2)	CI Weld (/mm)
Sample 10	a	2.5	3.8	6.1	0	0	0	0.41	0.66	8.91	0.00
	b	2.3	4.3	6.5	0	0	0	0.35	0.53	9.04	0.00
	c	2.4	4.2	6.4	0	0	0	0.38	0.57	9.21	0.00
	d	2.5	4.3	6.4	0	0	0	0.39	0.58	9.18	0.00
	e	2	4	7	0	0	0	0.29	0.50	9.53	0.00
	f	2.5	4.1	6.3	0	0	0	0.40	0.61	9.07	0.00
	g	2.2	4.2	6.7	0	0	0	0.33	0.52	9.25	0.00
	h	2.5	4.2	6.2	0	0	0	0.40	0.60	9.06	0.00
	I	2.4	4.3	6.5	0	0	0	0.37	0.56	9.12	0.00
	j	2.5	4	6.2	0	0	0	0.40	0.63	8.99	0.00
	Average	**2.38**	**4.14**	**6.43**	**0**	**0**	**0**	**0.37**	**0.57**	**9.14**	**0.00**
	Max	**2.5**	**4.3**	**7**	**0**	**0**	**0**	**0.41**	**0.66**	**9.53**	**0.00**
	Min	**2**	**3.8**	**6.1**	**0**	**0**	**0**	**0.29**	**0.50**	**8.91**	**0.00**
Sample 11	a	10	1.8	6.5	0	11.1	11.1	1.54	5.56	20.05	0.55
	b	10	1.8	6	0	12.6	12.6	1.67	5.56	19.99	0.63
	c	10	1.8	6.7	0	11.5	11.5	1.49	5.56	20.44	0.56
	d	10	1.8	6.4	0	12.2	12.2	1.56	5.56	19.99	0.61
	e	9.9	1.7	7.2	0	14	14	1.38	5.82	19.88	0.70
	f	10	1.8	6.1	0	13.7	13.7	1.64	5.56	19.94	0.69
	g	8.2	1.9	7.7	0	9.3	9.3	1.06	4.32	20.21	0.46
	h	10	1.7	6.9	0	15.3	15.3	1.45	5.88	19.82	0.77
	I	10	1.9	6.7	0	11.2	11.2	1.49	5.26	20.72	0.54
	j	8.5	1.8	7.6	0	9.6	9.6	1.12	4.72	20.20	0.48
	Average	**9.66**	**1.8**	**6.78**	**0**	**12.05**	**12.05**	**1.42**	**5.37**	**20.13**	**0.60**
	Max	**10**	**1.9**	**7.7**	**0**	**15.3**	**15.3**	**1.67**	**5.88**	**20.72**	**0.77**
	Min	**8.2**	**1.7**	**6**	**0**	**9.3**	**9.3**	**1.06**	**4.32**	**19.82**	**0.46**

	Trial	Weld Depth from parent material (mm)	Weld Width at Half Max (mm)	Weld Top Width (mm)	Crack Length in HAZ (mm)	Crack Length in Weld (mm)	Total Crack Length (mm)	Depth/ Top Width	Depth/ Mid Width	Weld Area (mm^2)	CI Weld (/mm)
Sample 12	a	8.6	1.2	4.3	0	6.1	6.1	2.00	7.17	11.96	0.51
	b	8.3	1.3	4.2	0	9.9	9.9	1.98	6.38	11.78	0.84
	c	7.4	1.3	5.1	0	12	12	1.45	5.69	11.48	1.05
	d	7.6	1.3	5	0	7.7	7.7	1.52	5.85	11.29	0.68
	e	7.6	1.3	4.3	0	9.4	9.4	1.77	5.85	11.36	0.83
	f	8.2	1.3	4.5	0	8.2	8.2	1.82	6.31	12.04	0.68
	g	8.8	1.3	4.3	0	9.2	9.2	2.05	6.77	11.89	0.77
	h	7.9	1.4	4.6	0	11.3	11.3	1.72	5.64	11.86	0.95
	l	8.3	1.4	4.2	0	7	7	1.98	5.93	12.02	0.58
	j	8.7	1.2	4.3	0	5.6	5.6	2.02	7.25	11.74	0.48
	Average	**8.14**	**1.3**	**4.48**	**0**	**8.64**	**8.64**	**1.83**	**6.28**	**11.74**	**0.74**
	Max	**8.8**	**1.4**	**5.1**	**0**	**12**	**12**	**2.05**	**7.25**	**12.04**	**1.05**
	Min	**7.4**	**1.2**	**4.2**	**0**	**5.6**	**5.6**	**1.45**	**5.64**	**11.29**	**0.48**
Sample 13	a	6.6	0.8	2.8	0	3.1	3.1	2.36	8.25	6.35	0.49
	b	6.1	0.9	2.8	0	4	4	2.18	6.78	6.23	0.64
	c	6.6	0.9	3	0	4.1	4.1	2.20	7.33	6.71	0.61
	d	5.9	0.9	3	0	3.6	3.6	1.97	6.56	6.22	0.58
	e	6	0.9	3.3	0	4.5	4.5	1.82	6.67	6.73	0.67
	f	6.3	0.9	3	0	3.1	3.1	2.10	7.00	6.40	0.48
	g	6.3	0.9	3	0	4.9	4.9	2.10	7.00	6.68	0.73
	h	6.1	0.8	3.2	0	3.5	3.5	1.91	7.63	6.49	0.54
	l	6	0.8	2.8	0	4.1	4.1	2.14	7.50	5.83	0.70
	j	6.1	0.8	3	0	3	3	2.03	7.63	6.19	0.48
	Average	**6.2**	**0.86**	**2.99**	**0**	**3.79**	**3.79**	**2.07**	**7.21**	**6.38**	**0.59**
	Max	**6.6**	**0.9**	**3.3**	**0**	**4.9**	**4.9**	**2.36**	**8.25**	**6.73**	**0.73**
	Min	**5.9**	**0.8**	**2.8**	**0**	**3**	**3**	**1.82**	**6.56**	**5.83**	**0.48**